

DIGITAL ACCESS TO SCHOLARSHIP AT HARVARD
DASH.HARVARD.EDU

HARVARD LIBRARY


Nanocalorimetry Experiments and First-Principles Theoretical Studies of Solid-State Reactions in Nanolaminates

Citation

Lee, Dongwoo. 2016. Nanocalorimetry Experiments and First-Principles Theoretical Studies of Solid-State Reactions in Nanolaminates. Doctoral dissertation, Harvard University, Graduate School of Arts & Sciences.

Link

http://nrs.harvard.edu/urn-3:HUL.InstRepos:33493483

Terms of use

This article was downloaded from Harvard University's DASH repository, and is made available under the terms and conditions applicable to Other Posted Material (LAA), as set forth at

https://harvardwiki.atlassian.net/wiki/external/NGY5NDE4ZjgzNTc5NDQzMGIzZWZhMGFlOWI2M2EwYTg

Accessibility

https://accessibility.huit.harvard.edu/digital-accessibility-policy

Share Your Story

The Harvard community has made this article openly available.
Please share how this access benefits you. Submit a story

Nanocalorimetry Experiments and First-Principles Theoretical Studies of Solid-State Reactions in Nanolaminates

A dissertation presented

by

Dongwoo Lee

to

The School of Engineering and Applied Sciences

in partial fulfillment of the requirements

for the degree of

Doctor of Philosophy

in the subject of

Applied Physics

Harvard University

Cambridge, Massachusetts

February 2016

© 2016 – Dongwoo Lee

All rights reserved

Thesis advisor
Joost J. Vlassak

Author
Dongwoo Lee

Nanocalorimetry Experiments and First-Principles Theoretical Studies of Solid-State Reactions in Nanolaminates

Abstract

The extraordinary sensitivity and extremely small thermal mass of chip-based nanocalorimetry sensors allow the study of reactions in thin films over a broad range of heating rates, from isothermal to 10^5 K/s. First-principles calculations provide insight in the phase transformation and diffusion behavior of a material at the atomistic scale. Combination of nanocalorimetry and first-principles, therefore, is highly efficient and reliable to determine the atomistic-to-macroscopic response of materials. This thesis explores, through use of this combined approach, reactions in reactive multilayers to synthesize ultra-high temperature ceramic coatings.

We employ scanning AC and DC calorimetry techniques to investigate the synthesis of ZrB_2 and carbon-doped ZrB_2 using Zr/B and Zr/B_4C multilayered reactive nanolaminates (MRNL). The solid-state reactions in these multilayers are shown to proceed in two distinct steps: an interdiffusion/amorphization step followed by a crystallization step. Measurements performed at heating rates ranging from 1,000 to 55,000 K/s allows determination of the kinetic parameters of the multilayer reactions,

such as the activation energies of interdiffusion and crystallization. Low activation energies in the interdiffusion processes in the Zr/B MRNLs are found and amorphization is shown to facilitate fast transport of B atoms into Zr lattice. It has also been shown that C impurity atoms in the Zr/B_4C MRNLs further reduce activation energies of interdiffusion and crystallization.

First-principles theoretical modeling provides insight in the amorphization processes in the Zr/B MRNLs and confirms the relatively low activation energies associated with the processes. The simulations further elucidate the effects of concentration (ZrB_x, $0<x\leq2$) and temperature on the diffusion kinetics and phase evolution of the Zr-B alloys. The effect of additives such as C and N on the synthesis of ZrB_2 using MRNLs has also been investigated using the first-principles theoretical approach. It has been revealed that both impurities facilitate amorphization, enhancing intermixing of the constituent layers of the MRNLs.

-

Table of Contents

Title Page ..... **i**

Copyright page ..... **ii**

Abstract ..... **iii**

Table of Contents ..... **v**

Acknowledgements ..... **vii**

Chapter 1. Introduction and background **1**
1.1 Nanocalorimetry **1**
1.1.1 Working principles 1
1.1.2 Design and fabrication of sensors 5
1.2 Combination of nanocalorimetry and first-principles calculations to investigate phase transformations of thin films **7**
1.3. Multilayered reactive nanolaminates (MRNLs) to synthesize ZrB_2 based alloys **8**
1.3.1 Properties and processing of ZrB_2 8
1.3.2 Phase transformations of MRNLs studied by nanocalorimetry 9
1.4 Outline of the thesis **14**

Chapter 2. AC nanocalorimetry to study solid-state reactions in thin films **16**
2.1 Introduction **16**
2.2 The nanocalorimetry sensor **18**
2.3 Scanning AC nanocalorimetry **21**
2.4 Analysis of solid-state reactions using scanning AC nanocalorimetry **23**
2.5 Experimental details **31**
2.6 Results **35**
2.7 Discussion **41**
2.8 Summary **44**

Chapter 3. Low temperature synthesis of ZrB_2 via MRNLs **46**
3.1 Introduction **46**
3.2 Experimental **49**
3.3 Results and discussion **52**
3.3.1 Nanocalorimetry and TEM studies on Zr/B MRNLs 52
3.3.2 Thermodynamics and kinetics of the reactions in Zr/B MRNLs 59
3.4 Summary **64**

Chapter 4. Thermodynamics and kinetics solid-state alloying of Zr-B with different concentrations **66**
4.1 Introduction **66**
4.2 Results and discussion **68**
4.2.1 Energetics of B insertion into the crystalline Zr host 68
4.2.2 Interstitial diffusion of B in Zr 71
4.2.3 Energetics, structural features, and diffusion kinetics in the intermediate compounds ZrB_x, $0.25 \leq x \leq 2$. 74
4.2.4 Diffusivity of B in various Zr-B compounds 78
4.2.5 Comparison between first-principles and nanocalorimetry results 81
4.3 Methods **82**

4.4 Summary **83**

Chapter 5. Kinetic role of carbon in solid-state synthesis of ZrB_2 using MRNLs ... **84**
5.1 Introduction **84**
5.2 Results and discussion **86**
5.2.1 Nanocalorimetry and structural characterizations of Zr/B_4C MRNLs 86
5.2.2 Kinetics of reactions in Zr/B_4C MRNLs 90
5.2.2 First-principles calculations of Zr-C 93
5.4 Methods **97**
5.4 Summary **98**

Chapter 6. Enhanced transport of B into Zr via local instability at the interface of MRNLs with impurities **100**
6.1 Introduction **100**
6.2 Results and discussion **103**
6.2.1 Nature of the bond between Zr and B or C 103
6.2.2 Effect of C impurities on amorphization and diffusion in Zr/B alloys 106
6.2.3 AIMD on Zr/B and Zr/B_4C MRNLs 108
6.2.4 Processing strategy of transition metal borides from MRNLs using impurity atoms 113
6.3 Methods **116**
6.4 Summary **116**

Chapter 7. Conclusion and outlook **118**

Appendix **121**
Appendix A **121**
Appendix B **125**
Appendix C **129**

Bibliography **131**

Acknowledgements

First and foremost, I would like to thank Prof. Joost Vlassak for his mentorship and guidance throughout the years at Harvard. It was only with his help that I am able to develop the scientific mindset that I have today. I will always be indebted to him.

I also want to thank my thesis committee members Prof. Frans Spaepen, Prof. David Clarke, and Prof. Joanna Aizenberg. Special thanks to Prof. Spaepen for his exciting and extremely helpful classes (AP 282 and AP 292) as well as discussions relating to my research.

I want to give thanks to Prof. Kejie Zhao (Purdue), Prof. Jan Schroers (Yale), and Prof. Stefano Curtarolo (Duke) for their helpful suggestions and support. They have broadened my perspectives and taken my research to another level.

Special thanks to all past and current members in the Vlassak group: Dr. Gi-dong Sim, Dr. Jeong-Yun Sun, Dr. Jianyu Li, Dr. Kechao Xiao, Dr. Gayatri Cuddalorepatta, Dr. Patrick Mccluskey, Dr. Matt Pharr, Dr. Widusha Illeperuma, Dr. John Gregoire, Dr. Kamyar Davoudi, Dr. Han Li, Prof. Jun-hyub Park, Prof. Insu Jeon, Dr. Jinhye Bae, Kevin Tian, Haitao Zhang, and Bingge Zhao. I would like to extend thanks to everyone I have met at Harvard including ELP friends.

Finally, I want to dedicate this dissertation to my wife Jiwon, our son Jaewon, my parents, and parents in law. This thesis would never have been accomplished without their love, encouragement, and support.

Chapter 1. Introduction and background

1.1 NANOCALORIMETRY

1.1.1 Working principles

A nanocalorimetry sensor in this work consists of a thin-film thermistor sandwiched between two electrically insulating silicon nitride layers that form a membrane supported by the substrate (Figure 1.1). The thermistor serves both as a heating element and a thermometer. It is made of tungsten because of its large temperature coefficient of resistance and its small resistivity, both of which are beneficial to measurement sensitivity. The high melting temperature of tungsten also results in excellent thermal stability of the thermistor. The electrical leads and contact pads on the substrate are made of copper to reduce the resistance of the signal lines on the substrate and to facilitate contact to the PnSC device [1, 2].

Samples to be measured are limited to the thermistor area of each sensor through use of a Si-based shadow mask (Figure 1.2 ab). The membrane design of the sensor thermally insulates the sample from its surroundings and ensures that the thermal mass of the sensor, i.e., the addendum, is very small. As shown in Figure 1.1.b, the straight lines down the center of the membrane is the heating element; the metal lines connected to the heater are the voltage probes, and the portion of the heating element between the voltage probes is the thermistor. A current passing through the thermistor heats the sample and the calorimetric cell. The power dissipated in the thermistor is determined experimentally from the current supplied to the thermistor and the potential drop between the voltage

probes. The local temperature change is determined from a four-point thermistor resistance measurement that has been calibrated to temperature. The calorimetric signal is then calculated from the power dissipated in the thermistor and the heating rate of the sample.

Not all power dissipated in the thermistor is used to heat the sample and addendum; some of it is lost to the environment. At moderate temperatures, heat transfer from the thermistor to the membrane dominates this heat loss. As the temperature increases, radiation from the thermistor and the membrane becomes important and eventually dominates the heat loss. Measurements are generally performed in vacuum to eliminate convection losses and to provide a chemically inert testing environment. Conduction and radiation heat losses can be accounted for by modeling as will be discussed in detail in Chapter 2 and Appendix A. Alternatively, measurements can be performed using scanning AC calorimetry method, where measurement results are insensitive to heat loss [3].

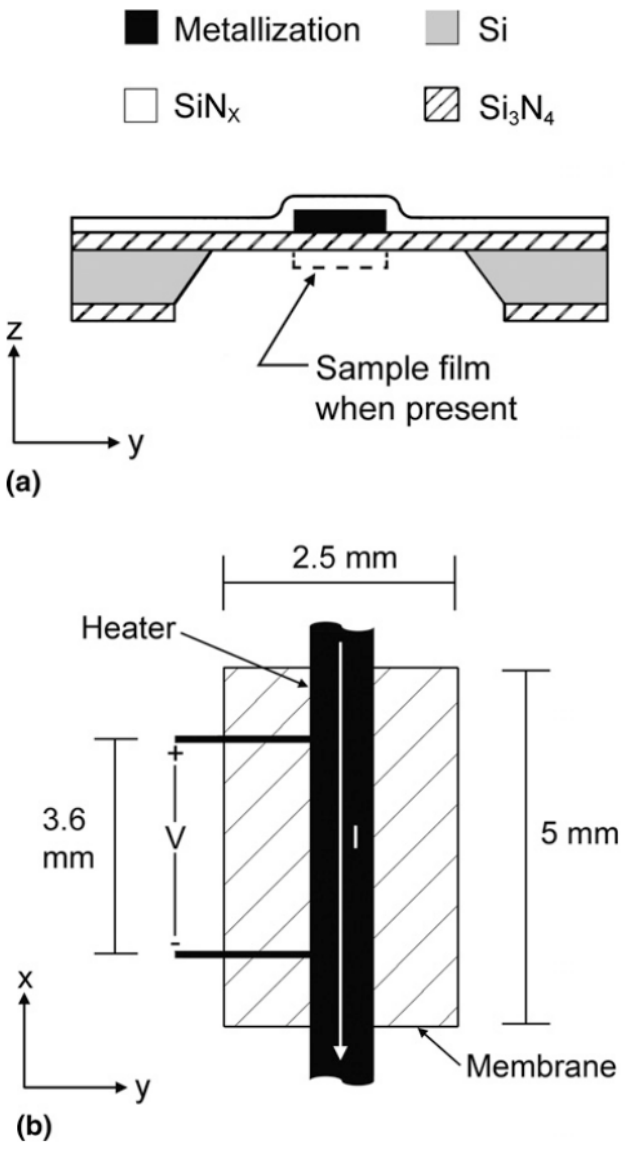


Figure 1.1. Layout of the nanocalorimeter cell [2]: (a) cross-section schematic, and (b) plan-view schematic. Heater line width is 0.8 mm and voltage probe line width is 0.1 mm. "P. J. McCluskey and J. J. Vlassak, Combinatorial nanocalorimetry, Journal of Materials Research, Vol. 25, issue 11, pp. 2086-2100, reproduced with permission."

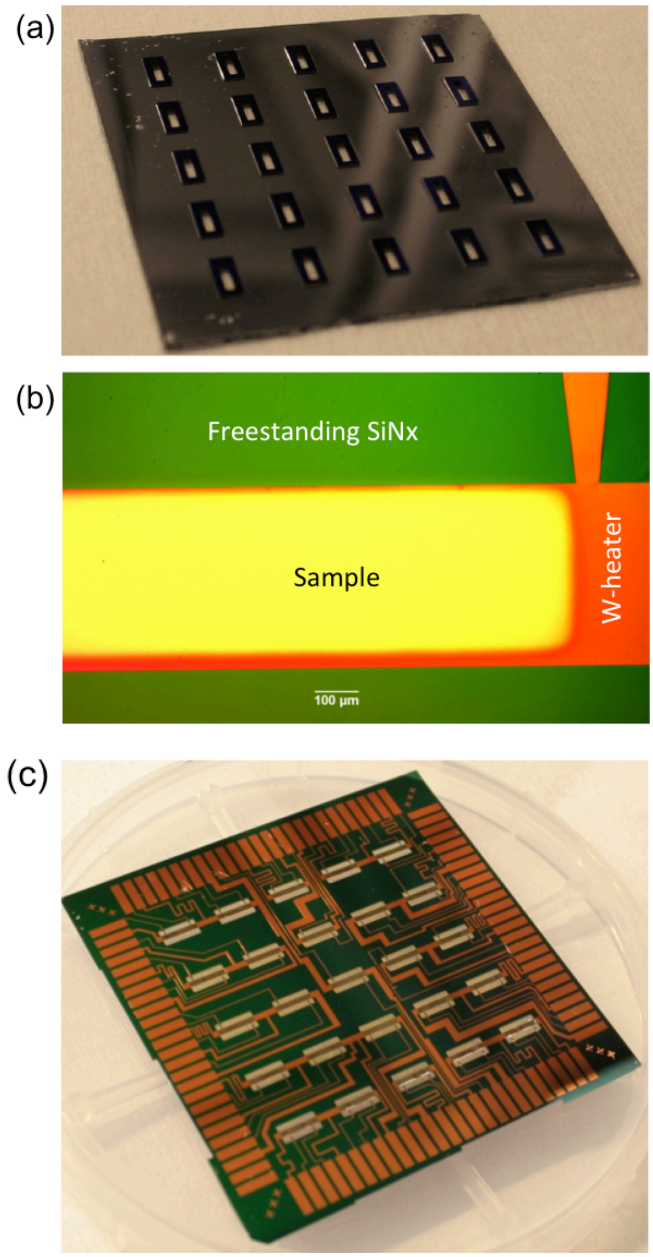


Figure 1.2. (a) A Si-shadow mask used to deposit samples in nanocalorimeters. (b) Sensor with a sample deposited by using the shadow mask. (c) Photograph of the 25-cell PnSC device.

1.1.2 Design and fabrication of sensors

The nanocalorimeter device in this work consists of a silicon substrate with an array of micromachined thermal sensors. The sensors are arranged in a 5 x 5 array as illustrated in Figure 1.2c. The device is fabricated using conventional Si-based microfabrication steps as depicted in Figure 1.3. Because the substrates used in combinatorial nanocalorimetry contain arrays of sensors, it is possible to perform combinatorial experiments both in terms of sample composition and thermal treatments: samples with different compositions can be deposited across an array and all samples can be subjected to the same thermal treatment. Conversely, identical sample can be subjected to a range of experiments where the heating rate is varied over orders of magnitude to measure the activation energies of the various reaction processes that take place.

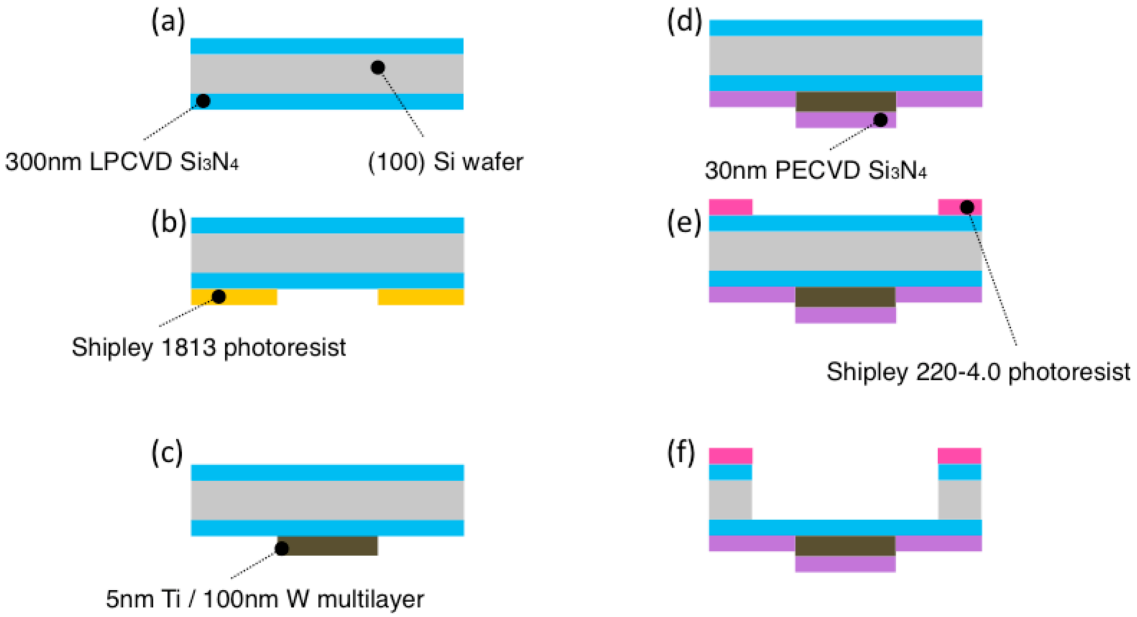


Figure 1.3. (a) The fabrication process starts with a (100) Si wafer passivated with 300 nm low-stress LPCVD nitiride. (b) Photoresist is spin-coated and patterend on the front side of the wafer. (c) Layers of 5 nm titanium and 100 nm tungsten are sputter deposited and patterned using a lift-off procedure. Copper is then deposited and patterned using the same procedure (not shown in the figure) to connect the heater to the contact pads. (d) After metal patterning, 30 nm Si_3N_4 is coated on the front side to protect the metal layers from oxidation. (e) To make freestanding membranes, photoresist is patterned on the backside and (f) Si is removed using a SPTS Rapier DRIE system [4]. Reprinted with permission from Lee, D.; Sim, G. D.; Xiao, K. C.; Vlassak, J. J., J Phys Chem C, 2014, 118, 21192-21198. Copyright (2014) American Chemical Society.

1.2 COMBINATION OF NANOCALORIMETRY AND FIRST-PRINCIPLES CALCULATIONS TO INVESTIGATE PHASE TRANSFORMATIONS OF THIN FILMS

First-principles theoretical studies can determine the energetics, structural evolution, and phase transitions in the material systems, as well as the electronic, ionic, and mechanical properties of a material. The modeling draws the energy landscapes of diffusion and various reaction pathways, and identifies the stable and/or metastable phases [5]. The results from the theoretical studies can be verified using nanocalorimetry and structural characterization tools such as X-ray diffraction (XRD) and transmission electron microscopy (TEM) [5, 6]. Nanocalorimetry measurements enable the investigation of formation mechanisms and characterize formation kinetics of various material systems. The nanocalorimetry experiments and first-principles theoretical modeling inform and guide each other, offering a comprehensive understanding of the fundamental mechanisms that underlie reactions in the materials of interest. In this thesis, reactions in multilayered reactive nanolaminates (MRNLs) to synthesize ZrB_2–based alloys are investigated by using the combined approach.

1.3. MULTILAYERED REACTIVE NANOLAMINATES (MRNLS) TO SYNTHESIZE ZrB_2 BASED ALLOYS

1.3.1 Properties and processing of ZrB_2

Transition metal diborides (TMB_2) of the main group and rare earth metals exhibit layered honeycomb structures. The partial ionic character of M−B bonds in TMB_2 leads to a $(B^-)_n$ lattice that is isoelectronic to graphite, explaining the sheet-like structure of TMB_2 [7]. Among the metal diborides, ZrB_2 is of special interest, as its unique set of properties allows a variety of potential applications [7, 8]. Excellent electrical and thermal conductivities, metal-like optical properties of ZrB_2, and the similarity of in-plane lattice constants and the thermal expansion coefficients between ZrB_2 and GaN suggest the promising prospect of ZrB_2 as a substrate or a buffer layer for group III nitride semiconductors for optoelectronic and microelectronic applications [7, 9-12]. Furthermore, its combination of properties such as extremely high melting point, chemical inertness, good oxidation resistance, and very high hardness makes ZrB_2 a great candidate for structural applications in extreme environments [8, 13, 14]. The highly stable structure of ZrB_2, however, is challenging for large scale processing, preventing the versatile material from being used in many practical applications. ZrB_2 can be synthesized via reduction processes [8], chemical routes [11, 15, 16], or reactive processes [4, 17]. Little is known, however, about the details of the diffusion kinetics between Zr and B, although this knowledge is critical for the synthesis processes and for enhancing the processibility of ZrB_2. Experimental values of the activation energy of Zr-B diffusion are available but with a large variation of 0.47 ~ 1.99 eV [4, 18]. Calorimetric

studies on multilayered reactive nanolaminates (MRNLs) to synthesize ZrB_2 offer an opportunity to thoroughly understand thermodynamics and kinetics of its formation reaction of the material.

1.3.2 Phase transformations of MRNLs studied by nanocalorimetry

A multilayered reactive nanolaminate (MRNL) is an energetic material that consists of alternating thin layers of two or more reactants [19, 20]. Examples of MRNLs are shown in Figure 1.4. The heterogeneous structure stores energy due to the metastable structure. Due to the negative heat of mixing in the constituent layers of the MRNLs, the stored energy in the metastable structure is released upon interdiffusion of the layers and crystallization of intermetallic compounds. The thermodynamics, diffusion kinetics, and structural evolution during the formation of a compound can be investigated using a calorimeter: an ideal tool to determine reaction enthalpies, temperatures of transformation, and specific heats in these systems [21].

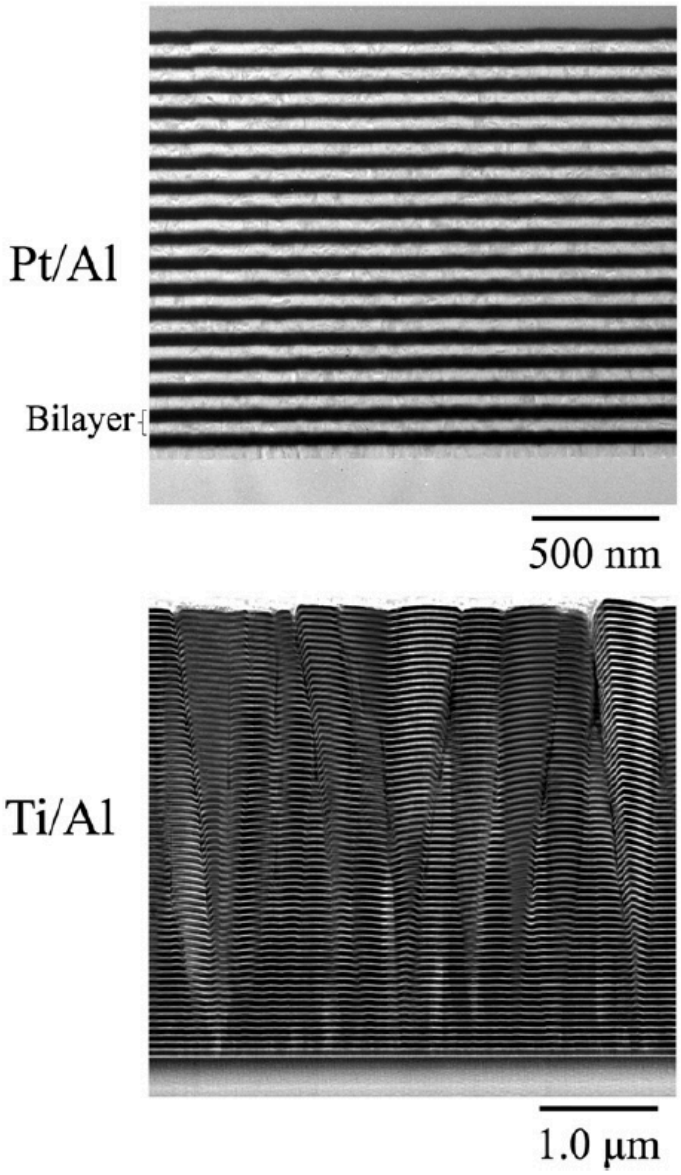


Figure 1.4. Cross sectional transmission electron micrographs of reactive multilayers fabricated by magnetron sputter deposition: ~1.6 μm Pt/Al (bright field) and ~3.8 μm Ti/Al (high-angle annular darkfield) on silicon dioxide substrates. Each multilayer has a fixed bilayer thickness (94 nmfor Pt/Al and 57.5 nm for Ti/Al) [20]. Reprinted from Thin Solid Films, Vol. 576, D.P. Adams, Reactive multilayers fabricated by vapor deposition: A critical review, pp. 98-128, Copyright (2015), with permission from Elsevier.

One notable example of an application of calorimetry is the study of the formation of amorphous compounds by solid-state reactions in metallic MRNLs. Amorphization reactions in nanolaminates are critical to the study of ZrB_2 formation in MRNLs, since the presence of an amorphous phase is known to enhance the transport of B atoms and thus improve the processibility of ZrB_2 [4, 5, 22]. Schwarz and Johnson [23] reported the first example of the formation of an amorphous phase in a metallic MRNL of Au-La. The phenomenon has since been observed in a number of diffusion couples and characterized by using calorimetry [24]. Figure 1.5 shows an example of calorimetric results on Ni/Zr MRNLs, which shows two exothermic peaks corresponding to solid-state amorphization and subsequent crystallization. The diffusion couples that form amorphous compounds usually have the following characteristics in common: (i) a large negative heat of mixing of the components and (ii) a significant difference between the diffusivities of the two elements in the amorphous phase. The formation of equilibrium intermetallic phases, which are often found in these alloys, must of course be suppressed [21].

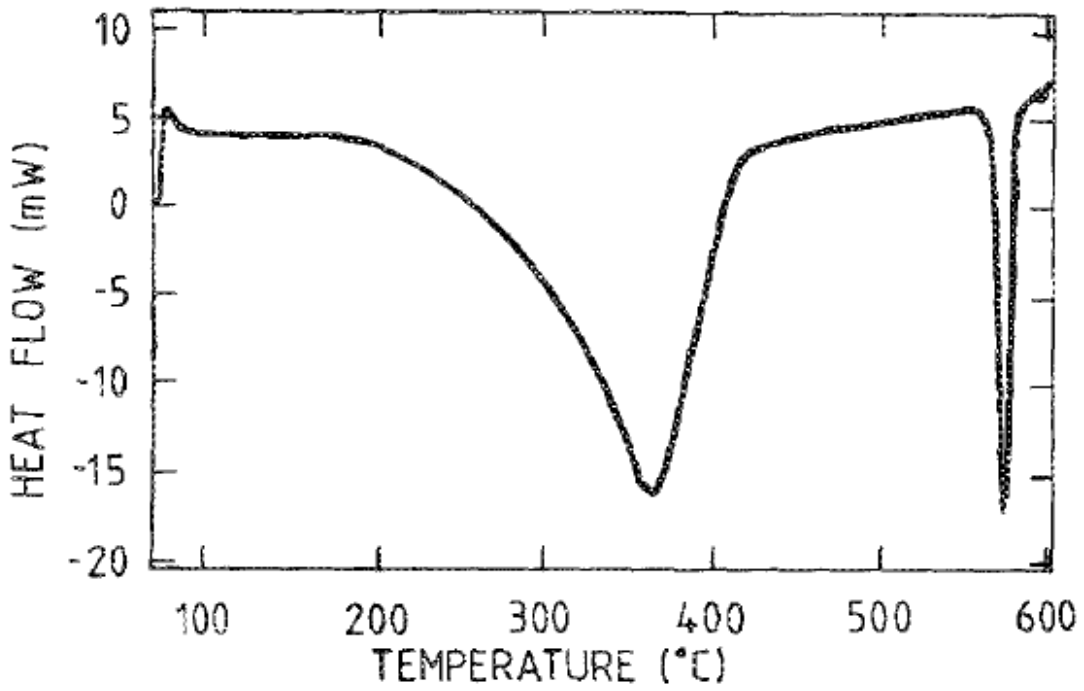


Figure 1.5. Differential scanning calorimetry (DSC) trace due to heating a $Ni_{67}Zr_{33}$ multilayer with a bilayer period of 63nm. Heating rate was 40K/min. Reprinted from Applied physic Letters, Vol. 50, R. J. Highmore, J. E. Evetts, A. L. Greer, and R. E. Somekh, Differential Scanning calorimetry study of solid-state amorphization in multilayer thin-film Ni/Zr. pp. 98-128, Copyright (1987), with permission from AIP publishing LLC.

Suppression of these phases is possible through the greater ease of formation of the isotropic amorphous phase at the interfaces in a nanolaminate, since the formation of an intermetallic crystalline nucleus requires the creation of at least one high-energy incoherent interface [21]. The steep concentration gradients at the interfaces of the MRNLs also suppress the thermodynamic driving force for crystallization [25-27]. Atom transport may be sufficient to accomplish the relatively short-range rearrangements necessary for amorphization, but not the longer-range ones required to form the larger unit cells of intermetallic compounds. Since thickening of the amorphous layer is governed by diffusion through the layer, the amorphization rate continuously slows down and eventually nucleation of intermetallics at the interface becomes competitive [21]. Individual amorphous layers can therefore not grow beyond a critical thickness. Thick fully amorphous coatings must be made using nanolaminates that consist of bilayers thinner than this critical thickness.

In this thesis, we study formation of ZrB_2 in MRNLs, using nanocalorimetry instead of conventional calorimetry. Nanocalorimetry has several important advantages over conventional calorimetry: the technique is much more sensitive than conventional calorimetry and can be applied to thin-film samples just a few nanometers thick rather than microns. As a result, samples are readily synthesized using thin-film deposition techniques. Thus, a large number of materials systems and sample parameters (e.g. MRNL bilayer thickness) can be explored. More importantly, nanocalorimetry has a huge dynamic range that makes it ideally suited for kinetics studies: through a combination of DC and AC techniques, measurements can be performed at rates from isothermal to 50,000 K/s, which is simply not possible with conventional calorimetry.

1.4 OUTLINE OF THE THESIS

The goal of this thesis is to investigate phase transformations in MRNLs to synthesize ZrB_2 based alloys by using the combined approach of nanocalorimetry and first-principles calculations. The thesis is organized as follows. Chapter 2 introduces the scanning AC nanocalorimetry technique to study phase transformations in MRNLs. A data reduction algorithm is discussed to determine heat flow of a reaction. The technique has been utilized to investigate the ZrB_2 formation reaction from Zr/B MRNLs with a bilayer period of 50 nm. We find that the two-step process of amorphization followed by crystallization occurs during the scanning measurements. The conversion to ZrB_2 is not complete, however, and significant amount of Zr and B remain. In Chapter 3, we achieve full conversion from Zr/B MRNLs with bilayer periods of 4 ~ 8 nm to ZrB_2 at relatively low temperature by preparing high-purity MRNLs. Nanocalorimetry and transmission electron microscope are used to study the kinetics of amorphization and crystallization in Zr/B MRNLs. We determine activation energies of reaction processes in the MRNLs. In Chapter 4, we investigate thermodynamics and kinetics of the solid-state alloying of Zr-B by using first-principles theoretical studies in order to understand the underlying process in the synthesis of ZrB_2. The simulation result is compared with nanocalorimetry results and shows good agreement. Kinetic parameters of diffusion as a function of concentration in ZrB_x are also studied. Next, in Chapter 5, we perform nanocalorimetry studies on the effect of C additives in the synthesis of ZrB_2 based alloys from MRNLs. We reveal that addition of C lowers activation energies of the processes responsible to synthesize ZrB_2. First-principles modeling shows that Zr has stronger bonding with C than B, which may reduce the diffusion activation energy. More detailed theoretical

modeling on the role of impurities in the synthesis of ZrB_2 is explored in Chapter 6, where we perform ab initio molecular dynamics (AIMD). Based on the results, we propose that the addition of elements with strong binding energies to transition metals may be an effective method to facilitate the low-temperature synthesis of diboride-based ceramics using MRNLs. We compile a map of the heat of mixing of various transition metals with B, C, and N to guide the synthesis of diboride-based ceramics using MRNLs.

Chapter 2. AC nanocalorimetry to study solid-state reactions in thin films*

*Reprinted with permission from D. Lee, G.D. Sim, K. Xiao, and J. J. Vlassak, Journal of Applied Physics 114 (21), 214902(2013). Copyright 2013 AIP Publishing LLC

2.1 INTRODUCTION

ZrB_2, classified as an ultra high-temperature ceramic (UHTC), possesses superb thermal, mechanical, and electrical properties, including an extremely high melting point (>3,200° C), high thermal/electric conductivity, chemical inertness, excellent thermal shock resistance, and good oxidation resistance. Due to these benefits, the utilization of this transition metal boride has been proposed for advanced structural applications in extreme environments, such as wing leading edges, nose tips, and propulsion system components of hypersonic vehicles [8, 13].

The unique set of properties of ZrB_2 stem mainly from the highly covalent nature of the Zr-B and B-B bonding, and the ionic nature of Zr-Zr bonding in the hexagonal closed packed structure (P6/mmm) [8, 28]. ZrB_2 can be prepared using reactive processes, including self-propagating high-temperature synthesis (SHS), spark plasma synthesis (SPS), and reactive hot pressing (RHP). Chemical routes and reduction processes are also available for the preparation of ZrB_2 [8]. Regardless of the type of processing methods, fabrication of dense structure of ZrB_2 requires very high temperature

and pressure, which makes processing difficult [8, 29]. To overcome challenges such as poor sinterability and difficult densification, and to investigate the thermo-physical characteristics of the material, a great deal of research has been devoted to phase/structure evolution and chemical composition change during ZrB_2 formation [30-34]. In this study we employ scanning AC nanocalorimetry to investigate the synthesis of ZrB_2 from reactive multilayers of Zr and B.

Calorimetry of multilayered thin-film materials systems can be used to conduct fundamental studies of the thermodynamics and kinetics of reactions that are not readily accessible in bulk materials systems [19, 21, 35-37]. Nanocalorimetry makes it possible to conduct such studies on extremely small samples over a very wide range of heating rates [1-3, 35, 38, 39]. DC nanocalorimetry, in particular, can be used to make accurate calorimetry measurements at heating and cooling rates in the 4,000-40,000 K/s range, whereas AC nanocalorimeters were developed [3, 40-42] to enable measurements for scan rates below 4,000K/s, bridging the gap between traditional calorimetry and DC nanocalorimetry.

When multilayers with large negative reaction enthalpies react, they release a large amount of thermal energy that can be used for joining two dissimilar materials. For example, nano-structured Ni/Al multilayers have been studied to braze various materials including alloys, bulk metallic glass, and silicon [43-47]. In this process, the Ni/Al multilayer acts as a local heat source that melts the brazing layers. A small thermal pulse is sufficient to activate the brazing process because the large enthalpy of reaction of Ni and Al, and the short diffusion distances in the multilayer lead to a self-propagating reaction. As the reaction to form ZrB_2 from Zr and B is highly exothermic [28], it may be

possible to use nano-structured multilayers of Zr and B for joining materials, especially in ultra high-temperature applications. This potential application motivated us to investigate the solid-state reaction in Zr/B multilayers.

The aim of this chapter is two-fold: 1) the first application of scanning AC nanocalorimetry to a reactive multilayer sample at a heating rate that is not accessible with traditional calorimetry, and 2) investigation of the solid-state reaction in Zr/B multilayers upon heating. We discuss the experimental details of scanning AC nanocalorimetry in Chapter 2.2 – 2.3 and 2.5. In Chapter 2.4, we propose a data reduction method to extract the rate of heat release from the multilayer sample and we verify its validity using finite element simulations. In Chapter 2.6, we present the results of the scanning AC nanocalorimetry study of a Zr/B multilayer and show that the formation of ZrB_2 proceeds in a two-step process.

2.2 THE NANOCALORIMETRY SENSOR

Scanning nanocalorimetry measurements were performed on a thin Zr/B multilayer using the parallel nano-scanning calorimeter device (PnSC) [1, 2]. This device consists of an array of nanocalorimeter sensors capable of thermo-physical characterization of samples with very small thermal mass. As schematically drawn in Figure 2.1, each sensor in a PnSC device consists of a metal line encapsulated in a thin non-conducting membrane. The metal line serves both as a heater and as a resistive thermometer in a four-point measurement scheme. During a calorimetry measurement, a current is applied to the metal line and the line heats the sample of interest. Both the applied current and the voltage drop across the resistance thermometer are continuously

recorded, enabling precise measurement of the power supplied to the sensor and the temperature of the sample, which is related to the resistance of the heating element by

$$R(T_0) = R(T_A)(1 + \lambda(T_0 - T_A)) \tag{2.1}$$

where R is the resistance of the heating element, λ is the temperature coefficient of resistance of the line, T_0 is the average temperature of the heating element, and T_A denotes the ambient temperature. In a typical measurement, the thermal diffusion lengths of sample and membrane are much larger than their thicknesses, making any temperature gradients in the out-of-plane direction negligibly small [1, 2].

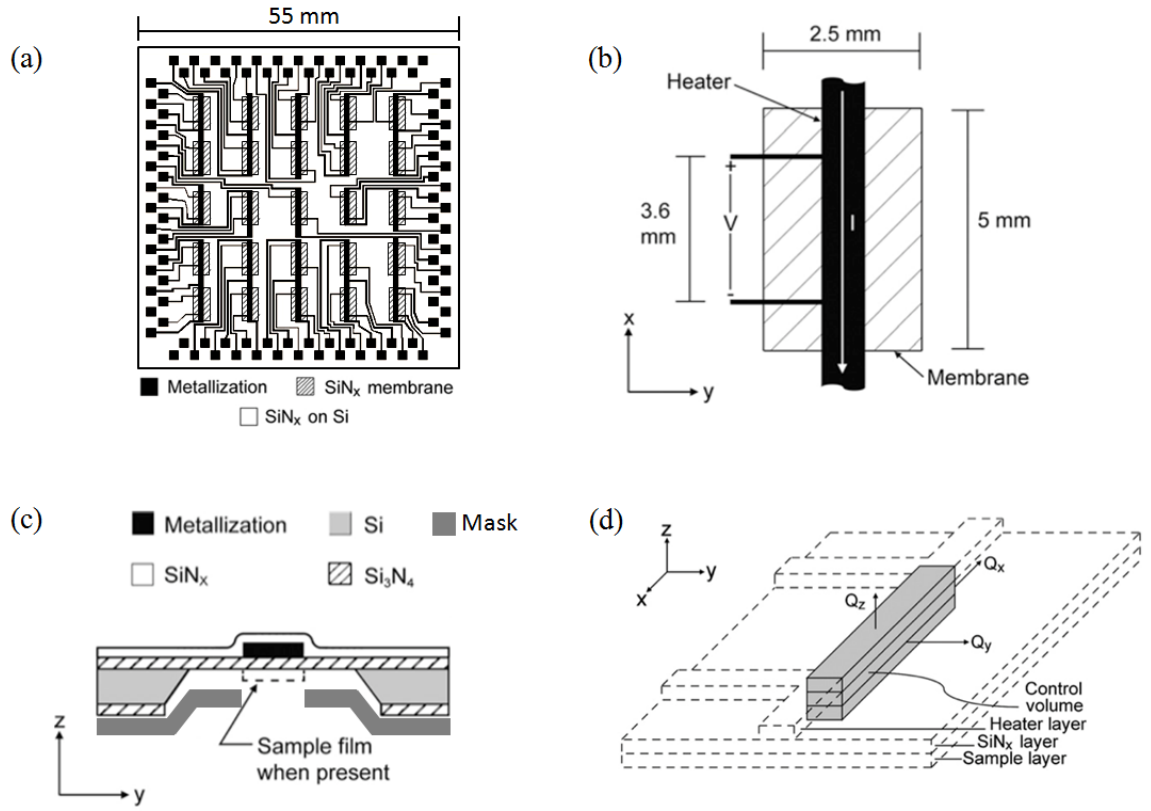


Figure 2.1. Schematic of the PnSC device. (a) Plan view of the PnSC device showing an array of nanocalorimetry sensors; (b) plan view of one sensor; (c) cross-sectional view of a sensor; (d) perspective view of the control volume containing sample and sensor addendum.

2.3 SCANNING AC NANOCALORIMETRY

The nanocalorimetric sensors on the PnSC device can be used to perform either DC or AC measurements depending on the heating rate. DC nanocalorimtery requires a high heating rate (1,000 - 40,000 K/s) to minimize any heat loss to the environment. AC nanocalorimetry, on the other hand, is insensitive to heat loss and can be used at heating rates ranging from isothermal to 4,000K/s [3, 40-42].

When a current I is supplied to the heating element of a PnSC sensor, the energy balance for the control volume (CV) that contains the sample and sensor addendum as marked in Figure 2.1d is

$$P = I^2 R$$

$$= C_p \frac{dT}{dt} + L + H \tag{2.2}$$

where P is the power supplied to the heater, R the resistance of the heating element within the CV, C_p the total heat capacity of the CV, and L the rate of heat loss to the environment. The enthalpy term H represents the rate at which the sample absorbs or releases heat as a result of solid-state reactions or phase transformations. In the context of this chapter, we refer to this term as the reaction enthalpy flow. In a DC nanocalorimetry measurement, the heating rate needs to be sufficiently large that the heat loss L is small compared with the other two terms in the right hand side of Equation (2.2). Knowledge of the power supplied to the sensor and the heating rate then provides the necessary data to determine the calorimetric signal of the sample. At slow scan rates or very high temperatures, the heat loss to the environment becomes so large that DC measurements fail to give meaningful results. In that case, measurements can be performed by means of

scanning AC nanocalorimetry. The scanning AC nanocalorimetry technique is discussed at length in references [3] and [40]; here we provide a brief summary. In scanning AC nanocalorimetry, the sensor is heated with a current that consists of a DC component and an oscillating component with angular frequency *w*,

$$I = I_0 + i\cos\omega t. \tag{2.3}$$

If the frequency is high enough, near-adiabatic operation of the sensor can be achieved enabling one to obtain precise values of the heat capacity. For AC nanocalorimetry, the energy balance equation can be written as

$$\begin{aligned} P &= \left[I_0 + i\cos\omega t\right]^2 R_0(1+\lambda\theta) \\ &= C_P\left(\frac{dT_0}{dt} + \frac{d\theta}{dt}\right) + L + H \end{aligned} \tag{2.4}$$

where T_0 is the temperature of the CV averaged over one oscillating period, θ is the oscillating part of the temperature, and R_0 is the resistance of the heating element at temperature T_0. The temperature oscillation of the heater produces harmonics in the potential drop across the resistor that can be used to determine the heat capacity of the sample and sensor [3]. With some mathematical manipulations, Equation (2.4) can be written as a set of two equivalent equations in T_0 and θ.

$$P_0 = \left({I_0}^2 + \frac{1}{2}i^2\right)R_0 = C_P\frac{dT_0}{dt} + L_0 + H_0, \tag{2.5}$$

$$2I_0 i R_0 \cos\omega t + \frac{1}{2}i^2 R_0 \cos 2\omega t = C\frac{d\theta}{dt} + \alpha\theta \tag{2.6}$$

where L_0 and H_0 represent the heat loss and reaction enthalpy flow averaged over one oscillation period, and *a* is the sum of their total time derivatives. Equation (2.5) describes the monotonic temperature response of the sensor, while Equation (2.6) describes its oscillatory response. Further analysis of Equation (2.6) eventually leads to

the following expression for the heat capacity of the CV [3, 40] in terms of the measured amplitude $V_{2\omega}$ and phase angle j of the 2ω - harmonic in the voltage across the resistor:

$$C_P = \frac{i^2 I_0 R_0 \lambda}{\omega |V_{2\omega}|} \sqrt{\frac{25\tan^2\varphi + 9}{16\tan^2\varphi + 4} \times \frac{\tan^2\varphi}{1+\tan^2\varphi}} \tag{2.7}$$

The phase angle φ and α are related by

$$\tan\varphi = \frac{C_P \omega}{\alpha} \tag{2.8}$$

These expressions are accurate provided that R_0 remain constant on the time scale of the temperature oscillations and q be sufficiently small [3],

$$\lambda \frac{dT_0}{dt} \frac{2\pi}{\omega} \ll 1,$$

$$\lambda\theta \ll 1, \tag{2.9}$$

respectively. These conditions are readily satisfied by designing the input current profile following the procedure detailed in reference [3].

2.4 ANALYSIS OF SOLID-STATE REACTIONS USING SCANNING AC NANOCALORIMETRY

While scanning AC nanocalorimetry allows direct determination of the heat capacity of a sample using Equation (2.7), it is also possible to extract information on the enthalpy flow H resulting from any solid-state reaction in the sample by considering the DC component of the calorimetry signal. In this section, we describe a simple but effective method to perform this analysis and use a finite element simulation to verify its accuracy.

Consider the following more explicit form of the energy balance in Equation (2.5)

$$P_0 = C_p \frac{dT_0}{dt} + L_C(T_0, \chi) + L_R(T_0) + H_0(T_0, \chi), \tag{2.10}$$

Here, L_C represents the power lost to the environment by conduction through the membrane and the heating element, while L_R represents the radiative heat loss, both quantities appropriately averaged over one oscillation period. Since measurements are typically performed in vacuum, there is no convective heat loss. The period-averaged past temperature history of the CV is represented by c. The analysis method is based on the observations that the radiative heat loss is a function of temperature only, while the conductive heat loss depends on both temperature and temperature history. Furthermore, for small temperature oscillations, the averaged heat loss terms do not depend on the amplitude of the temperature oscillations. The reaction enthalpy flow, H_0, generally depends on both temperature and past temperature history.

Consider a typical experiment that consists of two subsequent nanocalorimetry scans with similar but not identical heating rates. The sample undergoes an irreversible solid-state reaction during the first scan, but not during the second. The energy balance equations for both scans are then

$$P_0^{(1)}\left(T_0^{(1)}\right) = C_p^{(1)} \frac{dT_0^{(1)}}{dt} + L_C\left(T_0^{(1)}, \chi^{(1)}\right) + L_R\left(T_0^{(1)}\right) + H_0\left(T_0^{(1)}, \chi^{(1)}\right), \tag{2.11}$$

$$P_0^{(2)}(T_0^{(2)}) = C_p^{(2)} \frac{dT_0^{(2)}}{dt} + L_C\left(T_0^{(2)}, \chi^{(2)}\right) + L_R\left(T_0^{(2)}\right), \tag{2.12}$$

where the superscripts in parentheses refer to the scan numbers. Taking the difference between both equations for $T_0 = T_0^{(1)} = T_0^{(2)}$, and rearranging the terms leads to the following expression for the reaction enthalpy flow.

$$H_0\left(T_0,\chi^{(1)}\right)=\left(P_0^{(1)}(T_0)-P_0^{(2)}(T_0)\right)-\left(C_p^{(1)}\left(\frac{dT_0}{dt}\right)^{(1)}-C_p^{(2)}\left(\frac{dT_0}{dt}\right)^{(2)}\right)$$

$$-\left(L_C\left(T_0,\chi^{(1)}\right)-L_C\left(T_0,\chi^{(2)}\right)\right)$$

$$=\Delta P-\Delta\left(C_p\frac{dT_0}{dt}\right)-\Delta L_C, \tag{2.13}$$

in which the radiative heat loss term has been eliminated. Each of the terms in the RHS of Equation (2.13) is readily evaluated in a typical experiment. The first term represents the difference in power supplied in the two scans and is calculated from the applied current and resistance of the heating element using Equation (2.5). The second term arises because the enthalpy of the samples accrues at different rates in the two scans. Since scanning AC nanocalorimetry measurements provide the heat capacity of the CV as a function of temperature, Equation (2.7), this term is also easily calculated. Evaluation of this term represents a clear advantage of scanning AC nanocalorimetry over straight DC nanocalorimetry where this term is much more difficult to determine unless the two scans are performed at exactly the same heating rate in a power-compensated scheme and the heat capacity of the CV does not change after the reaction. The last term represents the difference in conductive heat loss as a result of the different temperature histories of the CV during the two scans. This term is well approximated by the following expression

$$L_C\left(T_0(t),\chi^{(1)}\right)-L_C\left(T_0(t),\chi^{(2)}\right)$$

$$=-(2k_mA_m)\frac{\partial}{\partial y}\left(\int_0^t\left(T_0^{(1)}(t')-T_0^{(2)}(t')\right)K_{\mathrm{m}}(t-t')dt'\right)|_{y=0}$$

$$-(2k_hA_h)\frac{\partial}{\partial x}\left(\int_0^t\left(T_0^{(1)}(t')-T_0^{(2)}(t')\right)K_{\mathrm{h}}(t-t')dt'\right)|_{x=0}, \tag{2.14}$$

where the subscript *m* refers to membrane properties, while *h* refers to properties obtained by appropriately averaging the heater and membrane properties. A detailed derivation of

this expression and the definition of the relevant parameters are found in Appendix A. This expression is evidently somewhat more cumbersome to evaluate. Appendix A also provides a numerical algorithm to accurately evaluate Equation (2.14).

In a typical experiment the current supplied to the sensor during the two scans is ramped up at the same rate and the difference in scan rates is caused by the enthalpy associated with a reaction. Consequently, the first term in Equation (2.13) arises because the resistance of the heating element is a function of temperature. This term is usually the dominant term in the expression for the reaction enthalpy flow. The difference in conduction heat loss arises solely as a result of the slightly different thermal histories of the scans and is typically quite small; the same is true for the term associated with the enthalpy. The radiative heat loss, which at elevated temperature is often the largest term in Equation (2.10), is automatically eliminated, although some care needs to be exercised if the solid-state reaction changes the emissivity of the CV. This effect shows up as a T^4-dependence of the reaction enthalpy flow at high temperatures and, if necessary, can be eliminated by fitting the experimental data over a temperature range where the enthalpy flow is expected to be zero.

To validate the analysis method and the algorithm to calculate the conduction loss, we constructed a finite element model (FEM) of the nanocalorimetry sensor using the commercial software package COMSOL Multiphysics 4.3a. Typical experiments were simulated using the FEM model and then analyzed using the procedure described above.

Table 2.1. Parameters used in the FEM [1, 3].

	Length (mm)	Width (mm)	Thickness (nm)	Heat Capacity ($J/kg \cdot K$)	Thermal Conductivity ($W/m \cdot K$)	Density (kg/m^3)	Emissivity
Membrane	5	2.5	200	700	3.2	3,000	0.18
CV	3.6	0.8	200	291	35.3	15,075	0.04
Heating element	5	0.8	200	267	23.4	12,650	0.04

The FEM model had the same in-plane dimensions as the nanocalorimetry sensor used for the measurements (Figure 2.1, Table 2.1). To save computational time, we constructed a two-dimensional model using properties averaged over the thickness of the sensor, which is a very good approximation for the real sensor since out-of-plane temperature gradients are entirely negligible in a typical measurement. The model was heated by sending a current through heating element. Since most measurements are performed in vacuum, only conductive and radiative heat losses were considered. The thermo-physical parameters of the sensor membrane and heating element used in the model (Table 2.1) were representative for the materials used in the sensors [1, 3]. The electrical resistance of the heating element was modeled as a linearly increasing function of temperature with a value of 8.2 W at 24°C and a temperature coefficient of resistance of 0.00115 K^{-1}, both values obtained from actual experiments. The emissivity of the top and bottom surfaces of the CV was chosen such that the heating rate in the FEM model was similar to the heating rate obtained in actual measurement. The specific heat of the CV was selected to make the value equal to that obtained in the measurements. During the simulations, the temperature of the edge of the membrane was fixed at 24°C. Two scans were simulated: one scan in which the sample released enthalpy as a result of a solid-state reaction (scan 1), and one in which it did not (scan 2). The reaction enthalpy

released during scan 1 was included in the FEM model as a heat source at the top surface of the CV. The solid-state reaction was modeled as an exothermic two-stage process with a shallow enthalpy peak at low temperature and a sharp peak at elevated temperature. Both peaks were modeled as Gaussian functions of time. The current supplied to the sensor was a DC current equivalent to the current used in the experiments and was given by $I = \sqrt{(15 + 33t)^2 + \frac{1}{2}(12 + 33t)^2}$ mA.

The results of the FEM simulations and the analysis are illustrated in Figure 2.2. Figure 2.2a shows the evolution of the temperature averaged over the CV during both scans. Initially the scans trace each other perfectly, but as the solid-state reaction proceeds the temperature during scan 1 is slightly larger than during scan 2. Figure 2.2b shows the three terms in the right hand side of Equation (2.13) that comprise the reaction enthalpy flow. The terms involving the power and the enthalpy difference can be calculated exactly from experimental data while the conduction loss difference is estimated from Equation (2.14). It is evident from the figure that the term associated with the power difference is dominant, while the conduction loss difference is the smallest. Figure 2.2c displays the conduction loss term as estimated from Equation (2.14) using the algorithm described in the Appendix A, along with the actual conduction loss difference obtained from the finite element simulations. Equation (2.14) provides a good estimate of the conduction loss difference at low temperature but the accuracy is diminished at temperatures in excess of 700°C where radiative loss from the membrane and heating element becomes significant. Given that the difference in conduction loss between the two samples is typically quite small, Equation (2.14) provides a reasonable estimate for the conduction correction over the temperature range considered. Figure 2.2d shows both

the reaction enthalpy determined from an analysis of the FEM results and the reaction enthalpy originally entered into the FEM model. Both curves are evidently in very good agreement, confirming the validity of the analysis. The enthalpies obtained from the FEM analysis and from the proposed method, agree to within 4%. Not taking into account the conduction loss difference increases the error to approximately 7%.

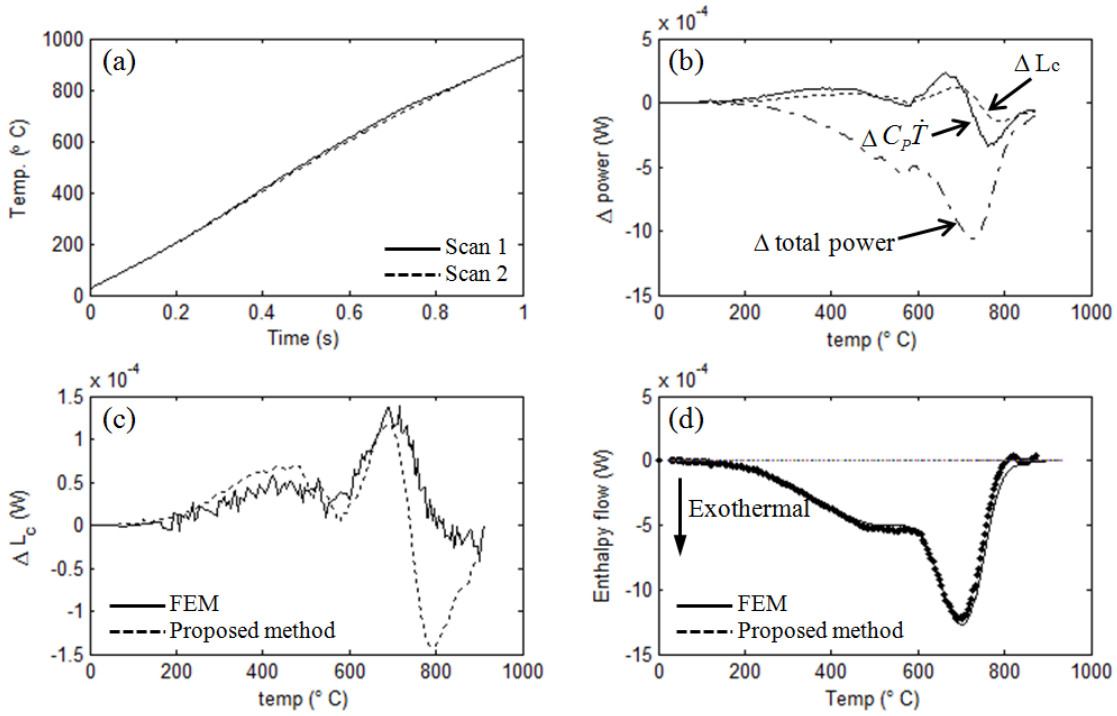


Figure 2.2. Validation of the data reduction method using a finite element model: (a) temperature versus time, (b) three power terms in the RHS of Equation (2.13), (c) difference in conduction loss versus temperature, and (d) enthalpy flow along with input enthalpy flow.

2.5 EXPERIMENTAL DETAILS

The PnSC device used for the reactive multilayer measurements was fabricated from a (100) single-crystal Si substrate employing standard Si-based micro-fabrication processes as described in detail in references [2, 48]. Each sensor on the PnSC device had a SiN_x membrane and a W heating element. The thickness of the membrane was 200 nm, while that of the heating element was 100 nm.

Before depositing the Zr/B multilayer, the PnSC sensors was stabilized and calibrated. To that effect, the sensors on the PnSC were resistively heated to a temperature of approximately 1,000°C, the maximum temperature range used in this study, for a period of 300 ms, and then cooled to room temperature. This thermal cycle resulted in a small shift in the resistance of the heating element because of microstructural changes in the W. This process was repeated until the resistance of the heater stabilized, typically after five thermal cycles. After conditioning, the temperature coefficient of resistance of each cell in the PnSC device was calibrated by heating the PnSC device over a temperature range from 20°C to 120°C in steps of 20°C. These measurements were performed inside a vacuum furnace with Ar gas at ambient pressure to ensure temperature uniformity within the furnace. The temperature coefficient of the resistance was then calculated using Equation (2.1).

After calibration of the sensors, Zr/B multilayer samples with a bilayer period of 50 nm were sputter deposited onto three sensors of the PnSC device, one for calorimetry measurements and two for additional transmission electron microscopy (TEM). The total thickness of the multilayers was 100 nm and the thickness of the individual layers was chosen to ensure that the sample would form stoichiometric ZrB_2 upon completion of the

reaction. The multilayers were deposited in a sputter chamber with confocal magnetrons (ATC 1800 system, AJA International) and a rotating substrate holder (10 rpm). The base pressure of the chamber was better than 10^{-7} Torr. Zr was deposited at a rate of 4.7 nm/min using a 99.99% Zr target (Ø 50.8 mm) and a DC power of 80 W. B was deposited at a rate of 0.5 nm/min using a 99.95% B target (Ø 50.8 mm) and an RF power of 150 W. The distance between substrate and targets was 120 mm. The temperature of the substrate was not controlled during the deposition process. To prevent oxidation of the samples during the measurements, the multilayer samples were coated with a 30 nm layer of SiN_x, by reactive sputtering from a Si target (DC 120 W, 5m Torr of Ar) in an N_2 (10sccm) environment.

The samples were deposited through a shadow mask to prevent deposition of material outside of the CV area (Figure 2.1c). The shadow mask was fabricated from a vacuum-compatible UV-cross-linkable polymer (VeroWhite, Stratasys Ltd., MN) using an Objet Connex500 3D printer (Stratasys Ltd., MN) in the high-quality print mode. As a result of shadowing by the mask, the thickness of the samples varied 70 nm at the edge to 100 nm in the center, as determined by transmission electron microscopy observation. The mass of the samples was estimated at 1.05 μg from the room-temperature heat capacity, in good agreement with the value determined from the deposition flux and the area of the shadow mask windows.

Table 2.2. Summary of the parameters of Zr/B multilayer samples and measurements

DC current, I_0 (mA)	AC current, i (mA)	frequency (Hz)	duration (ms)	heating rate (K/s)
15 – 48	12 - 45	987	1,000	600 - 1,400

Parameters for the scanning AC nanocalorimetry measurements were chosen based on Equations (2.5, 2.6) and are shown in Table 2.2. The calorimetry measurements in this study consisted of two successive scans: scan 1 and scan 2. The multilayer samples reacted during scan 1 and this scan contains the calorimetric signature of the reaction. No reaction took place during scan 2 and this scan was used as a baseline for the first scan. All nanocalorimetry measurements in this study were performed in vacuum to minimize heat loss to the environment using a custom low-noise data acquisition system described in detail in reference [3]. Typical noise levels in the measurements were on the order of 0.1%. The experimental nanocalorimetry data were analyzed following the data reduction algorithm described earlier; the material parameters used in the analysis were obtained from calibration runs on similar devices [1] and are listed in Table 2.2. The heat capacity of the CV was calculated from the $2w$ - harmonic in the voltage across the heating element using Equation (2.5).

Cross-sections of the three multilayer samples were investigated by TEM using a JEOL 2010 system operating at 200 KeV. To prepare the TEM samples, 10 μm x 2μm blocks were isolated from the samples of interest using a (30 keV, 150pA) focused beam of Ga ions inside a Zeiss NVision 40 Dual-Beam system. These blocks were attached to an Omniprobe and further thinned to a thickness of approximately 100nm using a 30 KeV, 40pA Ga ion beam inside the FIB. Finally, Ar ion milling was performed in a Nanomill 1040 operating at 500 eV to achieve electron transparency and to remove any Ga ions introduced by the focused ion beam. Each specimen was exposed to the electron beam on both sides for a period of 10 minutes with the gun current set at 140 pA.

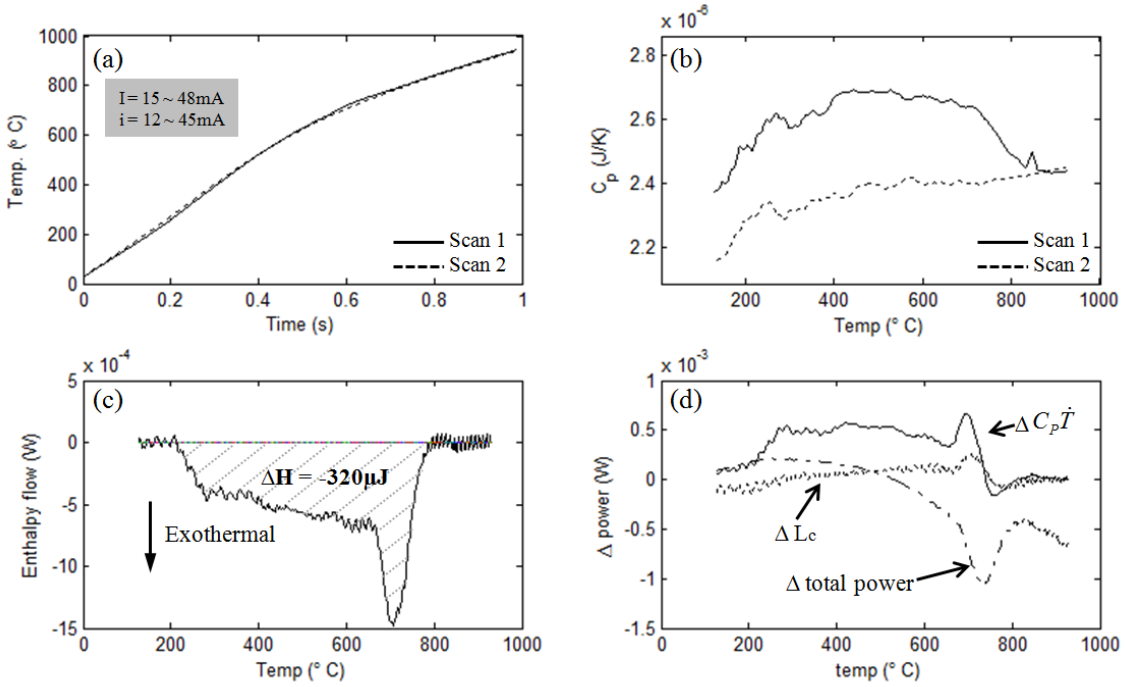


Figure 2.3. AC nanocalorimetry measurement results for the Zr/B multilayer: (a) average temperature history, (b) C_p versus temperature obtained from AC measurement, (c) enthalpy flow, and (d) the three terms in the RHS of Equation (2.13). To calculate the enthalpy flow a small correction corresponding to a change in emissivity of 2.2% was applied.

2.6 RESULTS

The results of the scanning AC nanocalorimetry measurements on the first multilayer sample are depicted in Figure 2.3. Figure 2.3a shows the temperature response of the sample for the two successive scans. Both curves very nearly trace each other with just a few subtle differences: Initially the slope for scan 2 is slightly greater than for scan 1 indicating that the solid-state reaction has reduced the heat capacity of the multilayer sample. Later on, the temperature in scan 1 is slightly larger than in scan 2 because of the exothermic reaction between Zr and B. At elevated temperatures, the slopes of both temperature curves decline because of significant radiative heat loss. Figure 2.3b shows the heat capacity of the CV obtained from the 2*w*-signal as a function of temperature for both scans. The heat capacity for scan 1 is larger than for scan 2 and increases slightly with temperature until approximately 720°C, when it suddenly decreases to overlap with the heat capacity for scan 2. As will be demonstrated later, this change coincides with the formation of crystalline ZrB_2 in the sample. Figure 2.3c depicts as a function of temperature the reaction enthalpy flow for the Zr/B multilayer, obtained from the three terms in Figure 2.3d. It is evident from the figure that the reaction in the multilayer proceeds in two stages: there is a broad exothermal peak at low temperature (200 – 650°C), followed by a sharp exothermic peak at more elevated temperature (650 – 800◦C). The total enthalpy of the Zr/B reaction is calculated at -320 μJ by integrating the reaction enthalpy flow with respect to time. Figure 2.3d shows $\Delta P, \Delta\left(C_p dT_0/dt\right),$ and ΔL_C as a function of temperature. As for the FEM simulations, the power term dominates, while the conduction loss term is quite small. While nanocalorimetry clearly demonstrates that the solid-state reaction in the Zr/B multilayer

proceeds in two stages, it does not provide insight in the precise nature of these stages. That insight is provided by TEM analysis of the samples.

Figure 2.4 shows bright-field TEM micrographs of an unreacted Zr/B multilayer in cross section. The micrographs clearly reveal a crystalline Zr layer (Powder Diffraction File #050665), an amorphous B layer, and an amorphous intermixed layer of Zr and B between them. The thickness of the intermixed layer is approximately 5nm and quite uniform throughout the TEM sample. The Zr layer shows a large variation in grain size, from a few nanometers (Figure 2.4b) to a few tens of nanometers (Figure 2.4a); no grains were detected in the B layers.

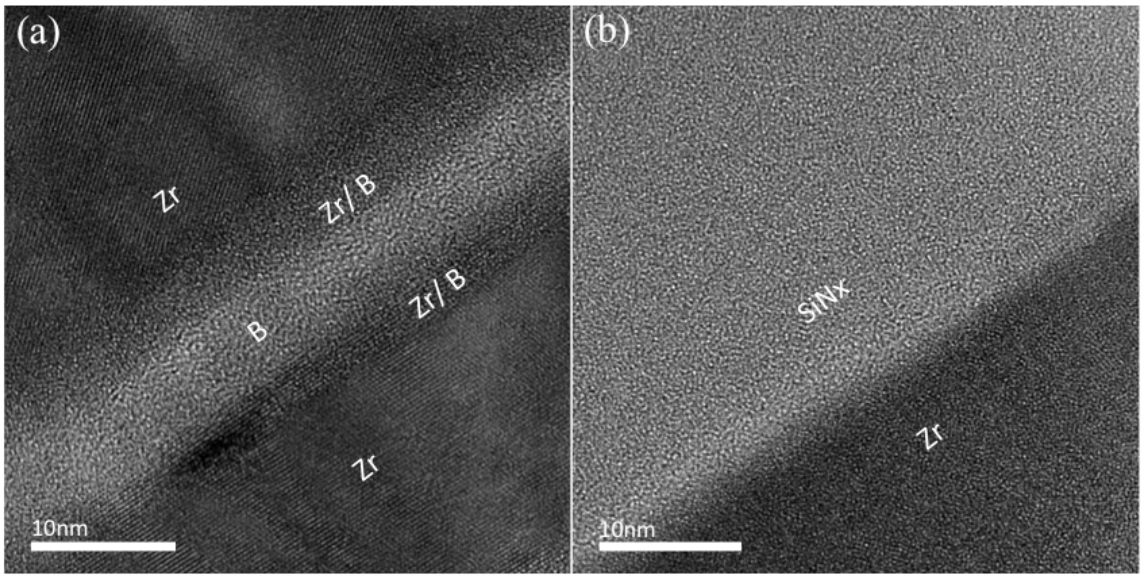


Figure 2.4. Cross-sectional transmission electron micrographs of an unreacted Zr/B multilayer. (a) Crystalline Zr layers and an amorphous B layer. Amorphous Zr/B intermixed layers were found between the Zr and B layers. (b) TEM image of a nano-crystalline Zr layer. The inset in each figure is the Fourier transformation of the dashed box in the same figure.

To determine the nature of the two stages in the reaction, a nanocalorimetry measurement was performed on a second Zr/B multilayer sample, interrupting the measurement at a temperature of 450°C, before the second stage of the reaction set in, in essence freezing in the structure that develops during the first stage of the reaction. The corresponding TEM micrographs are shown in Figure 2.5. The images show clear interdiffusion of the Zr and B layers, but in a very heterogeneous fashion: some regions of the TEM specimen have little interdiffusion (Figures a, d) and are comparable to the unreacted sample, while other regions show significant interdiffusion (tens of nanometers as in Figures b, e, f), resulting in the formation of an amorphous Zr-B alloy. This heterogeneous interdiffusion of Zr and B is not observed in the unreacted sample and indicates that the first stage of the multilayer reaction corresponds to a process of Zr and B interdiffusion at specific sites along the Zr/B interfaces**.** Only Zr grains were observed in this sample as illustrated by the electron diffraction images in Figure 2.5c; no crystalline ZrB_2 phase was identified. As in the unreacted sample, large variations in Zr grain size were observed.

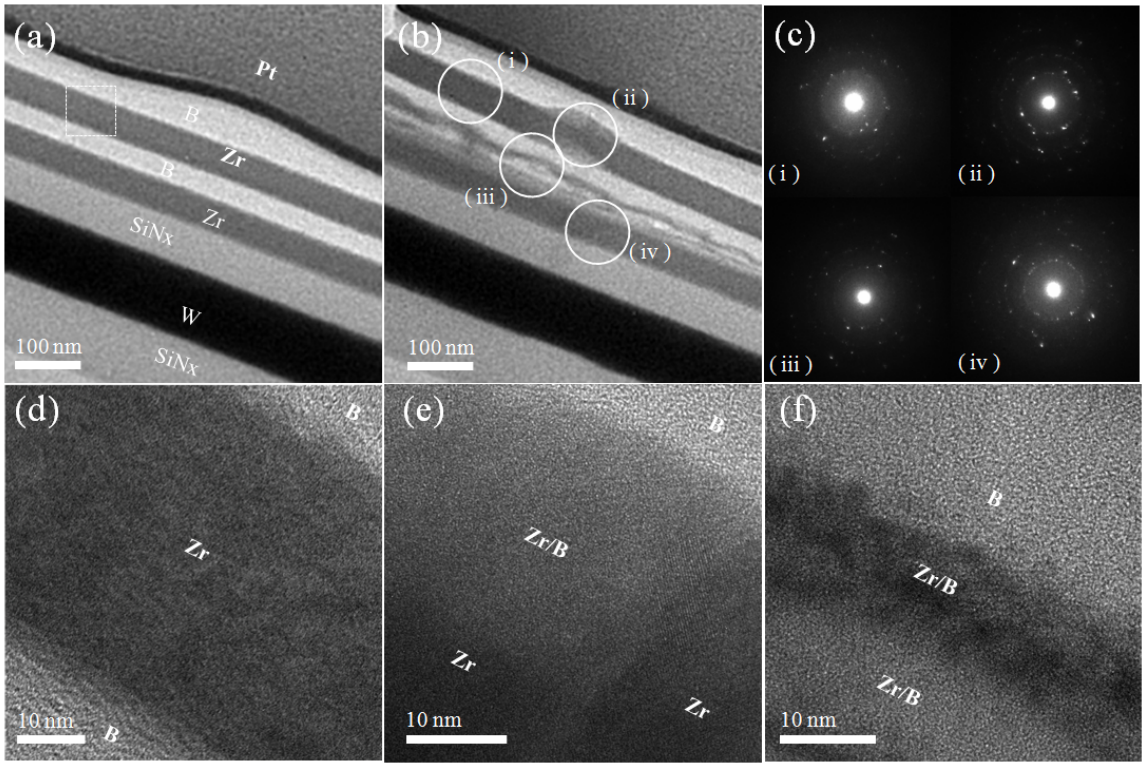


Figure 2.5. Cross-section TEM micrographs of a Zr/B multilayer heated up to 450°C. The specimen consists of parts with either narrow (a) or wide (b) interdiffused layers. (c) Diffraction patterns obtained from the corresponding circled areas in (b) High-resolution images in (d), (e), and (f) were obtained from the inset in (a) and from (ii), (iii) in (b), respectively.

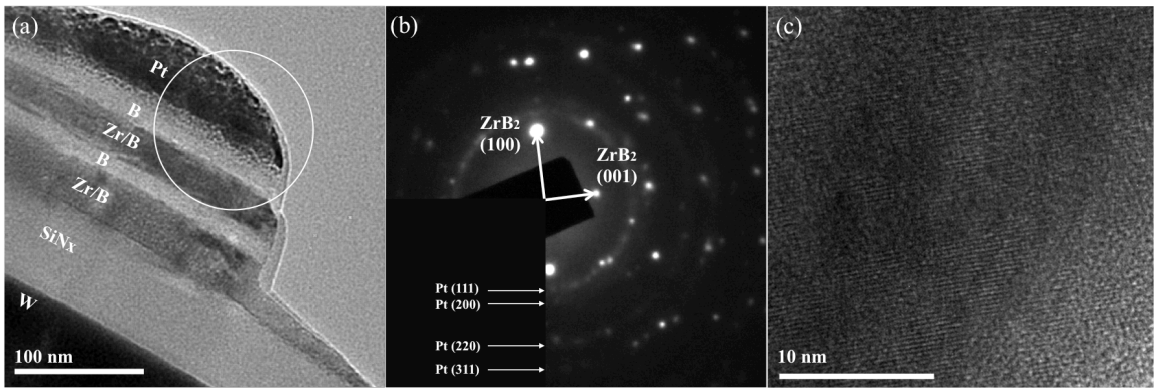


Figure 2.6. (a) TEM micrograph of a Zr/B multilayer heated up to 950°C. (b) Electron diffraction pattern obtained from the circled area in (a). Diffraction spots for ZrB_2 and for nano-crystalline Pt are clearly visible. (c) HRTEM image of a crystalline Zr in the same sample. The inset in the figure shows the Fourier transformation of the dashed box.

Figure 2.6 shows TEM micrographs for the Zr/B multilayer sample that was used for the nanocalorimetry measurements. The bright-field TEM micrograph in Figure 2.6a demonstrates that the microstructure of the sample is not homogeneous, even after heating to 950°C. It consists of dark Zr/B layers along with some unreacted B. Electron diffraction measurements on the dark layers in Figure 2.6a show that this layer contains a mixture of ZrB_2 and Zr grains. The selected area diffraction pattern in Figure 2.6b, for instance, agrees well with the Powder Diffraction File #751050 for ZrB_2, but HRTEM micrographs (Figure 2.6c) obtained at other locations in the same sample showed crystalline Zr (Powder Diffraction File #050665). No other ZrB-phases were observed. The micrographs indicate that the second stage of the multilayer reaction consists of the formation of crystalline ZrB_2 from the amorphous Zr/B mixture that forms in the first stage. Given that the Zr/B layer consists of both Zr and ZrB_2, it is likely that scans to even higher temperatures would result in the formation of additional ZrB_2, although the micrographs suggest that the samples had an excess of B, which would prevent total conversion to ZrB_2.

2.7 DISCUSSION

The scanning AC nanocalorimetry measurements have clearly identified two distinct stages in the Zr/B solid-state reaction: an exothermal reaction that occurs over a broad range of relatively low temperatures and an elevated-temperature exothermic reaction that occurs over a narrow range of temperatures. We attribute the first reaction to diffusion of Zr and B and the formation of an amorphous Zr/B alloy. There is no evidence that any crystalline Zr-B compounds form at this stage. The amorphous alloy

seems to form at certain preferred sites at the Zr/B interfaces resulting in a very non-uniform distribution of the alloy. Heterogeneous diffusion in multilayers has been observed in other multilayers that alternate amorphous and crystalline layers. In particular multilayers coatings that consist of crystalline Ni and amorphous NiP_y alloys show limited interdiffusion and do not completely homogenize on annealing [49]. The extent of diffusion in these multilayers is controlled by the crystalline layer and by the rate at which P diffuses into the Ni grain boundaries in particular. We suggest here that the broad range of Zr grain sizes from just a few nanometers to several tens of nanometers is responsible for the heterogeneous diffusion of B. If B diffuses predominantly along the Zr grain boundaries, the amorphous Zr/B alloy is expected to form in the regions with nano-crystalline Zr, while regions with larger Zr grains should have much lower B concentrations. The fact that the diffusion process occurs over a broad range of temperatures further suggests that diffusion occurs via a range of pathways with a distribution of relatively low activation energies – a thermally activated process with a well defined activation energy results in a sharp peak in a calorimetry trace obtained at constant scan rate.

The TEM images show that the second stage in the solid-state reaction is associated with the formation of crystalline ZrB_2. The conversion to ZrB_2 is not complete, however, and significant amounts of Zr and B remain. Specifically ZrB_2 grains form in some areas of the sample and not in others. It is likely then that the ZrB_2 grains grow only in those areas of the sample that form the amorphous Zr/B alloy during the first stage, i.e., the second stage corresponds to the crystallization of the amorphous Zr/B alloy formed in the first stage. This observation implies that the microstructure of the Zr layers is critical

to obtaining full conversion to ZrB_2, at least in the temperature range considered in this study. Figure 2.3b shows that crystallization of the amorphous Zr/B alloy is associated with a decrease of the heat capacity of the sample. While the heat capacity of ZrB_2 is nearly the same as the heat capacity of the equivalent amount of crystalline Zr and B [50], the figure suggests that the heat capacity of the amorphous phase is larger than that of ZrB_2.

A recent study on reactive hot pressing of Zr and B powders using differential thermal analysis [51] showed that the reaction between Zr and B occurs over a broad temperature range from 300 to 900°C, following a two-step process. It is likely that this process also consists of a combination of interdiffusion and crystallization processes, although diffusion in this case may be controlled by the presence of a native oxide on the Zr grains. Calorimetric studies of the solid-state reactions in Nb/Al multilayers have also revealed double peaks similar to those observed for Zr/B in this study. In the case of Nb/Al, however, the first peak is the result of an interface-limited reaction, while the second peak is associated with a diffusion-limited reaction regime [52].

The enthalpy of the Zr/B solid-state reaction is estimated at 36 kJ/mol, which is significantly smaller than the value of 297 – 323 kJ/mol reported in theoretical and experimental studies on ZrB_2 [28, 53]. The low value of the enthalpy is consistent with the incomplete reaction of B and Zr observed in the TEM and suggests that only about 12% of the sample reacted to form ZrB_2[*]. Although it is difficult to confirm the conversion rate quantitatively in the TEM, we believe that this number slightly underestimates the

[*] As will be discussed in Chapter 3, we have found that full conversion to ZrB_2 from MRNLs can be achieved by optimizing the sample preparation procedure. For instance, the impurity level of the sputtering chamber can be substantially lowered by pre-sputtering Zr before MRNL depositions.

actual conversion rate because of some intermixing of Zr and B during the deposition process as observed in the unreacted sample. The largest source of error in the conversion rate is the noise in the PnSC voltage measurements (0.1%), which causes an error of approximately 10% in the enthalpy flow. The uncertainty in the mass of the multilayer sample is estimated at 8%. Given that the Zr/B reaction is very exothermic [28, 53], it may be possible to use Zr/B multilayers as a heat source [43-47] for brazing of ultrahigh-temperature ceramics. For this application, it will be necessary, however, to significantly increase the conversion rate of the reaction through optimization of the multilayer deposition process. The conversion rate may be further enhanced by increasing the total thickness of the sample, which would reduce the heat loss relative to the reaction enthalpy and thus allow the sample to reach a higher temperature.

Finally, it should be pointed out that scanning AC nanocalorimetry combined with the relatively simple data reduction method described in this article is a promising technique for the characterization of reactions in reactive multilayers and of solid-state reactions more generally. The technique provides the same thermodynamic information for thin films as macroscopic calorimetry – one of the most useful tools in the study of materials – for bulk materials. Furthermore, scanning AC nanocalorimetry can access a very wide range of scanning rates making it a useful tool for kinetics studies.

2.8 SUMMARY

AC nanocalorimetry combined with the data reduction procedure discussed in the present article makes it possible to measure both heat capacities and reaction enthalpies for thin-film samples, making it the ideal tool for studying solid-state reaction in

multilayer samples. This technique has been applied to characterize the Zr/B multilayer reaction. The reaction proceeds in two stages, both of which are exothermic: interdiffusion of Zr and B resulting in an amorphous Zr/B alloy and crystallization of this alloy to form ZrB_2. The interdiffusion process occurs in a heterogeneous fashion at relatively low temperatures, while the crystallization process occurs at more elevated temperatures. As the ZrB_2 formation reaction is very exothermic, Zr/B multilayers may be useful in brazing applications of high-temperature ceramics, provided the conversion rate can be further improved through optimization of the multilayer deposition process.

Chapter 3. Low temperature synthesis of ZrB_2 via MRNLs*

*Reprinted with permission from D. Lee, G.D. Sim, K. Xiao, and J. J. Vlassak, The Journal of Physical Chemistry C 118 (36), 21192-21198 (2014). Copyright 2014, American Chemical Society

3.1 INTRODUCTION

ZrB_2 is an ultra high-temperature ceramic (UHTC) with a unique set of properties, including an extremely high melting point, very high hardness, exceptional resistance to erosion, and excellent thermal and electric conductivity. Due to this combination of properties, ZrB_2 has garnered intense attention as a structural material in extreme environments, such as propulsion systems, leading edges of hypersonic flight vehicles, and heat shields for atmospheric re-entry [8, 13, 29]. Practical application of ZrB_2, however, has been impeded because of its poor sinterability. ZrB_2 is conventionally fabricated using hot pressing (HP), spark plasma sintering (SPS), or pressure-less sintering (PS), processes that require very high temperature (> 2,200 K) to achieve dense ZrB_2 structures [29]. Even with applied pressures as high as 40 MPa, formation of pure ZrB_2 requires temperatures in excess of 1,950 K to achieve full density [29, 54]. A great deal of research has been conducted in an attempt to enhance the sinterability of ZrB_2 by refining the particle size of the raw materials and by including additives such as C, SiC,

B_4C, WC, B_2O_3 or $MoSi_2$ [29, 54-61]. Utilizing these methods, recent studies have demonstrated processing temperatures of dense ZrB_2 as low as 1,750 K in the presence of additives.

Here we demonstrate that it is possible to synthesize crystalline ZrB_2 at temperatures below 1,300 K through use of Zr/B reactive multilayers. As shown schematically in Figure 3.1a, a reactive multilayer consists of alternating Zr and B layers with a nominal stoichiometry of 1:2. Upon heating, Zr and B react to form ZrB_2 in an exothermic process. We have used nanocalorimetry (Figure 3.1b and c) combined with transmission electron microscopy (TEM) to explore the nature of the solid-state reaction and the structural changes that occur in the multilayer. Calorimetry has been used extensively to examine the thermodynamics and kinetics of multilayer reactions [19, 21, 24, 52, 62-66]. Nanocalorimetry sensors can significantly enhance the study of these solid-state reactions because of their extraordinary sensitivity and extremely small thermal mass [17, 67, 68]. These features make it possible to perform measurements on very thin multilayers over a much broader range of heating rates than traditional calorimetry, ranging from isothermal to 10^5 K/s [1, 17, 67, 69-75]. Current nanocalorimetry sensor designs allow measurements at temperatures as high as 1,500 K [6].

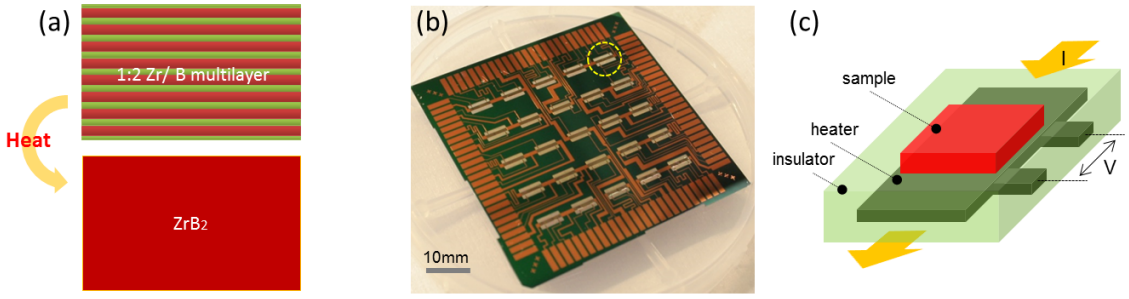


Figure 3.1. Nanocalorimetry analysis of the Zr/B solid-state reaction: (a) Schematic representation of the cross-section structure of a Zr/B reactive multilayer, before and after reaction. (b) PnSC device with 25 nanocalorimetry sensors. (b) A schematic representation of a nanocalorimetry sensor with a 4-point measurement scheme.

3.2 EXPERIMENTAL

All nanocalorimetry measurements were performed using a parallel nano-scanning calorimeter (PnSC) [1, 2]. This device consists of a 5x5 array of micromachined calorimetry sensors (Figure 3.1b). Each sensor consists of a thin metal layer that is patterned to serve both as a heating element and a resistance thermometer in a four-point measurement scheme. As illustrated schematically in Figure 3.1c, this heating element/thermometer is encapsulated in a thin membrane that insulates the heating element from its surroundings. The sample of interest is deposited in the area between the voltage leads as indicated in Figure 3.1c. To perform a calorimetry scan, an electric current is supplied through the heating element, which results in Joule heating of sample and addendum. The measured current and voltage are used to determine the power supplied to the sensor and the resistance of the heating element, which is calibrated to temperature.

The PnSC device in this study was designed for high-temperature measurements. Specifically, the heating element was fabricated from a 100 nm thick W-Ti alloy film with a high recrystallization temperature [76], extending the operating temperature to 1,500 K. The membrane was fabricated from Si_3N_4 with a total thickness of approximately.

Before depositing the Zr/B multilayer on the nanocalorimetry sensors, the sensors were stabilized and calibrated. The sensors were stabilized by resistively heating them to 1,400 K for 50 thermal cycles, each one of which had a duration of 1.5 sec. These thermal cycles resulted in a small decrease in the room temperature resistance of the heating element because of microstructural changes in the Ti/W alloy. Once the

resistance of the heating element was stable, the temperature coefficient of resistance (TCR) of each sensor in the PnSC device was measured by heating the device in an Ar-filled vacuum furnace and by recording the resistance as a function of temperature from 302 K to 452 K in steps of 30 K. High-temperature calibration data was obtained by melting 100 nm Ag samples on select sensors.

After calibration of the sensors, Zr/B multilayer samples with bilayer periods of 4.1 and 8.3 nm were deposited onto the sensors of the PnSC device using magnetron sputtering. All samples in this study had a total thickness of 66 nm and the thicknesses of the individual layers comprising the multilayer were chosen to ensure formation of stoichiometric ZrB_2 on completion of the reaction. The multilayers were deposited using an ATC 1800 system (AJA International) with a base pressure of $< 2 \times 10^{-7}$ Torr and an Ar working pressure of 5 mTorr. To ensure uniformity, the substrate holder was rotated at 10 rpm during the deposition process; the temperature of the substrate holder was not controlled. Zr was deposited at a rate of 4.8 nm/min using a 99.99% Zr target (Ø 50.8 mm) and a DC power of 80 W. B was deposited at a rate of 0.2 nm/min using a 99.95% B target (Ø 50.8 mm) and an RF power of 150 W. Before any multilayer sample deposition, Zr and B were sputter deposited on a dummy substrate for an hour to lower the impurity levels in the chamber as well as to remove native oxide layers in Zr and B targets. The multilayer coating was started and terminated with half layers of B, to impose periodic boundary conditions. To prevent oxidation of the samples during the measurements, a 30 nm Si_3N_4 capping layer was sputter deposited (RF 150 W, 4mTorr of Ar) on top of the multilayer, immediately after deposition of the multilayer and without breaking vacuum. All samples were deposited through a custom-fabricated Si-shadow mask. The mass of

the samples was estimated from the deposition flux and the area of the windows in the shadow mask to be 660 ± 70 ng.

All nanocalorimetry measurements were performed using a custom-built, low-noise data acquisition system described in detail in Xiao et al [72]. Typical noise levels in the measurements were less than 0.1%. AC measurements were performed at a heating rate of approximately 3,000 K/s and an angular frequency of 3,272.5 rad/s, using AC and DC current components in accordance with the selection criteria in Xiao et al [72]. For the AC measurements, the in-phase and out-of-phase response of the sensor was determined by dividing measured voltage and current signals into segments consisting of an integer number of AC oscillation periods, and applying a discrete Fourier transform to every segment as described by Xiao et al [40, 72]. AC measurements were performed on three different multilayer samples to measure the heat capacity, C_p, as a function of temperature, both before and after reaction. DC scanning measurements were performed on other multilayer samples to investigate the kinetics of the solid-state reaction. Measurements were carried out at nominal heating rates of 3,100, 5,200, 7,000, 8,600, and 10,000 K/s. For these measurements, both the temperature of the sample and the power supplied to it were determined directly from the heating element as described earlier. Each of the DC measurements consisted of three successive scans. The multilayer samples reacted during the first scan and this scan contained the calorimetric signature of the solid-state reaction. The second scan was used to establish a baseline for the first scan. The third scan was performed and compared with the second scan to confirm that the reaction was complete after the first scan. All nanocalorimetry measurements in this study were made in vacuum ($< 1 \times 10^{-6}$ Torr) to minimize any heat loss to the

environment. The results from the DC scans were combined with the C_p data from the AC scans to determine the enthalpy released during the multilayer reaction. The data reduction algorithm used to analyze the calorimetric signal of the solid-state reaction and to determine the heat flow rate during the reaction can be found in detail in Chapter 2.

Cross-sectional TEM micrographs and selected area diffraction patterns (SADP) were acquired using a JEOL 2100 system operating at 200 KeV. To prepare the TEM samples, 10 x 2 μm^2 blocks were isolated from the samples of interest using a focused beam of Ga ions (30 keV, 150 pA) inside a Zeiss NVision 40 Dual-Beam system. These blocks were attached to an Omniprobe and further thinned to approximately 100 nm using a 30 KeV, 40 pA Ga ion beam. Finally, Ar ion milling was performed in a Nanomill 1040 operating at 500 eV and 140 pA to ensure electron transparency and to remove any Ga ions introduced by the focused ion beam.

3.3 RESULTS AND DISCUSSION

3.3.1 Nanocalorimetry and TEM studies on Zr/B MRNLs

Figure 3.2a depicts temperature as a function of time for typical DC scans performed on multilayer samples. It is evident that the first temperature scan performed on a sample has a section where the heating rate first increases and then decreases, while the subsequent scan does not. This section starts around 500 K and is the result of exothermic reactions that take place in the samples. Figure 3.2b presents the heat capacity of a multilayer sample with an 8.3 nm bilayer period and addendum measured using AC

scans. The heat capacities of the unreacted and reacted multilayers are essentially indistinguishable and rise slowly with temperature.

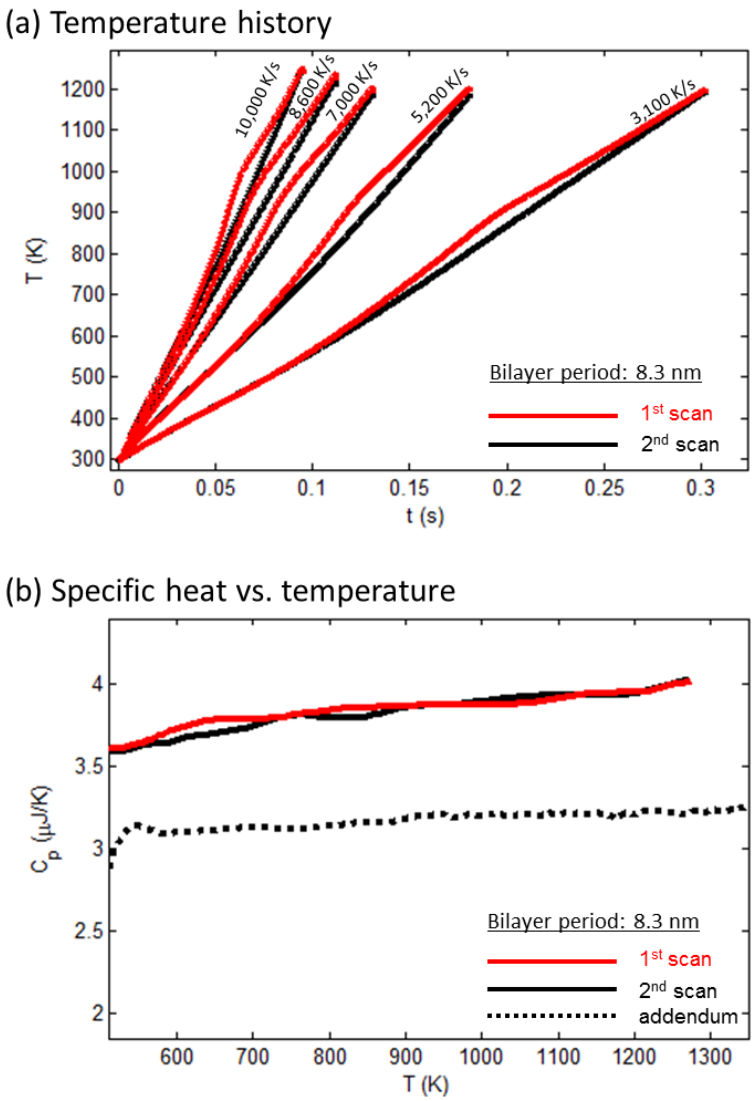


Figure 3.2. (a) Temperature histories for the Zr/B multilayer samples with a bilayer period of 8.3 nm. (b) Heat capacity of a multilayer sample with a 8.3 nm bilayer period and addendum (solid lines) and heat capacity of addendum (dotted line) obtained from AC measurements.

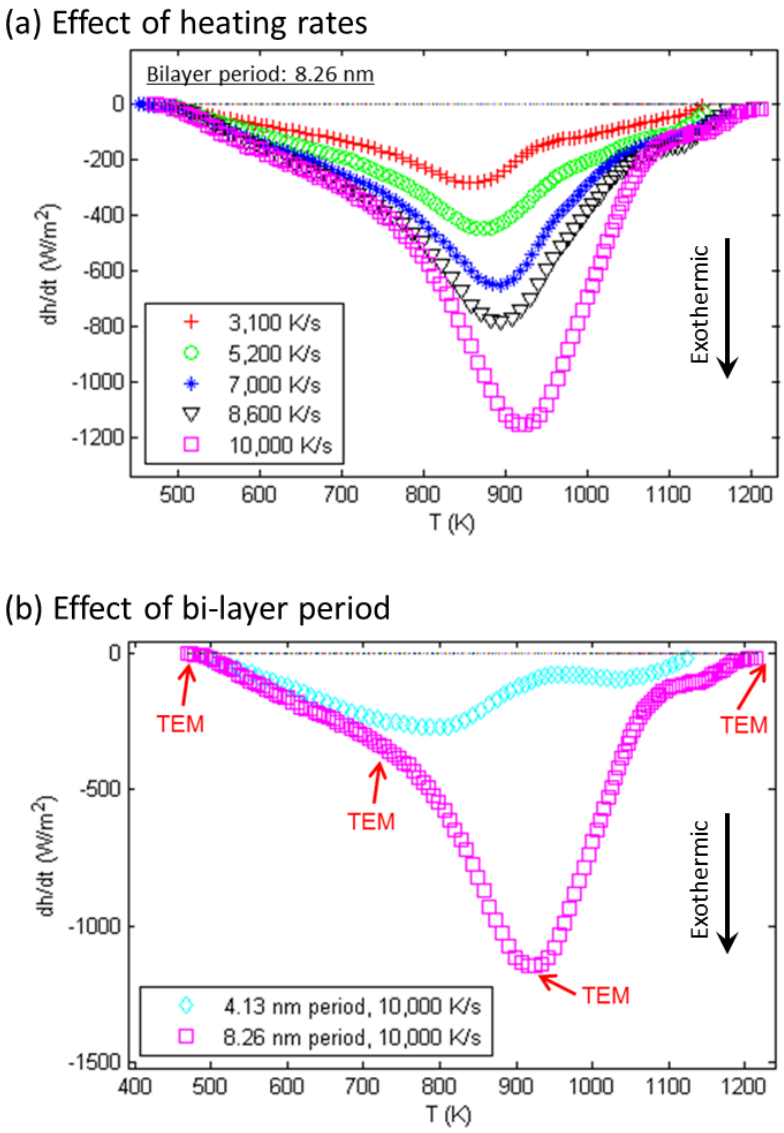


Figure 3.3. Heat flow rate per unit area of Zr/B multilayer reactions: (a) Heat flow rate per unit area vs. temperature for the Zr/B multilayer samples with a bilayer period of 8.3nm. (b) Heat flow rate per unit area for the multilayer samples with bilayer periods of 4.1 and 8.3 nm and with a heating rate of 10,000 K/s. Temperatures from which samples were quenched for TEM observations have been marked with arrows.

The temperature histories of the samples can be used to calculate the heat flow rates produced by the Zr/B reaction. Figure 3.3 displays the heat flow rate per unit area as a function of temperature. Figure 3.3a shows the effect of scan rate, while Figure 3.3b reveals the effect of the bilayer period of the multilayers. The scans reveal two separate exothermic reactions: a reaction with a strong enthalpy signal and a reaction with a much weaker enthalpy signal at a slightly higher temperature. Figure 3.3a shows that both peaks shift to higher temperatures as the heating rate increases. Figure 3.3b clearly demonstrates that the two peaks become more distinct with decreasing bilayer period. We now show that the first peak corresponds to the amorphization of the Zr/B multilayers as a result of interdiffusion of B and Zr, while the second peak is associated with the crystallization of the amorphous Zr/B alloy.

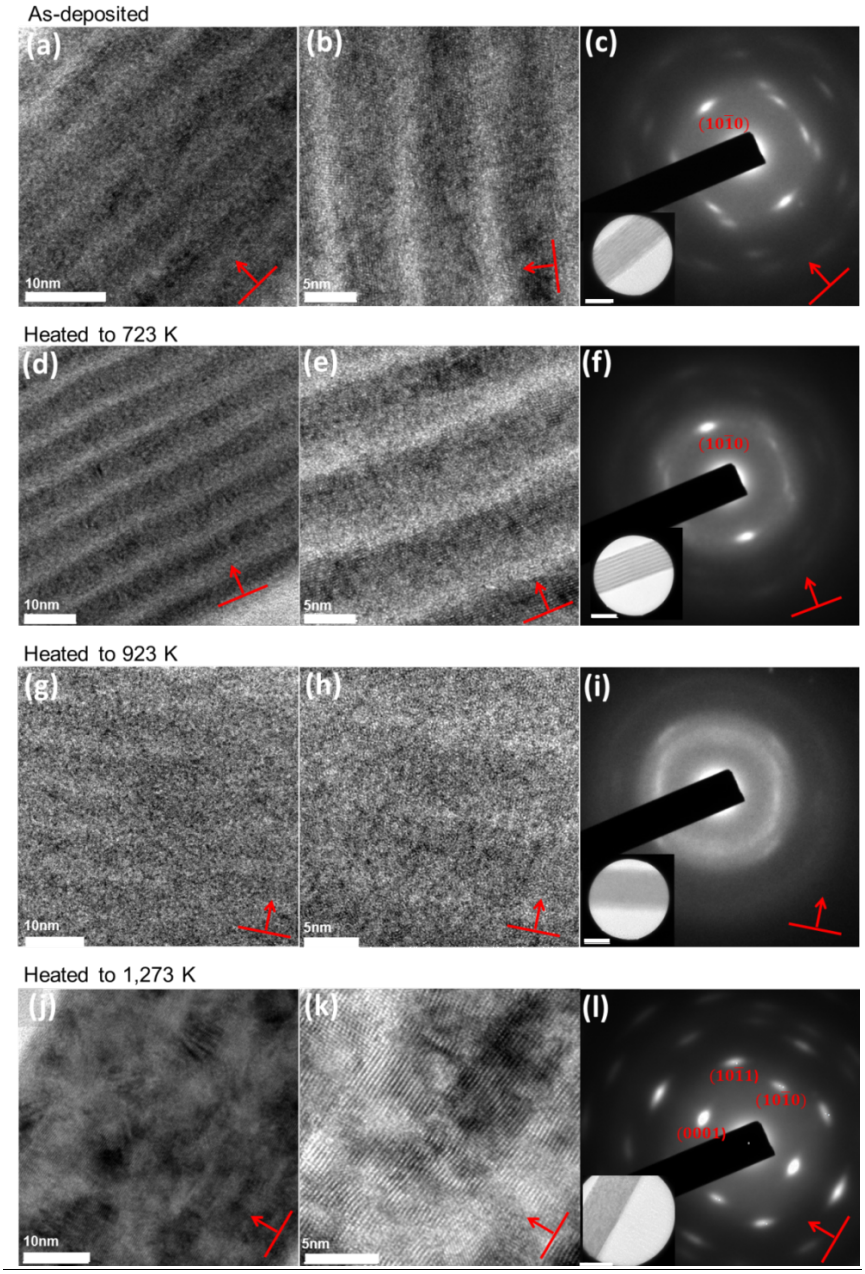


Figure 3.4. TEM observations on an as-deposited sample (a-c), a sample heated to 723 K (d-f), a sample heated to 923 K (g-i), and a fully reacted sample (j-l): (a, b, d, e, g, h, j, k) Bright-field images are shown for the four different samples. The sample normal are indicated by the arrows. (c, f, i, l) Selected area diffraction patterns obtained from the areas indicated in insets. The scale bars in the insets are 50 nm. All samples had a bilayer period of 8.3 nm and were heated to the relevant temperature at a nominal rate of 10,000 K/s, before being quenched to room temperature.

Figure 3.4 presents a series of TEM cross-sections that illustrate the reaction sequence. The micrographs were taken on samples that were heated to the temperatures marked by the arrows in Figure 3.3b, i.e., samples that were heated through different stages of the reaction before being quenched. The bright-field images in Figures 3.4a and b clearly show that as-deposited samples have a structure that consists of alternating layers of amorphous B (light) and crystalline Zr (dark). Figure 3.4c shows an electron diffraction pattern for the Zr layers, which indicates that as-deposited Zr layers have a $(10\bar{1}0)$ crystallographic texture (Powder Diffraction File #050665). No other phases have been identified from the diffraction pattern other than hcp Zr crystalline, indicating tha the initially intermixed layer is amorphous. Figures 3.4d-f and Figures 3.4g-i show micrographs for samples heated to 723 and 923 K, respectively. It is evident that the Zr and B layers in these samples have interdiffused and have started to form an amorphous Zr/B alloy. At 723 K, the layered structure of the sample is still present, but the Zr diffraction pattern in Figure 3.4f is more diffuse, indicative of the onset of amorphization. At 923 K, the peak temperature for the first reaction, the layered structure is mostly gone (Figure 3.4g, h) and the diffraction pattern is now a diffuse halo (Figure 3.4i), typical for an amorphous material. A few weak diffraction spots can still be discerned, however, indicating that the amorphization process is not yet complete at this temperature. Figures 3.4j-l show the results for a sample heated to 1,273 K, well above the temperature at which the second reaction is complete. The change in structure is dramatic: the sample now consists of crystalline ZrB_2 with a (0001) texture (Powder Diffraction File #340423). No other crystalline phases from the Zr-B phase diagram are observed. Evidently the second peak in the heat flow rate corresponds to the crystallization of the

amorphous Zr/B alloy to form the ZrB_2 compound. The ZrB_2 has a (0001) texture, which is somewhat surprising given that the ZrB_2 alloy is amorphous. The texture is a strong indication that the crystalline phase nucleated at the top or bottom interface of the multilayer coating, or possibly at the original locations of the Zr/B interfaces.

3.3.2 Thermodynamics and kinetics of the reactions in Zr/B MRNLs

The reaction sequence explains the observation in Figure 3.3b that the first enthalpy peak shifts to a lower temperature with decreasing bilayer period. As the bilayer period decreases, so does the diffusion distance, allowing intermixing of the two phases at lower temperature for a fixed heating rate. Integrating the heat flow rates in Figure 3.3 with respect to time provides the formation enthalpy of the ZrB_2 compound. The formation enthalpy measured for the samples with a bilayer period of 8.3 nm is 190 ± 23 kJ/mol, while that for the samples with a bilayer period of 4.1 nm is 74 ± 23 kJ/mol, respectively 64% and 25% of the formation enthalpy of bulk ZrB_2 [28, 77]. The TEM micrographs indicate a complete conversion of the multilayer to ZrB_2. Consequently the formation enthalpy deficit can be attributed to intermixing of Zr and B during the deposition process. The enthalpy values are consistent with an intermixed layer of approximately 1.5 nm. Intermixing has also been observed in other multilayer systems [19, 62].

The first step in the reaction sequence involves the formation of an amorphous phase caused by the interdiffusion of B and Zr. As discussed in Appendix B, the kinetics

of this process can be determined from the heat flow rate curves in Figure 3.3 using a simple one-dimensional diffusion model. According to this diffusion model, there exists a simple relationship between the enthalpy released in the reaction and the absolute temperature,

$$\ln\left((H + H_o)\frac{dH}{dt}\right) = 2ln\left(\frac{\alpha\Delta H\sqrt{2D_o}}{t_{Zr}}\right) - \frac{E_d}{k_B T}, \tag{3.1}$$

where H_o is the enthalpy associated with the intermixing, a is a constant defined in Appendix B, ΔH is the enthalpy of mixing associated with one bilayer period l, t_{Zr} is the thickness of the Zr layers, k_B is the Boltzmann constant, E_d is the diffusion activation energy, and D_o is the pre-exponential factor of the diffusivity. Figure 3.5a shows a graph of $\ln\left((H + H_o)\frac{dH}{dt}\right)$ versus $\frac{1}{k_B T}$ for the temperature range where Zr and B interdiffuse (580 – 890 K), for different heating rates. Evidently all curves are very nearly linear. This indicates that the kinetics of the first step in the reaction is consistent with a diffusion-controlled model, in agreement with the TEM observations. The diffusion activation energy can be determined from the slopes of the curves in Figure 3.5a and is estimated to be 0.47 ± 0.06 eV. Equation (3.1) can then be used to calculate the heat flow rate during the calorimetry scans. Figure 3.5b compares the model curves with the experimental data. The model curves agree well with the experimental data, but cannot explain why the gradual decline of heat flow rate is observed instead of an abrupt decrease when the diffusion process is completed. We attribute this to the homogenization of through-thickness composition gradients in the amorphous phase and to experimental factors such

as non-uniformity in the multilayer wavelength and temperature distribution in the sample.

The activation energy for the crystallization process can be determined from a Kissinger plot [78] of the heating rate versus peak temperature. The results are shown in Figure 3.5c for samples with both bilayer periods. The results for the multilayers with the 8.3 nm bilayer period show a significant amount of scatter because the overlap of both peaks in the calorimetry traces makes it difficult to determine an accurate value of the peak temperature. The results for the multilayers with the 4.1 nm period are better and provide an estimate of the activation energy of 2.4 eV. Although it is not possible to get an accurate value of the activation energy from the data points for the 8.3 nm samples, the results are certainly consistent with an activation energy of 2.4 eV.

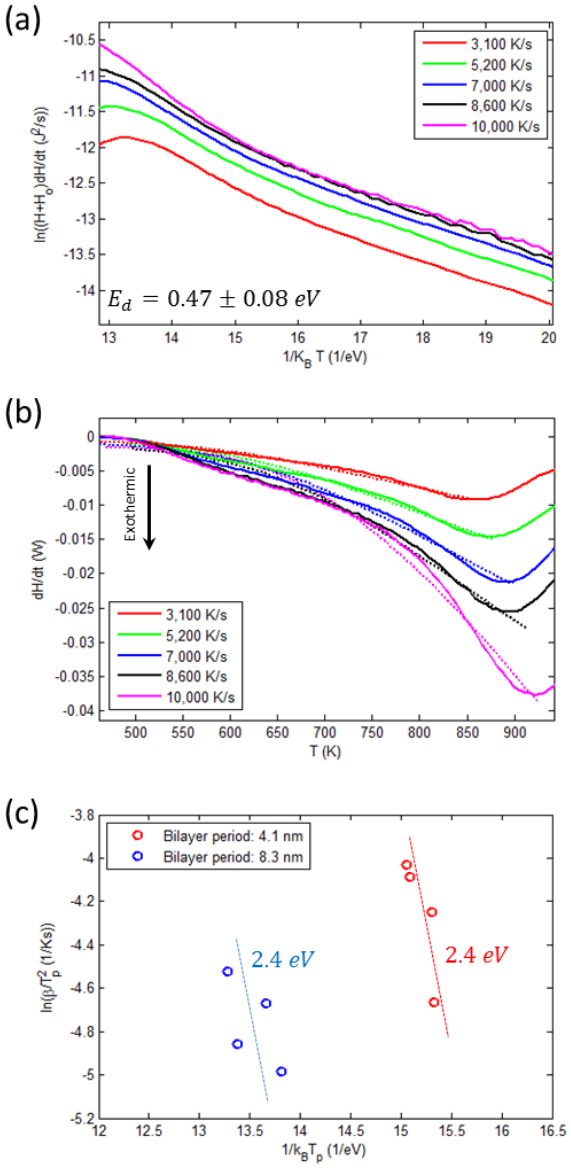


Figure 3.5. Kinetic analysis on the reaction in Zr/B multilayer: (a) $\mathbf{ln}\left((\boldsymbol{H}+\boldsymbol{H_o})\frac{\boldsymbol{dH}}{\boldsymbol{dt}}\right)$ versus $\frac{\mathbf{1}}{\boldsymbol{k_BT}}$ for the temperature range of 580 ~ 890 K. Slopes in this plot is the activation energy of the diffusion process. (b) Heat flow rate as a function of temperature: model curves (dotted lines) with experimental curves (solid lines). Plots in (a-b) were generated from the nanocalorimetry measurements performed on the samples with a bilayer period of 8.3 nm. (c) Kissinger plots for crystallization peaks from the measurements on both 4.1 and 8.3 nm period samples

It is instructive to compare the measured activation energies to values reported in the literature. For instance, Samsonov et al reported an activation energy of 1.69 - 1.99 eV [79] for the diffusion of B in Zr, a value that is much higher than the diffusion activation energy found in this study. The activation energy obtained by Samsonov et al was determined by measuring the thickness of ZrB_2 in Zr/B diffusion couples exposed to temperatures in excess of 1,373 K. No amorphous Zr/B phase was observed in their experiments. Formation of ZrB_2 thus required B to diffuse through crystalline ZrB_2, a process that is evidently much more difficult than diffusion through an amorphous phase, given the high activation energy. In fact, the activation energy measured by Samsonov et al is close to the activation energy for crystallization measured in this study. The crystallization activation energy is also close to the 2.57 eV activation energy reported for sintering of ZrB_2 [30]. To the best of our knowledge, formation of an amorphous Zr/B alloy through interdiffusion of B and Zr, and the very low associated activation energy have not been reported before. The phenomenon is similar, however, to the formation of amorphous phases during isothermal anneals in multilayers that contain components with a large negative Gibbs free energy of mixing and a large mismatch in atomic volume such as Au/La, Ti/Ni, and Ni/Zr [23, 80]. In these systems, diffusion through the amorphous reaction product is rate controlling, although the activation energies tend to be larger than the value reported here. We attribute this to the fact that the mismatch in atomic volumes in these systems is significantly larger than in the Zr/B system.

It is possible to synthesize ZrB_2 directly from Zr and B powders using a self-propagating reaction. Even though this process is cost-effective, it has been regarded as a less-than-ideal technique to produce bulk ZrB_2 [51]. The rapid heating rate (3,000 -

4,000K/s [51, 81]) associated with the process results in incomplete reaction of Zr and B, and in the formation of non-equilibrium phases [51]. Similar observations were made in our previous work on reactive multilayer where impurities in Zr prevented complete reaction of B and Zr [17]. Here we obtained high-purity multilayer samples by optimizing deposition process and demonstrate that complete reaction is possible as long as the impurity level is sufficiently low, and that this reaction occurs at relatively low temperatures compared with bulk processes for ZrB_2. Thus, it may be possible to manufacture low-cost bulk ZrB_2 using Self-propagating High-temperature Synthesis (SHS), although attaining the requisite purity levels may be difficult using powders because of the native oxide on Zr and the affinity of Zr for hydrogen and other impurities. It may also be possible to use Zr/B reactive multilayers to braze ultra high-temperature materials. The Zr/B reaction is highly exothermic and a nano-structured Zr/B multilayer could be used as a local heat source to melt the brazing material. In a similar application, Ni/Al reactive multilayers have been utilized to braze silicon, bulk metallic glasses, and other alloys [44].

3.4 SUMMARY

In conclusion, we have investigated the reaction kinetics of Zr/B multilayers using high-temperature nanocalorimetry combined with TEM. The multilayer reaction produces strongly textured ZrB_2 coatings below 1,300 K at heating rates ranging from 3,000 K/s to 10,000K/s. The Zr/B reaction proceeds in two stages: (1) interdiffusion between the nanocrystalline Zr and the amorphous B layers and the formation of an amorphous Zr/B alloy, and (2) crystallization of the amorphous alloy to form crystalline

ZrB_2. The formation of the amorphous alloy is diffusion limited and has a low activation energy of 0.47 eV. The crystallization step, in contrast, has a much higher activation energy of 2.4 eV. We believe that the kinetic information obtained in this study will provide useful insights into the synthesis of ZrB_2 using both conventional processing techniques and Zr/B reactive multilayers.

Chapter 4. Thermodynamics and kinetics solid-state alloying of Zr-B with different concentrations*

*Reprinted with permission from D. Lee, J. J. Vlassak, and K. Zhao, Nano Letters 15 (10), 6553-6558 (2015). Copyright 2015, American Chemical Society

4.1 INTRODUCTION

ZrB_2 exhibits a unique combination of properties including extremely high melting temperature, corrosion resistance, and mechanical hardness that make it an ideal structural material for extreme environments [8, 13, 14]. ZrB_2 is also a promising candidate in optoelectronic and microelectronic applications due to its excellent electrical and thermal conductivities, metal-like optical properties, and the similarity of in-plane lattice constants and thermal expansion coefficients between ZrB_2 and GaN [7, 9-12]. Large scale processing of dense structures of ZrB_2 is, however, challenging that makes implementation in practical systems difficult.

ZrB_2 is generally synthesized via reduction processes [8], chemical routes [11, 15, 16], or reactive processes [4, 17]. Solid-state alloying of Zr-B is the intrinsic process underlying nearly all the fabrication routes. However, a fundamental understanding of the thermodynamics and kinetics in the intermediate compounds of zirconium boride are

critically missing. Experimental measurements of the activation energy for Zr-B diffusion show a large variation of 0.47 ~ 1.99 eV [4, 18]. A few related theoretical studies are available including research on point defects and self-diffusion of Zr [82-84], structures and physical properties of ZrB_2 [28, 85-87], and phase stability of Zr-B compounds [88, 89].

To reach a comprehensive understanding of the solid-state alloying process of Zr-B, we investigate the energetics, diffusion kinetics, as well as the structural evolution with systematic variation of the B concentration in the Zr host. First-principles computational methods within the framework of density functional theory (DFT) are employed. We identify the diffusion pathways in the interpenetrating network of interstitial sites for a single B atom and demonstrate the anisotropic nature of B transport in Zr. The dominant hopping step is the hop from the octahedral to the crowdion site, which is distinct from the conventional mechanism of octahedral-tetrahedral transition in hexagonal close-packed (HCP) structures. In the intermediate compounds ZrB_x, $0<x\leq2$, the B diffusivity varies by a few orders of magnitude depending on the B concentration and the temperature of interest. It reaches a minimum for ZrB that originates from the lowest energy landscape at the rational stoichiometry of ZrB and from the drastic structural transition beyond this composition. We further perform nanocalorimetry measurements on Zr/B reactive multilayers to extract the kinetic parameters of the solid-state reaction. The diffusion barrier of ZrB_2 in atomistic modeling is in good agreement with the experimental values.

4.2 RESULTS AND DISCUSSION

4.2.1 Energetics of B insertion into the crystalline Zr host

We determine the stable positions of a single B atom in α-Zr, which has a HCP structure with a space group of $P6_3/mmc$ and lattice parameters $a = b = 3.23$ Å, and $c = 5.17$ Å [82, 84]. A single B atom is placed into a supercell at nonequivalent sites, shown in Figure 4.1a, including the octahedral site (Oct), the crowdion site (C), the basal bond center (Bc), the hexagonal site (Hex), the plane center (Pc), the tetrahedral site (Tet), and the substitutional site. We calculate the formation energy to compare the thermodynamic stability of B at the various sites. We take the energies of a Zr atom (E_{Zr}) and a B atom (E_B) in bulk form as reference energies, with $E_{nB\text{-}Zr}$ being the total energy of the system containing n B atoms in a cell that contains $(54 - m)$ Zr atoms (m=0, except when B is on the substitutional site, in which case $m = 1$). The formation energy per B atom $E_{fB}(n)$ is:

$$E_{fB}(n) = [E_{nB\text{-}Zr} - (54-m)\, E_{Zr} - nE_B]/n \tag{4.1}$$

Table 4.1 lists calculated formation energies at various sites and associated structural parameters, where ε_V is the volumetric strain and CN represents the coordination number, which is calculated by a cut-off of 10% elongation of the Zr-B bond in crystalline ZrB_2 (P6/mmm, $a, b = 3.17$ Å, $c = 3.53$ Å) [8]. The formation energies at the different positions indicate that B insertion at the Oct site results in the only energetically favorable structure. The C, Bc, Hex, and Pc sites are defined as metastable positions because the B atom would be stabilized at the initial insertion site upon relaxation, but the formation energies show positive values. Interestingly, the Tet site is unstable in that a B atom placed at this site will slide to the nearby hexahedral site during relaxation. The Tet

site has also been found unstable for O, N, and C impurities in HCP Ti [90, 91]. As a reference, we also calculate the formation energy for substitutional B in Zr. The large formation energy indicates that substitution of Zr by B is energetically costly and may occur only at high temperatures. We note that B insertion at interstitial sites with lower formation energies results in relatively small volumetric strains (ε_V) and large coordination numbers representing a less repulsive and more cooperative local environment. This correlation is plotted in Figure 4.1b, which shows a nearly monotonic increase of E_{fB} as a function of ε_V /CN. The static energy barrier (ΔE_s) for B transport can be estimated by subtracting E_{fB} for each interstitial site from that of the most stable site (Oct). This procedure suggests a preferred diffusion path, Oct-C-Oct with $\Delta E_s = 1.12$ eV, which occurs between the basal planes of the Zr lattice. The next favorable path is Oct-Bc-Oct with $\Delta E_s = 1.35$ eV, which corresponds to diffusion along the *c*-axis.

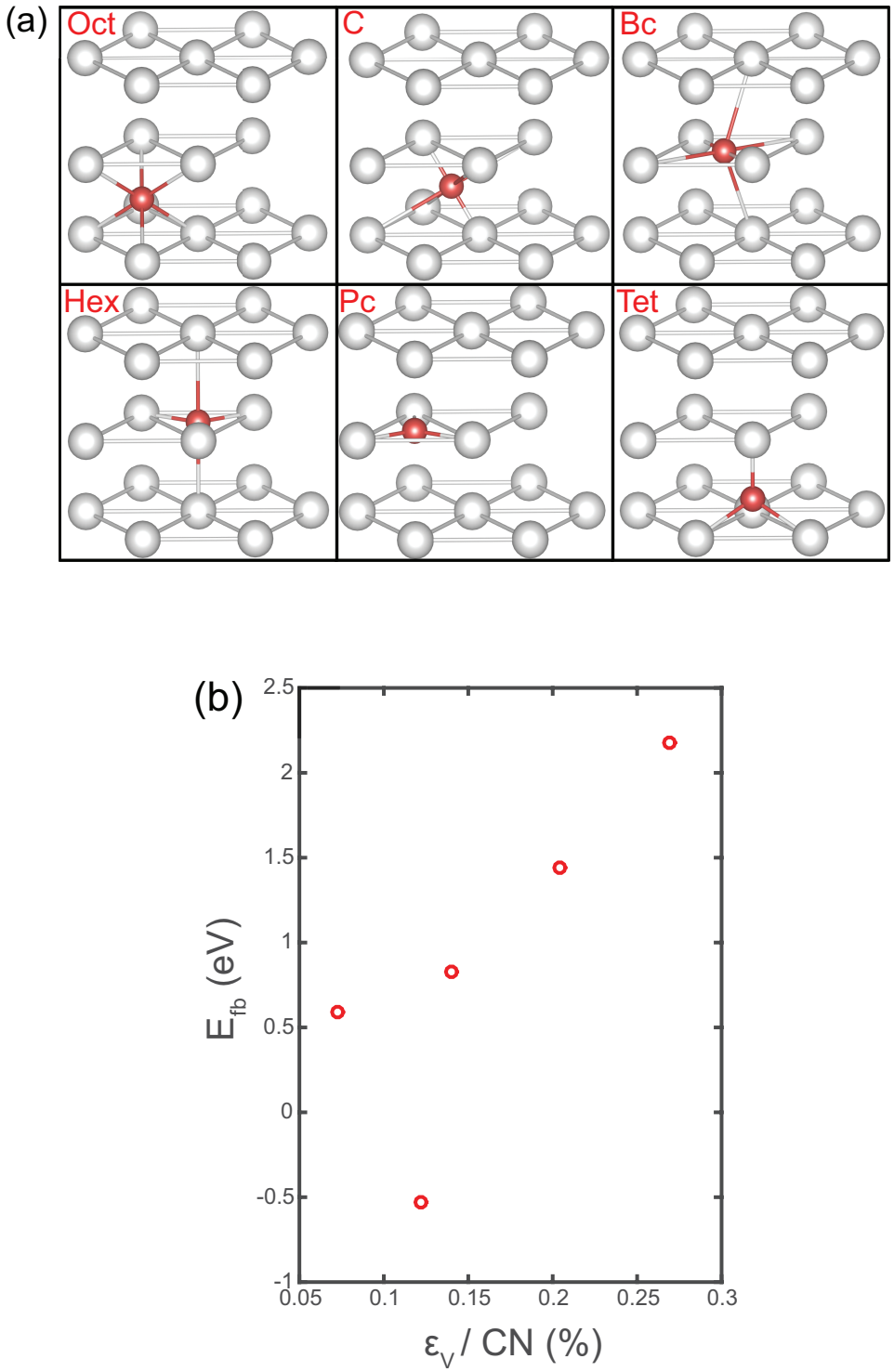


Figure 4.1. (a) Positions and local environments of the interstitial sites in Zr. (b) The formation energy of the interstitial B at each site versus volumetric strain / coordination number.

Table 4.1. Structural and energetic features of a single B atom at various sites in the Zr lattice

Boron sites	Position	E_{fB} (eV)	CN	ε_V (%)	Stability
Octahedral (Oct)	(0.33, 0.67, 0.25)	-0.53	6	0.732	Stable
Crowdion (C)	(0.83, 0.17, 0.25)	0.59	6	0.435	Metastable
Basal bond center (Bc)	(0.67, 0.83, 0.50)	0.82	6	0.840	Metastable
Hexahedral (Hex)	(0.00, 0.00, 0.50)	1.45	5	1.021	Metastable
Plane Center (Pc)	(0.33, 0.67, 0.50)	2.18	3	0.807	Metastable
Tetrahedral (Tet)	(0.67, 0.33, 017)	2.03	4	1.134	Unstable
Substitutional (Sub)	(0, 0, 0)	1.86	12	-1.605	Metastable

4.2.2 Interstitial diffusion of B in Zr

In order to determine the diffusion pathway of B, we calculate the activation energies along various diffusion trajectories using the nudged elastic band (NEB) method. In the NEB calculations, all atoms in the initial and final states are first relaxed in a supercell with fixed volume and shape. We then sample the diffusion pathway consisting of three intermediate configurations. The NEB path is constructed by linear interpolation of the atomic coordinates. Then, the path is relaxed until the force on each atom is smaller than 0.02 eV/ Å. The activation energy versus the reaction coordinate is illustrated in Figure 4.2 for several diffusion paths. Table 4.2 lists the calculated energy barrier (ΔE_{NEB}) and the energy corresponding to the occupancy probability of B at the initial position of the diffusion path (ΔE_i). When the initial position is Oct, ΔE_i is set to zero. The actual diffusion barrier ΔE_t is then $\Delta E_i + \Delta E_{NEB}$. Even though the NEB calculations show that the Bc-Hex and the C-Hex paths have relatively small energy barriers (0.46 and 0.73 eV, respectively), the actual activation energies of diffusion (ΔE_t),

are approximately 2.1 eV if the energy penalties for the initial sites are taken into account. Consistent with the earlier calculations of the static energy barrier (ΔE_s), the NEB simulations confirm that the Oct-C-Oct transition has the smallest diffusion energy barrier (1.39 eV). The Oct-Bc-Oct transition is the next preferred path with an energy barrier of 1.64 eV. Although the difference in the energy barrier between the two favorable paths is not large (0.25 eV), the corresponding Boltzmann factor, $\exp(-0.25/k_BT)$, where k_B is the Boltzmann constant and T is the temperature, indicates that diffusion along the second favorable path is approximately 18 times less likely than along the first path at 1,000 K, the temperature where the intermixing between B and Zr actively occurs [4]. Other transition paths do not contribute to the diffusion kinetics much as they have higher energy barriers. It is clear that B transport in crystalline Zr is highly anisotropic and that the hopping step from the octahedral to the crowdion site in the basal planes dominates the diffusion kinetics of B in Zr.

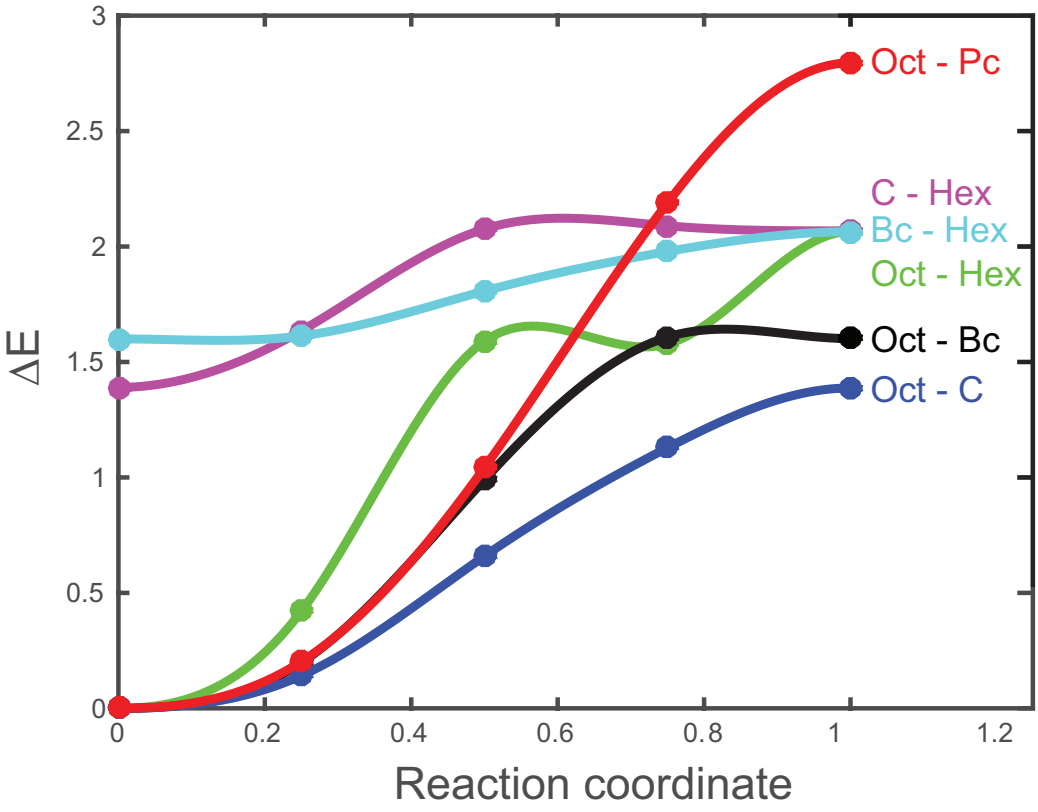


Figure 4.2. Activation energies of a single B atom along different diffusion trajectories calculated by the NEB method. The energy profile at the starting point takes into account the probability of B being filled at the initial position of the each path.

Table 4.2. Activation energies calculated by the NEB method for a single B atom along various diffusion trajectories.

Diffusion paths	ΔE_{NEB} (eV)	ΔE_i (eV)	ΔE_t (eV)
Oct-C	1.39	0	1.39
Oct-Bc	1.64	0	1.64
Oct-Hex	2.07	0	2.07
Oct - Pc	2.80	0	2.8
Bc-Hex	0.46	1.6	2.06
C-Hex	0.73	1.39	2.12

4.2.3 Energetics, structural features, and diffusion kinetics in the intermediate compounds ZrB_x, $0.25 \leq x \leq 2$.

We incrementally increase the B concentration in the Zr host. At each B concentration, we perform a Delaunay triangulation analysis to identify the largest void size in the lattice to accommodate insertion of B. Those void spaces are generally regarded as energetically favorable for B insertion [92]. In crystalline Zr, the centers of the largest voids correspond to the octahedral sites. B insertion drastically disorders the Zr lattice. We show in Figure 4.3a four representative structures, $ZrB_{0.5}$, ZrB, $ZrB_{1.5}$, and ZrB_2. More details of the structural evolution upon B insertion can be found in Figure C1. For each configuration, we calculate the enthalpy of formation from $E_f = [E_{mZr\text{-}nB} - mE_{Zr} - nE_B]/(m+n)$, where m and n represent the number of Zr and B atoms, respectively. The dependence of E_f on the composition is plotted in Figure 4.3b. Note that the Oct site, the only stable site with a negative value of the formation energy shown in Table 1, has an equivalent number of Zr host atoms. Therefore, the ZrB phase represents the case where

all Oct sites are filled by B. This structure has the lowest enthalpy of formation and is the most energetically favorable among the metastable compounds. We also include for comparison reference data points that correspond to experimentally found or theoretically predicted Zr-B crystalline phases [89, 93]. As expected, most of the crystalline phases have a smaller E_f compared to the metastable structures at the same concentration. One exception is that the ZrB phase in this study has a smaller E_f than the rock-salt phase reported in experiments. Figure 4.3c shows the evolution of the volumetric strain as a function of the B concentration. The slope of the volumetric strain remains very nearly constant throughout the entire range. We fit the dependence of the volumetric strain on the B concentration using a linear function, and obtain the partial molar volume of B in Zr, $\Omega_{B\text{-}Zr} = 0.51\times10^{-29}$ m^3. The large volumetric deformation during Zr-B alloying is accommodated by the amorphization of the Zr lattice and the gradual rearrangement of the structure through Zr-Zr bond breaking and Zr-B cluster formation. To examine the bonding mechanism, we measure the evolution of the atomic coordination at various concentrations. A physically meaningful measure of atomic coordination is needed to define the atomic bonds. We define Zr-Zr atoms to be bonded if their distance is within 10% of the Zr-Zr bond length in bulk crystalline ZrB_2, which corresponds to a largest bond distance of 3.50 Å. Likewise, we define that a Zr atom is bonded with a B atom if their distance is smaller than 2.81 Å, and that two B atoms are bonded to each other if their bond length is less than 2.02 Å. Figure 4.3d shows the average values of the coordination numbers. The Zr-Zr coordination steadily decreases indicating a constant breaking of the bonds between the host atoms. Interestingly, the rates of bond breaking and formation change discontinuously at the ZrB composition, indicative of the more

drastic structural change that occurs beyond this composition. More specifically, the CN for the B-Zr pairs stays nearly 6 for $ZrB_{x\leq1}$, which is the same as the CN for the Oct site (Table 1). When the B concentration increases, the CN starts to decrease indicating that metastable sites are now being filled. We find that most of the additional B atoms in $ZrB_{x>1}$ occupy Hex-like sites, which facilitates amorphization of the structure. This feature is also evident in the plot of the radial distribution function (RDF) for the Zr-Zr pairs– the structure remains largely crystalline up to the composition of ZrB (Figure 4.3e), but amorphization proceeds quickly beyond this point (Figure 4.3f).

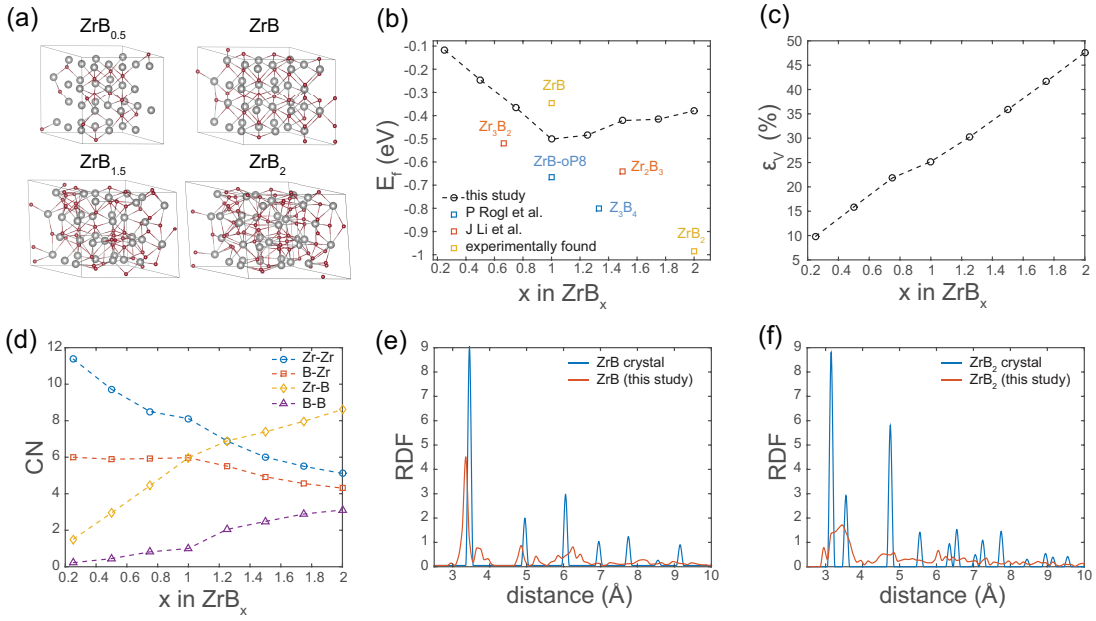


Figure 4.3. Structural and energetic features of $ZrB_{0.25\leq x\leq 2}$. (a) Representative geometries of the ZrB_x structures. (b) Enthalpy of formation of ZrB_x in this work (circles) and the values of crystalline references (squares). (c) Volumetric strain (d) Coordination numbers of Zr-Zr, B-Zr, Zr-B, and B-B pairs in the ZrB_x structures. (e, f) Radial distribution functions (RDF) of ZrB and ZrB_2 for the Zr-Zr pairs. RDFs of crystalline references are included for comparison (blue).

4.2.4 Diffusivity of B in various Zr-B compounds

We perform ab initio molecular dynamics (AIMD) simulations based on density functional theory using the eight relaxed structures with different B concentrations ($ZrB_{0.25\leq x\leq 2}$). Molecular dynamics calculations are carried out at temperatures of 1,500, 1,625, 1,750, 1,875, 2,000, and 2,500 K. The supercells are allowed to dynamically equilibrate at each temperature for 10,000 time steps; each step corresponding to 2 fs. We calculate the mean square displacements (MSD) of B using $\mathrm{MSD}=\left\langle \left| r_i(t) - r_i(0) \right|^2 \right\rangle$, where $r_i(t)$ is the position of atom i at time t, $r_i(0)$ is the position of atom i in the initial configuration, and <·> represents an average over the ensemble of atoms. The calculated mean square displacements of B in eight zirconium borides are shown in Figure C2 in Appendix C. Here we only consider the MSD of B because B is much more mobile in the mixing process compared to Zr. The diffusivity of B can be derived from the MSD using Einstein's relationship, $D = \lim_{t\to\infty} \frac{1}{6t} \left\langle \left| r_i(t) - r_i(0) \right|^2 \right\rangle$. We calculate the diffusivity of B at different temperatures and fit the data using the standard expression for diffusivity, $D = D_0 \exp(-E_a / k_B T)$, where E_a is the energy barrier. Logarithmic plots of the B diffusivity versus 1,000/T are shown in Figure C2 for eight representative compositions. Figure 4.4a shows the B diffusivity for each concentration at temperatures of 1,000, 1,500, and 2,000 K. For all temperatures, the diffusivity is minimum at ZrB. The B concentration effect is striking at the lowest temperature (1,000 K), with a difference of four orders of magnitude between the largest value for $ZrB_{0.25}$ and the smallest for ZrB. This is a consequence of the large activation energy for diffusion in the ZrB structure (Figure 4.4b) – B fills all Oct sites in the structure making B transport through the

structure very difficult. Effective transport of B would probably require a vacancy mechanism in this case.

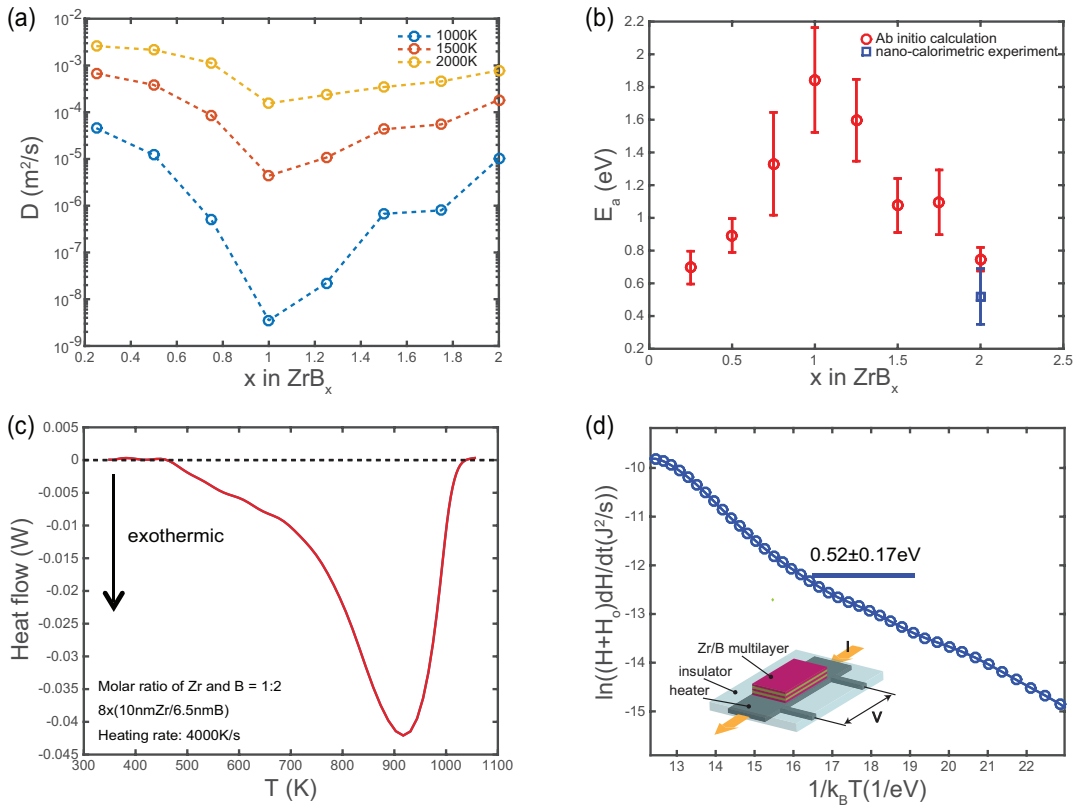


FIGURE 4.4. AIMD simulations and nanocalorimetry measurement to quantify the diffusion kinetics in ZrB_x. (a) B diffusivity vs. composition at different temperatures of 1,000, 1,500, and 2,000 K obtained from the MD simulations. (b) Red circles show the activation energies of B diffusion calculated from MD simulations. The error bars are calculated by linear fitting the MSD in different time ranges as detailed in Figure C2. Blue squares represent the experimental value by nanocalorimetry measurements. (c) Heat flow as a function of temperature obtained from a nanocalorimetry measurement on a Zr/B multilayer with a bilayer period of 16.5 nm. (d) A plot to obtain the activation energy of the diffusion in the Zr/B multilayer. The schematic of the nanocalorimetry sensor is depicted in the inset.

4.2.5 Comparison between first-principles and nanocalorimetry results

Nanocalorimetry experiments using a special sensor (Figure 4.4d inset) have been performed on a Zr/B reactive multilayer with a bilayer period of 16.5 nm and a specific atomic ratio of Zr:2B. The results are shown in Figures 4.4 c and d. The principle of the nanocalorimetry technique is reported in our previous work [1, 2, 17], and experimental details are included in the methodology section. Zr/B reactive multilayers are of technological interest as a means of synthesizing highly textured ZrB_2 coatings at relatively low temperatures [4]. As illustrated in Figure 4.4c, the exothermic reaction starts at 470 K and is completed at 1050 K, peaking around 910 K. The exothermic reaction in this temperature range is caused by the interdiffusion of B and Zr, yielding an amorphous Zr-B alloy [4]. The peak temperature observed here is higher than previous nanocalorimetry measurements [4] on Zr/B multilayers with smaller bilayer periods because of the increased diffusion distance in these multilayers.

With the formation of amorphous structures observed in both the Zr/B multilayer sample and in the AIMD simulations, it is possible to directly compare the results to cross validate experiments and simulations. Figure 4.4d shows a graph of $\ln[(H+H_o)dH/dt]$ versus $1/k_BT$ for the temperature range of 500 ~ 930K, where H is the enthalpy released during the exothermic reaction and H_o is the enthalpy that corresponds to the mixed Zr/B interface layers (1.5 nm, approximately [4]) formed during the multilayer deposition process. The slope of this curve has been shown to be the diffusion activation energy for a number of multilayer systems [4, 24, 62]. The graph is nearly linear with a slope of 0.52

eV, a value that is marked in Figure 4.4 b and that agrees well with the AIMD simulations for the same concentration.

4.3 METHODS

The first-principles calculations based on the DFT are carried out using the Vienna ab initio simulation package (VASP) [94]. The projected-augmented-waves (PAW) [95] with the Perdew-Burke-Ernzerhof (PBE) [96] exchange-correlation potentials are adopted. For Zr, $4s^2 4p^6 5s^2 4d^2$ valence states are treated. The cut-off energy for plane waves is set to 400 eV, and the forces are converged to within 0.02 eV/Å. We use a 54-atom Zr supercell (3×3×3) and one B atom for the simulations to identify the interstitial sites and for the NEB [97, 98] calculations. For the relaxations of the eight structures with different B concentrations ($ZrB_{0.25\leq x\leq 2}$) and for the AIMD simulations, supercells with 36 Zr atoms (3×3×2) and the number of B atoms corresponding to each concentration are utilized. For Brillouin zone sampling, 6 × 6 × 4, 3 × 3 × 2, 3 × 3 × 3, and 1 × 1 × 1 *k*-point meshes in the Monkhorst−Pack scheme are employed for the simulations of the interstitial sites, the NEB calculations, the relaxations of the $ZrB_{0.25\leq x\leq 2}$ structures, and the AIMD simulations, respectively.

Nanocalorimetry sensors are fabricated using conventional Si-based micro-fabrication techniques. Details of sensor fabrication and working principle can be found elsewhere [1, 2, 4]. A multilayer with alternating Zr and B layers (molar ratio = 1:2, bilayer period = 16.5 nm, total thickness = 82.5 nm) is magnetron sputter deposited using 99.99% Zr and 99.95% B targets inside a chamber with a base pressure better than 2×10^{-7} Torr. A scanning nanocalorimetry measurement is performed in vacuum at a heating rate

of 4,000 K/s, during which both the power supplied to and the temperature of the calorimetry sensor are measured. The raw power and temperature data is utilized to determine the reactive heat flow of the multilayer sample following the procedure developed in our previous work [17].

4.4 SUMMARY

In conclusion, we have studied the thermodynamics and kinetics of the solid-state alloying process of Zr-B for the synthesis of ZrB_2. In the limit of low B concentration, B transport in crystalline Zr is highly anisotropic and is dominated by the Oct-C transition between the Zr basal planes. With increasing B concentration, the Zr structure is gradually amorphized as a result of the rupture of host atom bonds and the formation of Zr-B clusters. The ZrB phase maintains the lowest enthalpy of formation among all the metastable compounds. The ZrB energy landscape has the highest energy barrier for B transport, yielding the lowest B diffusivity, consistent with the results obtained in the molecular dynamic simulations. Nanocalorimetry measurements on Zr/B reactive multilayers allow experimental determination of the diffusion energy barrier, and are in good agreement with the atomistic simulations for ZrB_2. The fundamental understanding of the Zr and B interdiffusion process arising from the combination of atomistic modeling and experimentation provides valuable insight that can be used to optimize the fabrication of ZrB_2 coatings for a range of practical applications.

Chapter 5. Kinetic role of carbon in solid-state synthesis of ZrB_2 using MRNLs*

*Reprinted with permission from D. Lee, G.D. Sim, K. Zhao, and J. J. Vlassak, Nano Letters 15 (12), 8266-8270 (2015). Copyright 2015, American Chemical Society

5.1 INTRODUCTION

Zirconium diboride (ZrB_2), a high-performance ceramic with metallic properties, exhibits a unique combination of physical, chemical, and structural properties, making it a material of interest for a broad range of applications. Examples include its use as a substrate for group III nitride semiconductors in optoelectronic devices [7, 9-12], as support material for low-temperature fuel cells [99, 100], and as a hydrogen storage medium [101]. Difficulties associated with synthesis, however, have hindered broad adoption of the material – production of high-density ZrB_2 typically requires both extremely high temperature and pressure [102] because of its high melting point and stability. Viable synthesis methods of ZrB_2 have been a topic of intense investigation for decades [7, 8, 102]. Additives such as carbon have been shown to improve the processability of ZrB_2. It has been reported that carbon promotes removal of surface oxides in ZrB_2 powders and limits grain growth, thus enhancing its sinterability [103-106]. The beneficial role of carbon in the formation of ZrB_2-based compounds, however,

is not fully understood and few studies have been conducted at the nano- to atomistic scales [105].

Recent experiments [4] have demonstrated low-temperature synthesis of highly textured crystalline ZrB_2 coatings through use of multilayered reactive nanolaminates (MRNLs) that consist of alternating layers of Zr and B. The synthesis is facilitated by the formation of an intermediate amorphous phase that allows fast transport of B [4, 5]. The notion that the addition of carbon may further facilitate synthesis of ZrB_2 motivated us to investigate the phase evolution in reactive nanolaminates that contain Zr, B, and C. In this chapter, we combine nanocalorimetry and ab-initio simulations to study the energetics and kinetics of phase evolution in Zr/B_4C MRNLs.

We demonstrate that, as temperature increases, the crystalline Zr and amorphous B_4C layers of the MRNLs intermix to form an amorphous compound. In a subsequent step, this amorphous compound crystallizes to form a textured ZrB_2 coating that is supersaturated with carbon. A kinetics analysis of the nanocalorimetry results reveals that the activation energies of both diffusion and crystallization are reduced by more than 20% compared to the reaction in MRNLs without carbon. Ab-initio calculations on α-Zr with a C atom at various interstitial sites reveal that Zr and C bond more strongly than Zr and B, thus facilitating interdiffusion of B. The finding suggests that C doping may be an effective strategy to facilitate ZrB_2 synthesis.

5.2 RESULTS AND DISCUSSION

5.2.1 Nanocalorimetry and structural characterizations of Zr/B_4C MRNLs

The micromachined nanocalorimetry sensors used in this study have been described in detail elsewhere in the literature [1, 2, 17]; a brief description of the sensors and experimental details are provided in the methods section (Chapter 5.3). MRNLs consisting of alternating Zr and B_4C layers were sputter deposited directly onto the nanocalorimetry sensors as illustrated schematically in the inset of Figure 5.1a. The thickness of each layer was determined to ensure a stoichiometric composition: as-deposited samples had a 3:1 molar ratio of $Zr:B_4C$, to produce a 2:1 molar ratio of ZrB_2:ZrC after reaction. Figure 5.1 shows, as a function of temperature, the heat produced by Zr/B_4C nanolaminates with bilayer periods of (a) 5 nm and (b) 10 nm. In order to characterize the kinetics of the reaction, scanning rates were varied from 4,800 K/s to 56,600 K/s as indicated in the figures.

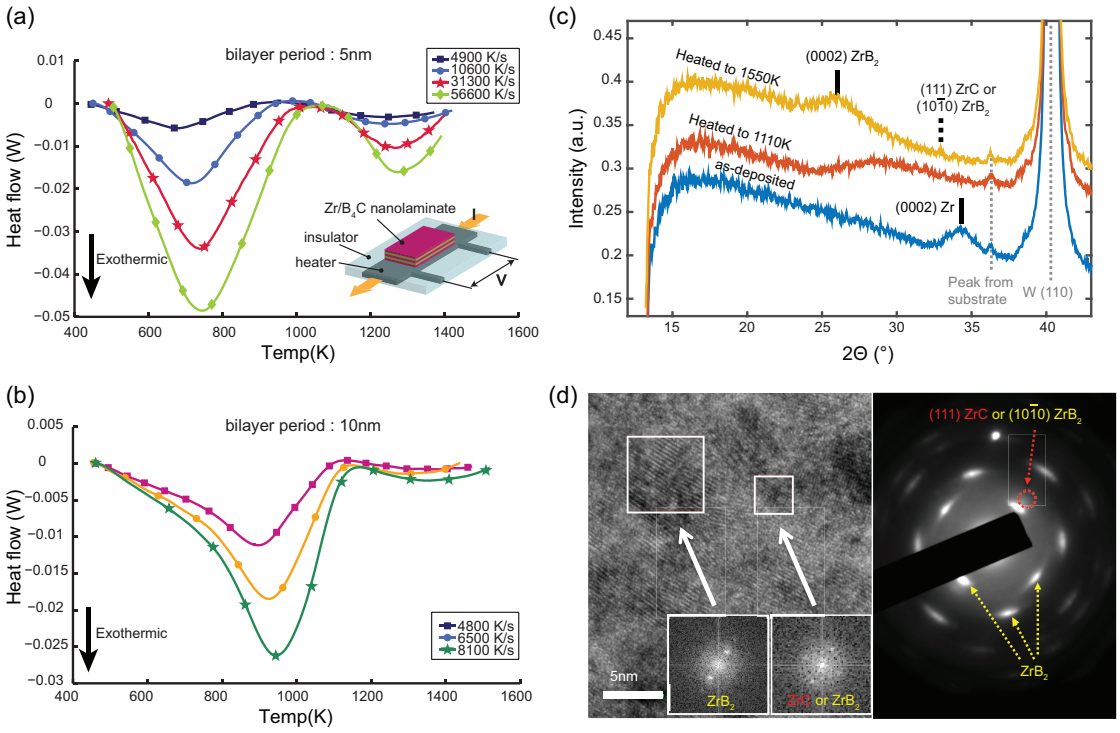


FIGURE 5.1. Heat flow vs. temperature for Zr/B_4C nanolaminates with bilayer periods of (a) 5 nm and (b) 10 nm measured using nanocalorimetry. Nanocalorimetry heating rates are indicated in the insets of the figures (c) XRD results for an as-deposited nanolaminate (bilayer period: 10nm), and for nanolaminates heated to 1,110 and 1,550 K (scanning rate: 8,100 K/s). (d) Cross-sectional TEM micrographs for a nanolaminate heated to 1,550K: (left) bright-field image with Fourier transform analyses for selected regions and (right) diffraction pattern.

The heat flow curves in Figure 5.1a, b clearly show that the reaction in the Zr/B_4C MRNLs proceeds in two distinct stages, each represented by an exothermic peak. The stage that corresponds to the first exotherm starts around 400-500 K for all samples tested. This stage of the reaction is complete at temperatures below 1,000 K for the samples with a 5 nm bilayer period, and below 1,150 K for the samples with a 10 nm period. Faster heating rates and larger bilayer periods result in higher peak temperatures. The second stage is completed at approximately 1,400 K for the samples with a 5 nm bilayer period, and at 1,550 K for the 10 nm samples. Again, faster heating rates and larger bilayer periods shift the peak temperatures to higher values, but the effect is less pronounced than for the first stage.

To determine the phase evolution of the MRNLs during the two stages of the reaction, X-ray diffraction (XRD) was performed on MRNLs with a 10 nm bilayer period in the as-deposited state, heated to an intermediate temperature (1,110 K) and quenched, and after completion of the second exothermic reaction (1,550 K). As shown in Figure 5.1c, the as-deposited sample has a diffraction peak corresponding to crystalline Zr with a (0002) texture (Powder Diffraction File #050665). No other reflections are identified, indicating that the as-deposited MRNL consists of crystalline Zr and amorphous B_4C. The intermediate sample has a broad peak corresponding to an amorphous structure. This result implies that the first exothermic peak in the calorimetric signal is caused by the intermixing and amorphization of the Zr and B_4C layers in the laminate, explaining the shift to higher temperatures of the first calorimetry peak as the bilayer period, and thus the diffusion distance, increases. The sample heated to 1,550 K has a strong diffraction peak corresponding to the (0002) ZrB_2 reflection (Powder Diffraction File #050665), and

a very small peak caused by the $(10\bar{1}0)$ ZrB_2 or the (111) ZrC (Powder Diffraction File #050665) reflections – evidently, the second stage in the reaction corresponds to the crystallization of the amorphous phase to form a supersaturated, crystalline ZrB_2 phase, with possibly a small amount of ZrC. Transmission electron microcopy (TEM) performed on the same sample confirms the XRD findings as shown in Figure 5.1d. The electron diffraction pattern shows distinct spots rather than rings, indicating that the ZrB_2 films have a preferred crystallographic texture. This texture, together with the small crystallite size, suggests that the crystalline phase nucleates preferentially at the original interfaces of the MRNLs or that remanent concentration gradients at these interfaces induce a preferred nucleus orientation. These arguments are further supported by the observation that the peak crystallization temperature decreases with decreasing bilayer period, i.e., with increasing density of original interfaces.

The total reaction enthalpy is calculated by integrating the heat flow curves in Figure 5.1a, b. The reaction enthalpy is independent of the heating rate, but varies with the bilayer period of the MRNLs because of a small amount of intermixing that occurs during sputter-deposition of the nanolaminates: samples with a 5 nm period released 392 ± 72 μJ, while 10 nm period samples produced 784 ± 117 μJ, respectively 19.7 ± 3.6 and 39.5 ± 5.9 % of the theoretical enthalpy for the reaction of $3Zr + B_4C \rightarrow 2ZrB_2 + ZrC$ [107]. The energies associated with the first stage of the reaction are 295 ± 55 and 727 ± 93 μJ, respectively. Given that the total thickness of the two sets of laminates is the same and that the volume of initially intermixed material is two times larger for the samples with the 5 nm period than for the samples with the 10 nm period, the thickness of the intermixed layer can be estimated from the experimental reaction enthalpies as

approximately 1.9 nm per bilayer period.

5.2.2 Kinetics of reactions in Zr/B_4C MRNLs

The sequence of interdiffusion and crystallization in the Zr/B_4C MRNLs is similar to the sequence observed in MRNLs that consist of alternating Zr and amorphous B [4] layers. Thus we adopt the diffusion model developed for the Zr/B system to characterize the first exothermic reaction in the Zr/B_4C MRNLs [4]. According to this model, there exists a simple relationship between the rate at which enthalpy is produced during the reaction and the rate of interdiffusion: $(H + H_o)\mathrm{d}H/\mathrm{d}t$ at a given temperature is proportional to the diffusivity at that temperature. Here, H is the enthalpy released during the exothermic reaction and H_o is the enthalpy that corresponds to the initially mixed Zr/B_4C interface layers. Figure 5.2a shows graphs of $\ln\big((H + H_o)\mathrm{d}H/\mathrm{d}t\big)$ versus $1/k_BT$ over the temperature range of the first exotherm for several samples. The graphs are nearly linear and have a slope of 0.37 ± 0.08 eV, regardless of bilayer period or heating rate. This slope is the activation energy for the interdiffusion process [4, 24, 62].

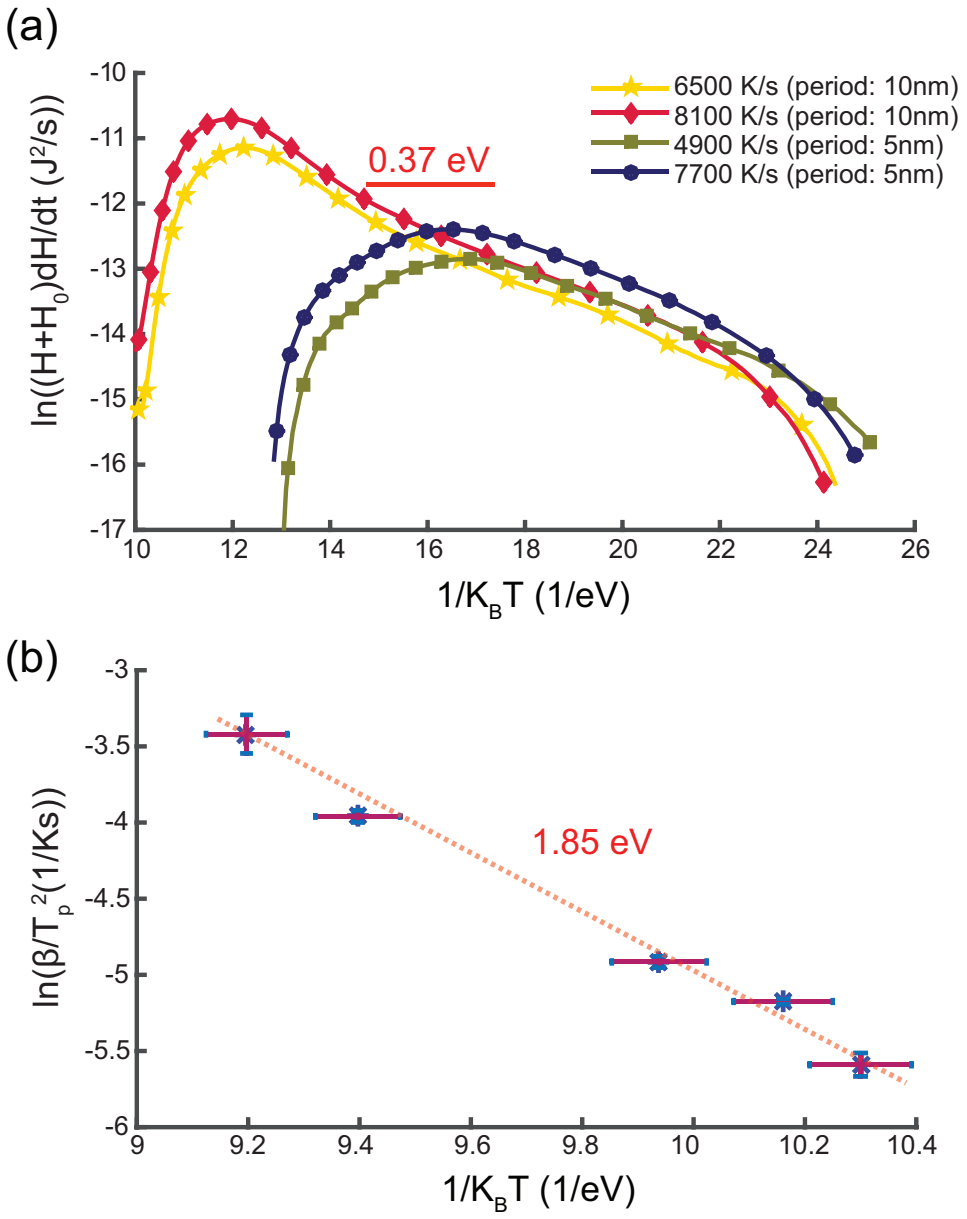


FIGURE 5.2. Kinetic analyses of the reactions in Zr/B_4C MRNLs: (a) $\mathbf{ln}\left((\boldsymbol{H}+\boldsymbol{H_o})\mathbf{d}\boldsymbol{H}/\mathbf{d}\boldsymbol{t}\right)$ versus $\mathbf{1}/\boldsymbol{k_BT}$ over the temperature range of interdiffusion between Zr and B_4C. (b) Kissinger analysis of the crystallization peaks of the nanolaminates with a 5 nm bi-layer period.

The kinetics of the crystallization step can be characterized using a Kissinger analysis [78] of the crystallization peak temperature, yielding an activation energy of 1.85 eV (Figure 5.2b). This value is much larger than the activation energy for interdiffusion, which is consistent with the observation that the crystallization peak temperature is less sensitive to the heating rate than the interdiffusion peak (Figure 5.1). The activation energies for diffusion and crystallization obtained for the Zr/B_4C MRNLs are approximately 20% smaller than the values for the Zr/B MRNLs [4]. Since the nanolaminates were synthesized in high vacuum without any exposure to air, our results suggest that carbon enhances the formation of ZrB_2, not by the removal of surface/interfacial oxides as observed in the sintering of ZrB_2 powders [103-106], but by lowering the energy barriers associated with the formation reactions.

The formation of amorphous phases in both Zr/B_4C and Zr/B [4] nanolaminates upon intermixing can be explained by the large differences in the atomic sizes of the constituent atoms (atomic radius of Zr, B, and C are 1.62 Å, 0.90 Å, and 0.77 Å, respectively [108]), the low solubility of B and C in Zr, and the steep concentration gradients at the interfaces of the MRNLs, which suppress nucleation of the crystalline phase [23, 25-27, 109]. However, the lower activation energies for interdiffusion and crystallization in the Zr/B_4C system compared to the Zr/B system are somewhat surprising because the addition of more elements to a compound typically enhances its glass forming ability and lowers the diffusivity of its constituent atoms [109-112].

5.2.2 First-principles calculations of Zr-C

In order to gain a better understanding of the mechanism responsible for lowering the activation energies for interdiffusion and crystallization, we have performed first-principles calculations on α-Zr ($P6_3/mmc$, $a = b = 3.23$ Å, and $c = 5.17$ Å [82, 84]) containing C atoms at various interstitial sites. We only consider stable or metastable sites where the C atom is stabilized at the initial interstitial position upon energetic relaxation [5]. These sites include the octahedral site (Oct), the crowdion site (Cd), the basal bond center site (Bc), the hexagonal site (Hex), and the plane center (Pc) site. Positions and local environments of the sites are depicted in Figure 5.3. We also consider the substitutional site (Sub) as a reference. To determine the thermodynamic stability, the formation energy per C atom can be calculated for each interstitial site using the following expression,

$$E_{f\mathrm{C}}(n) = [E_{n\mathrm{C\text{-}Zr}} - (54-m)\,E_{\mathrm{Zr}} - nE_{\mathrm{C}}]/n. \quad (5.1)$$

We take the energies of a Zr atom (E_{Zr}) and a C atom (E_{C}) in bulk form as reference energies, with $E_{n\mathrm{C\text{-}Zr}}$ the total energy of a system containing n C atoms in a super-cell that contains $(54 - m)$ Zr atoms (m=0, except when C is at the Sub site, in which case $m = 1$).

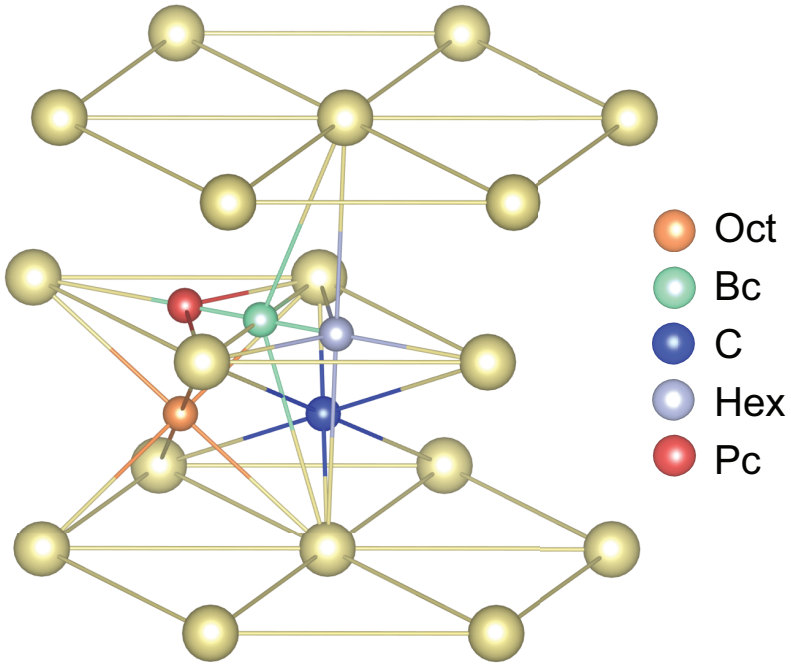


Figure 5.3. Positions and local environments of the interstitial sites in Zr

Table 5.1. Structural and energetic features of a single C or B atom at various sites in the Zr lattice

Interstitial sites	Position	CN	E_{fC} (eV)	E_{fB} (eV) [5]
Octahedral (Oct)	(0.33, 0.67, 0.25)	6	-1.53	-0.53
Crowdion (Cd)	(0.83, 0.17, 0.25)	6	0.029 (1.56)	0.59 (1.12)
Basal bond center (Bc)	(0.67, 0.83, 0.50)	6	-0.046 (1.48)	0.82 (1.35)
Hexahedral (Hex)	(0.00, 0.00, 0.50)	5	0.303 (1.83)	1.45 (1.98)
Plane Center (Pc)	(0.33, 0.67, 0.50)	3	2.16 (3.69)	2.18 (2.71)
Substitutional (Sub)	(0, 0, 0)	12	3.98	1.86

Table 5.1 lists calculated values for E_{fC} at various sites. CN represents the coordination number, which is calculated using a cut-off length of 110 % of the Zr-C bond length in crystalline ZrC (2.36 Å). We also list the formation energy per B atom (E_{fB}) at each interstitial site in Zr for comparison [5]. The most stable site for C in Zr is the Oct site, which is also the most stable site for B in Zr. The Sub site is energetically very costly for both C and B atoms, indicating that both B and C are transported in the Zr lattice via an interstitial rather than a substitutional mechanism.

The values in parentheses in the last two columns of Table 5.1 represent the static energy barrier (ΔE_s), a measure of the energy barrier for a given diffusion path [5, 91]. ΔE_s can be estimated by subtracting E_{fC} or E_{fB} for each interstitial site from that of the most stable site (Oct). Interestingly, the Oct-Bc-Oct transition yields the lowest value for C (ΔE_s = 1.48 eV), while B has a preferred diffusion path of Oct-Cd-Oct (ΔE_s = 1.12 eV). These results suggest that C diffuses faster along the c-axis, while B diffuses preferentially within the basal plane. Note that the barrier for diffusion in Zr is larger for C than for B, for most of the cases considered. Thus, the enhanced interdiffusion between

Zr and B in the presence of C is not caused by the intrinsic diffusion properties of C in Zr. Instead, we submit that it arises because the interaction between Zr and C is stronger than between Zr and B – indeed, as shown in Table 5.1, C has a lower energy in all interstitial sites of Zr than B. The stronger bonding between Zr and C enhances the amorphization of the Zr lattice in the course of intermixing and thus facilitates the transport of B through the resulting amorphous phase. The presence of C decreases the equilibrium concentration of B at the amorphous ZrB_xC_y/α-Zr phase boundary compared to Zr/B MRNLs. Previous ab-initio simulations [5] have shown that the diffusion activation energy decreases with decreasing B concentration in ZrB_x, $0 < X \leq 1$, in line with our observation here.

Carbon also reduces the activation energy for crystallization. We believe that this is not the result of enhanced mobility of the constituent atoms – on the contrary, we would expect the presence of C in a homogenous amorphous ZrB_2 alloy to reduce the mobility of all atoms [109-111]. Our experimental results show that the enthalpy of crystallization is larger for Zr/B_4C than for Zr/B MRNLs [4]. This observation suggests that the reduced activation energy for crystallization may be caused by a larger free energy difference between the amorphous phase and the crystalline product. According to classical nucleation theory [113], a larger free energy difference increases the thermodynamic driving force for crystallization and lowers the nucleation barrier, resulting in a reduced activation energy for the crystallization process.

5.4 METHODS

Each micromachined nanocalorimetry sensor consists of a 100 nm Ti-W alloy four-point electrical probe that serves both as a resistance thermometer and as a Joule heater. The element is encapsulated and is supported by a freestanding 300 nm Si_3N_4 membrane. The Si_3N_4 membrane serves to isolate sample and sensor from the ambient. Details of the operating principles and sensor fabrication procedures can be found elsewhere [1, 2].

Zr/B_4C nanolaminate samples were magnetron sputter deposited (ATC 1800, AJA Int.) on the measurement section of the nanocalorimetry sensors using 99.99% Zr (DC 80W, 5nm/min) and 99.95% B_4C (RF 150W, 0.4nm/min) targets (Kurt J. Lesker Company). The thickness of each layer was determined to ensure a stoichiometric composition: 3:1 molar ratio of Zr:B_4C in the as-deposited samples to produce a 2:1 molar ratio of ZrB_2:ZrC after the reaction. Nanolaminate samples with bilayer periods of 5 nm and 10 nm, and a total thickness of 80 nm were used in this work. The area of the sample was defined using a custom made Si-shadow mask during the sputter-deposition process.

All nanocalorimetry measurements were performed inside a high-vacuum furnace with a base pressure better than $5x10^{-6}$ Torr. The samples were heated to approximately 1550 K at heating rates from 4,800 K/s to 56,600 K/s. The power input and the temperature data were utilized to determine the reactive heat flow of the nanolaminate sample following the procedures established in our previous work [17].

X-ray diffraction (XRD) measurements were performed on both the as-deposited sample and on the samples heated to 1,110 and 1,550 K (D8 Discover, Bruker). TEM

images were acquired for the sample heated to 1,550 K using JEOL 2100 system. The TEM sample was prepared using a typical *in-situ* lift-out technique (INLO) [114] in an focused ion beam system (Zeiss NVision 40 Dual-Beam). The samples that were heated for XRD and TEM studies were quenched with a fast cooling rate (~ 15,000 K/s) to freeze in the structure before performing XRD or TEM.

Density functional theory calculations were performed using the Vienna ab initio simulation package (VASP) [94]. The projected-augmented-waves (PAW) [95] with the Perdew-Burke-Ernzerhof (PBE) [96] exchange-correlation potentials were adopted. For Zr, the valence states were treated using a Zr_sv ($4s^2 4p^6 5s^2 4d^2$) pseudo-potential. The C ($2s^2 2p^2$) pseudo-potential was employed for carbon. The cut-off energy for plane waves was set to 400 eV, and forces were converged to within 0.02 eV/Å. We used a 54-atom Zr super-cell (3×3×3) and one C atom for the simulations to identify the interstitial sites. A 6 × 6 × 4 *k*-point mesh in the Monkhorst−Pack scheme was employed for Brillouin zone sampling.

5.4 SUMMARY

In conclusion, we have studied the thermodynamics and kinetics of the interdiffusion and crystallization of Zr/B_4C MRNLs by combining nanocalorimetry and first-principles calculations. Nanocalorimetry and structural characterization reveal intermixing of the two constituent layers of the MRNLs upon heating, followed by crystallization to form a ZrB_2 phase that is super-saturated with C. A diffusion model for a multilayered system with crystalline and amorphous phase boundaries and a Kissinger analysis reveal that the Zr/B_4C MRNLs have lower energy barriers for both interdiffusion

and crystallization than Zr/B MRNLs. First-principles calculations suggest that the lower energy barrier for interdiffusion diffusion is not caused by the diffusional properties of C in the Zr lattice, but rather by the stronger interactions between Zr and C. The reaction thermodynamic and kinetics discussed in this work can provide guidance for optimizing the fabrication process of ZrB_2 coatings.

Chapter 6. Enhanced transport of B into Zr via local instability at the interface of MRNLs with impurities*

*Reprinted with permission from D. Lee, J. J. Vlassak, and K Zhao, ACS Applied Materials & Interfaces, DOI: 10.1021/acsami.6b01733 (2016). Copyright 2016, American Chemical Society

6.1 INTRODUCTION

Transition metal diborides are metallic ceramics with a unique combination of properties, including extremely high melting points, outstanding chemical stability, high thermal conductivity, low electrical resistivity, low work function, and extreme hardness. This combination of properties has led to their use in low-temperature fuel cells [99], in optoelectronics and microelectronics [7, 9-12], as hydrogen storage media [101], as super-hard materials [115, 116], and in superconducting nanodeviecs [117]. However, their high melting points, in addition to excellent chemical and mechanical stability, require extreme processing conditions that limit their adoption in many applications [7, 8, 116]. Multilayered reactive nanolaminates (MRNLs) that consist of alternating layers of a transition metal and boron provide a promising route to synthesize transition metal

borides at relatively low temperatures and without contamination [4, 17, 118]. The formation of metal diborides using MRNLs is typically a two-step process that starts with low-temperature intermixing and amorphization of the layers, and that concludes with the formation of crystalline diborides at a more elevated temperature. The low reaction temperature is possible thanks to the formation of an intermediate amorphous phase that allows facile transport of B atoms [4, 5].

Processing of transition metal diborides can be facilitated through use of additives. Carbon, for instance, is known as an effective sintering aid for diborides. Carbon promotes removal of surface oxides in ZrB_2 and limits grain growth, thus enhancing its sinterability. Recent experiments using nanocalorimetry also demonstrated that C has a profound impact on the formation of ZrB_2 in MRNLs. Kinetics analyses of the intermixing of Zr and B, and of the crystallization of amorphous ZrB_2 show that the activation energies for both processes are reduced by more than 20% when C is present in the MRNL [6]. Carbon has a larger electronegativity difference with Zr (1.22) than B (0.71) and binds with Zr much more strongly. The accelerating effect of C runs counter to classical glass theory, which suggests that larger negative heats of mixing generally result in slower kinetic processes [109-111]. The kinetic role of carbon may be attributed to its role in the structural transformation that occurs at the Zr/B interface and that results in the formation of the amorphous ZrB_2 compound – the strong bonding between Zr and C, in addition to the steep concentration gradients at the interface, enhances amorphization of the Zr lattice and thus facilitates the transport of B atoms. Since this process is associated with the Zr/B interface, we expect its effects to diminish as the thickness of the elemental

layers in the MRNLs increases and the overall process becomes more diffusion-controlled – eventually the process of nucleation and growth takes over.

Here we perform a fundamental study of how additives such as C or N facilitate the synthesis of crystalline ZrB_2 using MRNLs. The study is performed using first-principles computational methods within the framework of density functional theory (DFT). We start with a detailed examination of the energetics, bonding mechanism, and diffusion kinetics of B and C in bulk α-Zr. We show that interstitial C markedly decreases the mobility of B in the Zr lattice and frustrates the amorphization of crystalline Zr. We then investigate the effects of C and N on the intermixing of Zr/BC_x or Zr/BN_y MRNLs. We find that the addition of C or N significantly enhances the amorphization of the Zr lattice at the interfaces and promotes transport of B through the amorphous layer. Evidently the effects of C and N are quite distinct for the bulk phase or the interface, even though in both cases these effects originate from the strong atomic bonding of C and N with Zr. Based on these results, we propose that the addition of elements with strong binding energies to transition metals may be an effective method to facilitate the low-temperature synthesis of diborides. We compile a map of the heat of mixing of various transition metals with B, C, and N to guide the synthesis of diboride-based ceramics using MRNLs.

6.2 RESULTS AND DISCUSSION

6.2.1 Nature of the bond between Zr and B or C

We study the electronic structure of crystalline α-Zr (space group: $P6_3/mmc$, $a = b = 3.23$ Å, and $c = 5.17$ Å [82, 84].) with a B or C atom at an octahedral (Oct) interstitial site. The Oct site is energetically favorable for the insertion of both B and C [5, 6]. Figures 6.1a and 6.1b show the distributions of the total valence electron charge densities on a $(01\bar{1}1)$ plane of the Zr lattice with either an interstitial C or B atom. Figure 6.1c shows line profiles of the charge density distribution from the C or B atom to the nearest Zr atom. Close inspection of the graphs shows that atomic bonds of mixed covalent-ionic character are formed between the neighboring Zr atoms and the interstitial elements, and that C forms a stronger bond with Zr than B. This is consistent with a prior study that revealed that the formation energy of a C interstitial at the Oct site is -1.53 eV, while the formation energy for a B interstitial is -0.53 eV [5, 6]. Note that the stronger interaction makes the length of the bond between Zr and C (2.28 Å) shorter than between Zr and B (2.34 Å).

To further explore the bond character of Zr-C and Zr-B, we plot the charge density difference distributions on a $(01\bar{1}1)$ plane of the Zr lattice with either a C or B interstitial in Figures 6.1d and 1e. The corresponding line profiles from the C or B atom to a neighboring Zr atom are shown in Figure 6.1f. Here the charge density difference $\Delta\rho$ is defined as $\Delta\rho = \rho_{nZr\text{-}I} - \rho_{Zr} - \rho_{I,}$ where I represents B or C. The charge densities $\rho_{nZr\text{-}I}$, ρ_{Zr}, and ρ_I represent the total charge densities of the Zr-I system (*n* Zr atoms and one I atom in the supercell), of the pure Zr system (*n* Zr atoms in the same positions as in the

Zr-I system), and of an individual I atom, respectively. Both the Zr-B and Zr-C bonds show an asymmetric distribution of $\Delta\rho$ with surplus electrons around the C or B atom and charge depletion on the side of the Zr atom, indicative of a partial electron transfer from Zr to the interstitials. The charge depletion in Zr-C is larger than that of Zr-B because of the larger difference in electronegativity (electronegativities are 1.33 for Zr, 2.04 for B, and 2.55 for C, according to the Pauling scale).

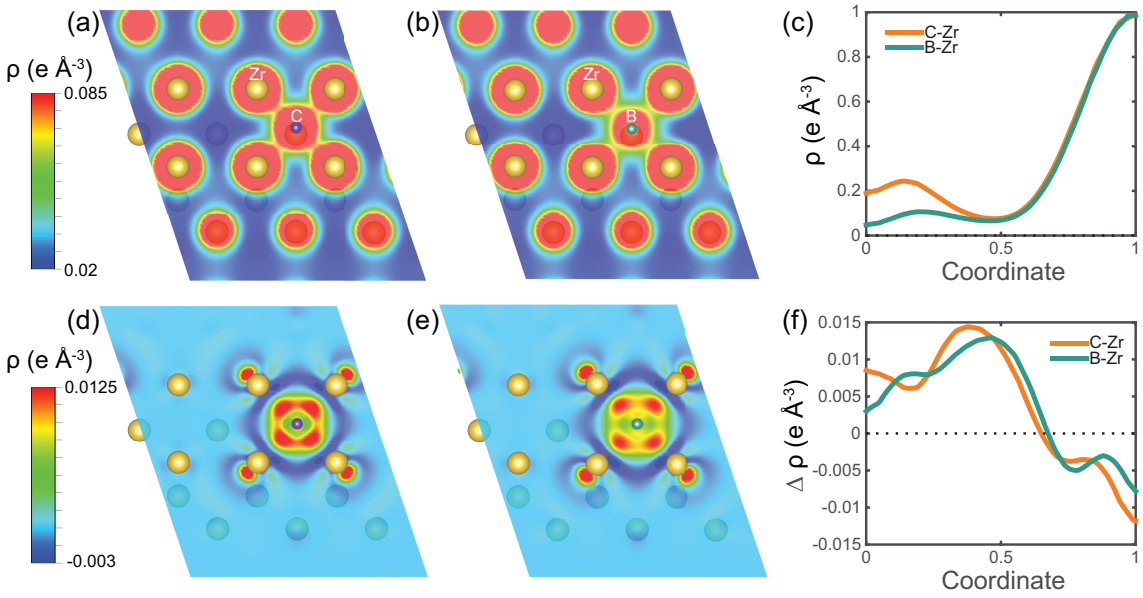


Figure 6.1. Valence electron charge density distribution on a $(01\bar{1}1)$ plane of Zr lattice with an interstitial C or B atom: 2D map (a, b) and line profile between C or B and the nearest Zr atom (c). The 2D maps of the charge density difference distribution in Zr with a C (d) or a B atom (e). The line profile is shown in (f).

6.2.2 Effect of C impurities on amorphization and diffusion in Zr/B alloys

Solid-state alloying of Zr-B in MRNL occurs by amorphization of the Zr lattice and diffusion of B through the amorphous layer [4]. We investigate how B and C break Zr bonds and mediate the amorphization process, and how the presence of C influences the transport of B in Zr single crystals. As shown in Figure 6.2a, each Zr-Zr bond in the basal plane (dashed line) of α-Zr is surrounded by two octahedral sites (Oct_1 and Oct_2) and a hexahedral site (Hex), which are energetically favorable sites for the insertion of B or C. We do not consider unstable interstitial sites such as the tetrahedral site (Tet) [5, 6, 90, 91]. We place up to three C and/or B atoms at the three sites surrounding a given Zr bond and calculate the change in bond length between the Zr atoms. Table 1 lists the results. The values between parentheses in the 4^{th} column of the table are the strains of the Zr-Zr bond in the relaxed structure (the original bond length in α-Zr is 3.24 Å). Taking a strain of 10 % as a threshold for bond breaking, it is clear that all configurations in the Table result in fracture of the Zr-Zr bond, except when B or C occupy only the Oct sites in the Zr lattice. Interstitial C atoms generally stretch the Zr bonds less than B atoms at the same site. This observation suggests that the addition of C to bulk Zr does not promote amorphization as much as B.

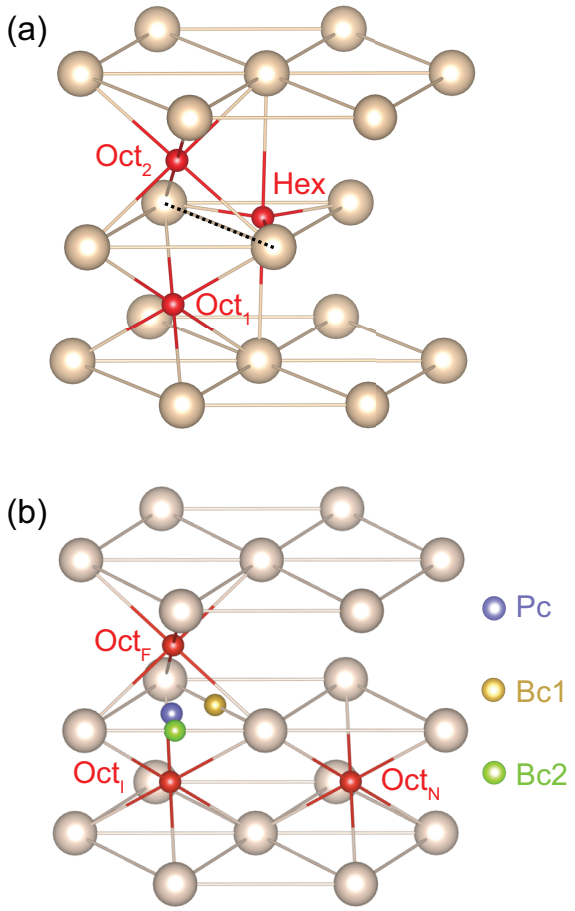


Figure 6.2. (a) Each Zr-Zr bond in the basal plane of α-Zr is surrounded by two Oct sites ($Oct_{1,2}$) and one Hex site. (b) Effect of an impurity atom at the neighboring Oct site (Oct_N) on the diffusion path of B from Oct (Oct_I) to Oct (Oct_F) along the *c*-axis.

Table 6.1. Position of impurity atoms and the resulting Zr-Zr bond length (atoms in a basal plane).

Oct_1	Oct_2	Hex	Bond length (Å) (Strain (%))
B	B	-	3.369 (4.01)
B	C	-	3.245 (0.19)
B	-	B	4.3266 (33.58)
C	-	B	4.330 (33.68)
B	-	C	4.001 (23.53)
B	B	B	4.329 (33.65)
B	C	B	4.299 (32.73)
B	B	C	4.239 (30.87)

6.2.3 AIMD on Zr/B and Zr/B_4C MRNLs

In Figure 6.2b and Table 2, we illustrate the effect of a B or C atom at a neighboring Oct (Oct_N) site on the diffusion of B in the direction of the *c*-axis (i.e., along the Oct_I – Oct_F path). We consider this diffusion path because as-deposited Zr in Zr/B_4C MRNLs prepared by magnetron sputtering usually has a strong (0001) texture [6]. Oct_I - Oct_F transitions via a bond center (Bc_1), another bond center (Bc_2), and a plane center (Pc) sites are considered. The static energy difference (ΔE_s) between the initial position (Oct_I) and the saddle point (a B atom in Bc_1, Bc_2, or Pc) is taken as a measure of the diffusion energy barrier [5, 6, 91] for each trajectory. Table 2 lists the calculated ΔE_s for each diffusion path. It is evident that the Oct_I – Bc_1 – Oct_F path always has the lowest energy barrier regardless of whether the Oct_N site is filled or the type of atom at the Oct_N site. It is also evident that filling the Oct_N site with C results in an increase in the energy

barrier from 1.60 - 1.66 eV to 1.84 eV, indicating that C slows down diffusive transport of B. The Boltzmann factor, $\exp(-\Delta E_s/k_B T)$, where k_B represents the Boltzmann constant and T the temperature, indicates that insertion of B at Oct_N reduces the probability of B diffusion along the Oct_I-Oct_F path by a factor of two, while a C atom decreases the B diffusivity by more than an order of magnitude at 1,000 K, the temperature where intermixing between B and Zr actively occurs [4].

Table 6.2. Effect of interstitial atoms at Oct_N on the diffusion energy barrier of B along the Oct_I – Oct_F path.

Atom at Oct_N	B diffusion path	ΔE_s (eV)
none	Oct_I – Bc_1 – Oct_F	1.60
none	Oct_I – Bc_2 – Oct_F	1.60
none	Oct_I – Pc – Oct_F	2.80
C	Oct_I – Bc_1 – Oct_F	1.84
C	Oct_I – Bc_2 – Oct_F	1.93
C	Oct_I – Pc – Oct_F	2.66
B	Oct_I – Bc_1 – Oct_F	1.66
B	Oct_I – Bc_2 – Oct_F	1.88
B	Oct_I – Pc – Oct_F	2.60

The above results indicate that addition of C to crystalline Zr decreases the mobility of B. We posit that both the reduced amorphization of Zr and the increased energy barrier for B diffusion in bulk Zr in the presence of C are caused by the stronger interaction between Zr and C than between Zr and B – the C atoms traps neighboring atoms more effectively and restrains their displacements. These observations clearly demonstrate that

the enhanced reaction kinetics (intermixing and crystallization) of Zr/B_4C MRNLs is due to enhanced B mobility, but is the result of processes associated with the interface between the amorphous B and crystalline Zr phases, an interface far from thermodynamic equilibrium.

To elucidate these interfacial processes, we perform ab-initio molecular dynamic simulations (AIMD) and explore the effects of C and N. A Zr/B multilayer structure (Figure 6.3a) is modeled by attaching an amorphous B layer of 72 atoms to the (0001) surface of a 3×3×2 α-Zr supercell (36 atoms). The amorphous B layer is created by first placing ten B atoms at random positions in a space that has the same basal area as the Zr supercell and a height of approximately 48% of the thickness of the Zr supercell [5]. Additional B atoms are then gradually inserted into this structure following a Delaunay triangulation (DT) analysis that identifies the largest voids in the structure. The DT analysis and insertion of additional 10 ~ 12 B atoms are followed by an energetic relaxation of the amorphous structure. This procedure is iterated until the structure contains 72 B atoms. Periodic boundary conditions are prescribed to the a-B/Zr structure to model the multilayer geometry and an energetic relaxation is performed to ensure that the structure is in a local energy minimum. This procedure ensures a better minimization of the interfacial mismatch compared to the case that B and Zr supercells are simply bonded. Zr/B_4C and the Zr/B_4N MRNLs are constructed by randomly replacing a number of B atoms with C or N atoms to achieve the correct stoichiometry. Ab-initio molecular dynamics (AIMD) simulations are carried out at 2,000 K. The supercells are allowed to dynamically equilibrate at each temperature for 10,000 time steps; each step corresponds to 2 fs.

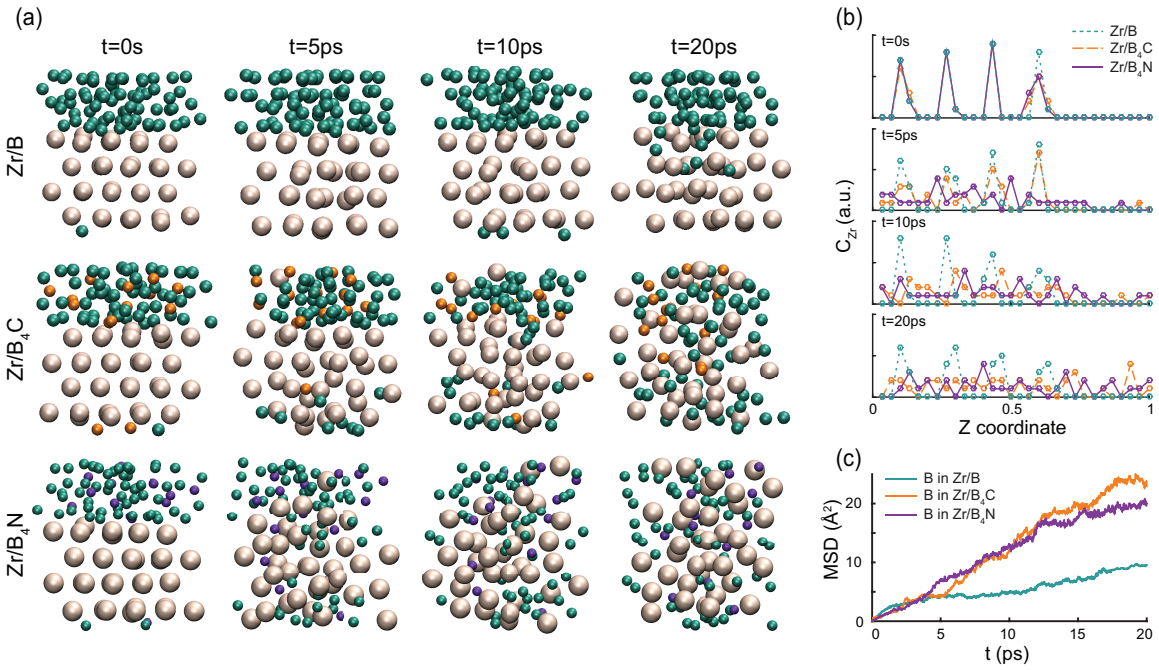


Figure 6.3. (a) Structural evolution of the Zr/B, the Zr/B_4C, and the Zr/B_4N MRNLs upon annealing at 2,000 K for 20 ps. (b) Concentration profile of Zr vs. the Z coordinate of the Zr/B (green, dotted), the Zr/B_4C (orange, dashed) and the Zr/B_4N (purple, solid) MRNLs at different annealing times. (c) Mean square displacement (MSD) of B atoms. The B, Zr, and C atoms are represented by green, orange, and purple spheres, respectively.

Figure 6.3 shows the structural evolution of the MRNLs, the Zr concentration (C_{Zr}) profile in the direction perpendicular to the MRNL at different annealing times, and the mean square displacement (MSD) of the B atoms in each MRNL. The value of the MSD is determined using $\text{MSD}=\left\langle \left| r_i(t) - r_i(0) \right|^2 \right\rangle$, where $r_i(t)$ is the position of atom i at time t, $r_i(0)$ is the position of atom i in the initial configuration, and <·> represents an average over the ensemble of atoms. It is evident from Figures 6.3a and 6.3b that the Zr concentration is homogenized much more quickly in the Zr/B_4C and Zr/B_4N MRNLs than in the Zr/B MRNL. The mobility of the B atoms, as measured by the MSD, is shown in Figure 6.3c for the three MRNLs. The addition of C and N to the amorphous B layer clearly enhances the diffusion of B atoms in the multilayered structure.

Figure 6.3 shows that the amorphization of the Zr lattice occurs at the Zr/B_4(C, N) interface. The accelerated B transport is a consequence of the enhanced intermixing of the constituent layers and amorphization of the Zr lattice at the Zr/B_4(C, N) interface, in good agreement with previous nanocalorimetry experiments [4-6]. We believe that the enhanced amorphization is caused by to the stronger interaction between Zr and C or N than between Zr and B: C or N atoms at the interface distort the Zr lattice more effectively than B. The amorphous layer, in turn, allows enhanced B diffusion because of its larger free volume. As shown in Figure 6.3a, Zr is progressively amorphized as this interface/reaction front propagates until intermixing is complete. These kinetic processes are driven by the steep concentration gradient at the interface between both phases. This qualitative understanding explains the enhanced reactivity of Zr/B MRNLs in the presence of C observed in nanocalorimetry experiments [4, 6].

6.2.4 Processing strategy of transition metal borides from MRNLs using impurity atoms

Our results suggest that any dopant atoms in the amorphous layers of the MRNLs, with a strong affinity for Zr and similar in size to B may enhance the amorphization of the Zr lattice and promote intermixing of the constituent layers. From the above results, one would expect N to have a stronger effect than C because the heat of formation of Zr-N is -233 kJ/mol [108], compared to -131 kJ/mol for Zr-C [108] (Figure 6.4b). The larger negative heat of mixing in Zr-N is attributed to the larger difference in electronegativity (Figure 6.4a). Figures 6.3a-6.3c show a comparison of the structural evolution and B mobility for Zr/B_4C and Zr/B_4N MRNLs. As expected, amorphization in the Zr/B_4N structure occurs earlier than in Zr/B_4C, achieving faster homogenization of the composition: the Zr/B_4N MRNL is almost fully homogenized after 5 ps, while the Zr/B_4C MRNL still has an unreacted Zr layer. As a result, the MSD of the B atoms in the Zr/B_4N MRNL is larger than in Zr/B_4C at 5 ps. After 10 ps, however, the MSD of the B atoms in Zr/B_4N is slightly smaller than in Zr/B_4C – the MSD curves at this time represent the mobility of B atoms in the amorphous ZrB_xC_y and ZrB_xN_y phases in the absence of sharp concentration gradients. In homogenous solutions, N decreases the mobility of B even more than C. This behavior is consistent with the glass theory - in a homogeneous solid solution, atoms with larger negative heat of mixing typically have lower mobility thus promoting the glass forming ability of the solution [109-111].

It is noteworthy that transition metals (TMs) that form crystalline diborides, such as Sc, Ti, V, Cr, Mn, Fe, Y, Zr, Nb, and Mo also have the largest negative heats of mixing and the largest differences in electronegativity with N, followed by C, and then by

B [108], as shown in Figure 6.4. We propose that the addition of C and/or N to the amorphous B layer will enhance the processibility of transition diborides using TM/B MRNLs.

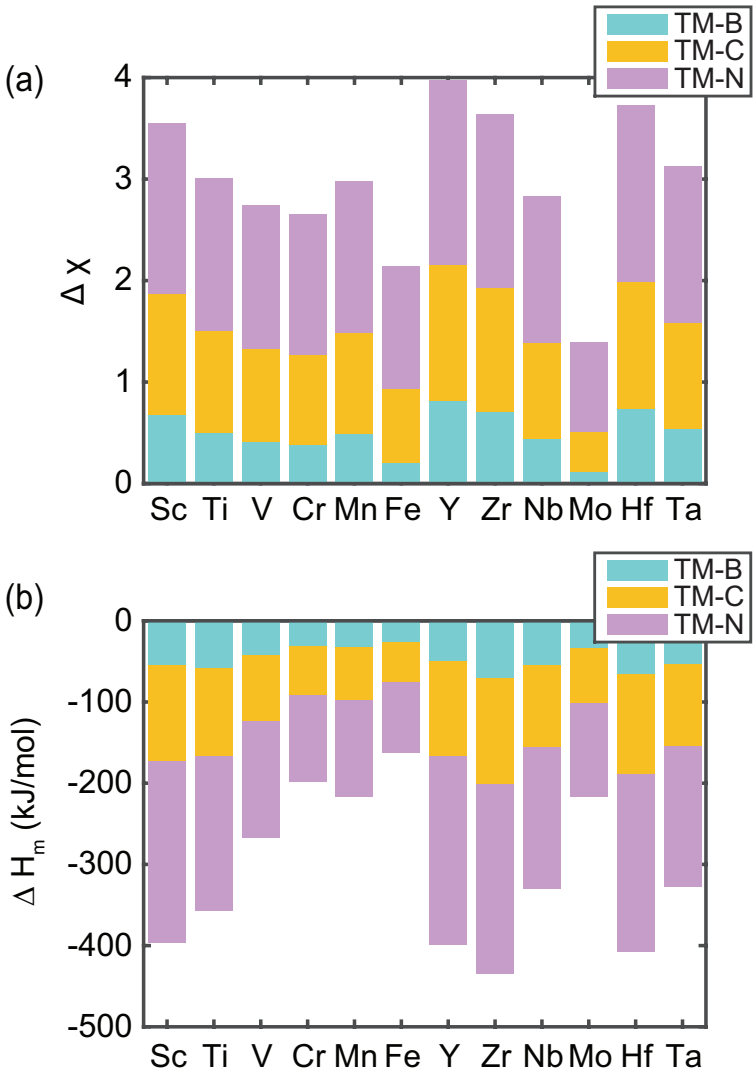


Figure 6.4. (a) Differences between transition metals (TMs) and B, C, or N atoms in (a) electro-negativity and (b) heat of formation[108].

6.3 METHODS

The first-principles calculations based on the DFT were carried out using the Vienna ab initio simulation package (VASP) [94]. The projected-augmented-waves (PAW) [95] with the Perdew-Burke-Ernzerhof (PBE) [96] exchange-correlation potentials were adopted. For Zr, the valence states were treated using a Zr_sv ($4s^2 4p^6 5s^2 4d^2$) pseudopotential. B ($2s^2 2p$), C ($2s^2 2p^2$), and N ($2s^2 2p^3$) pseudopotentials were employed for B, C, and N, respectively. The cut-off energy for plane waves was set to 400 eV, and the forces converged to within 0.02 eV/Å. We used a 54-atom Zr supercell (3×3×3) and B and/or C interstitial atoms for the simulations of amorphization and interstitial diffusion. We utilized a 36-atom Zr supercell (3×3×2) and 72 atom BC_xN_y amorphous layers in the AIMD simulations. For Brillouin zone sampling, 6 × 6 × 4, 6 × 6 × 4, and 1 x 1 x 1 *k*-point meshes in the Monkhorst−Pack scheme were employed for the amorphization, interstitial diffusion, and AIMD simulations, respectively. The AIMD simulations were performed at constant volume.

6.4 SUMMARY

In summary, we have employed a first-principles approach to investigate the catalytic role of additives in the low-temperature synthesis of metal diborides using MRNLs. The beneficial effect of C and N on the synthesis of ZrB_2 is attributed to the enhanced amorphization of the Zr and the enhanced intermixing of the constituent layers driven by the steep concentration gradient at the reaction front. While the strong

interaction between C/N and Zr reduces the mobility of B in bulk Zr, it facilitates the interfacial processes responsible for the amorphization. We suggest that dopants with a strong binding energy with transition metals may also facilitate the synthesis of diboride-based ceramics using MRNLs. The findings are in excellent agreement with recent nanocalorimetry experiments and provide important guidance for the synthesis of transition metal diborides.

Chapter 7. Conclusion and outlook

This thesis has explored reactions in MRNLs to synthesize ultra-high temperature ceramic of ZrB_2 based alloys through use of the combined approach of nanocalorimetry experiments and first-principles theoretical studies. The major accomplishments and findings of the thesis are summarized as follows.

- AC/DC nanocalorimetry combined with the data reduction procedure discussed in this thesis makes it possible to measure both heat capacities and reaction enthalpies (heat flows) for nanolaminate samples. This technique has been applied to characterize reactions in the Zr/B MRNLs and to synthesize ZrB_2 from the metastable structure. We have demonstrated that ZrB_2, an ultra-high temperature ceramic, with a strong crystallographic texture can be synthesized below 1,300K using MRNLs. The nanocalorimetry experiments and TEM reveal that the reaction proceeds in two stages: intermixing of Zr and B resulting in an amorphous Zr/B alloy and crystallization of this alloy to form ZrB_2. The interdiffusion process occurs at relatively low temperatures while the crystallization process occurs at more elevated temperatures. The formation of the amorphous alloy has been characterized using a diffusion limited model which determines an activation energy of diffusion as ~ 0.5 eV. The crystallization step, in contrast, has a much higher activation energy of ~ 2.4 eV.
- We have employed first-principles calculations to study thermodynamics and kinetics of the solid-state alloying process of Zr−B. In the limit of low B concentration, B transport in crystalline Zr is highly anisotropic and is dominated

by the interstitial diffusion in basal planes. With increasing B concentration, the Zr structure is gradually amorphized as a result of the rupture of host atom bonds and the formation of Zr−B clusters. The ZrB phase maintains the lowest enthalpy of formation among all the metastable compounds. The closely packed phase has the highest energy barrier and the lowest diffusivity for B transport. Nanocalorimetry results on the energy barrier show a good agreement with the value determined from the simulations.

- The combined approach of nanocalorimetry and first-principles calculations has been utilized to investigate the effects of impurities in the synthesis of ZrB_2 from MRNLs. Nanocalorimetry measurements have shown that intermixing of the two constituent layers of the Zr/B_4C MRNLs upon heating occurs, followed by crystallization to form a ZrB_2 phase that is supersaturated with C. Kinetic analyses show that the Zr/B_4C MRNLs have lower energy barriers for both interdiffusion and crystallization than Zr/B MRNLs. First-principles calculations suggest that the beneficial effect of the impurities on the synthesis of ZrB_2 is attributed to the enhanced amorphization of the Zr that facilitates intermixing of the constituent layers. We have suggested that dopants with a strong binding energy with transition metals may also facilitate the synthesis of diboride-based ceramics using MRNLs.

Use of the coordinated approach involving both nanocalorimetry and first-principles calculations described in this thesis is broadly applicable and may well provide

a new paradigm for materials discovery. Beyond the work in this thesis, the following subjects are interesting to explore in the future.

- The combined approach can be utilized to investigate an expanded material library of transition metal (TM) / B MRNLs with a goal of synthesizing TMB_2. First-principles theoretical studies can determine the energetics, structural evolution, and phase transitions in the solid-state alloying of B with transition metals, as well as the electronic, ionic, and mechanical properties of TMB_2. The modeling can draw the energy landscapes of diffusion and various reaction pathways, and identify the stable and/or metal-stable phases. The results from the theoretical studies can be verified using nanocalorimetry and structural characterization tools such as X-ray diffraction (XRD) and transmission electron microscopy (TEM). Nanocalorimetry measurements would enable investigation of formation mechanisms, characterize formation kinetics, and identify interfacial reactions versus diffusion-controlled regimes. The combination of techniques can explore the effects of additives such as C, N or Si, and to develop hybrid metal diborides $TM^1_{1-x}TM^2_xB_2$ with enhanced processibility and tailored thermo-physical properties [119].

Appendix

APPENDIX A

In this appendix, we provide an estimate of the conduction losses through the membrane and the heating element. Let *y* be the coordinate in the direction perpendicular to the heating element (See Figure 2.1d). The temperature distribution in the membrane is then described by the one-dimensional thermal diffusion equation [1],

$$\rho c_P \frac{\partial T}{\partial t} = k \frac{\partial^2 T}{\partial y^2} - 2 \frac{\varepsilon \sigma}{h} \left(T^4 - {T_0}^4 \right), \tag{A1}$$

with conditions

$$\begin{aligned} T(y,0) &= T_0, \\ T(0,t) &= T_0 + f(t), \\ T(\infty,t) &= T_0, \end{aligned} \tag{A2}$$

where *r*, c_p, *k*, *e*, and *h* designate the mass density, heat capacity, thermal conductivity, emissivity, and thickness of the membrane; *s* is the Stefan-Boltzmann constant. The function *f(t)* describes the temperature history of the heating element. Defining $\tau = T - T_0$,

$$\alpha = \frac{k}{\rho c_p}, \tag{A3}$$

$$\beta = \frac{8 \varepsilon \sigma {T_0}^3}{h \rho c_p}, \tag{A4}$$

and performing a linear expansion of the radiation term in Equation (A1) leads to the following equation

$$\frac{\partial \tau}{\partial t} = \alpha \frac{\partial^2 \tau}{\partial y^2} - \beta \tau, \tag{A5}$$

with conditions

$$T(y,0) = T_0,$$
$$T(0,t) = T_0 + f(t), \tag{A6}$$
$$T(\infty,t) = T_0.$$

The solution of this equation can be written as [1]

$$\tau(y,t) = \int_0^t f(t')K(t-t')dt', \tag{A7}$$

where

$$K(t-t') = \frac{y exp\left[\frac{-y^2}{4\alpha(t-t')} - \beta(t-t')\right]}{2\sqrt{\pi\alpha}(t-t')^{3/2}}. \tag{A8}$$

The integral in Equation (A7) is difficult to calculate numerically for arbitrary functions *f(t)*. Here we describe a simple method to evaluate the integral for an experimentally measured temperature history based on the realization that the integral is analytical for a linear temperature history. Specifically, if the experimental temperature history consists of a set of *n* data points (t_i, T_i) and is represented by a linear spline, the temperature profile at time t_n is well approximated by

$$\tau(y,t) = \sum_{i=1}^{n-2} \int_{t_i}^{t_{i+1}} (A_i + B_i t')K(t-t')dt' + \int_{t_{n-1}}^{t_n} (A_{n-1} + B_{n-1}t')K(t-t')dt', \tag{A9}$$

where

$$A_i = \frac{T_i t_{i+1} - T_{i+1} t_i}{t_{i+1} - t_i} \text{ and } B_i = \frac{T_{i+1} - T_i}{t_{i+1} - t_i}. \tag{A10}$$

The heat lost by conduction into the membrane is then given by

$$L_C = 2kA \left.\frac{\partial \tau}{\partial y}\right|_{y=0} \tag{A11}$$

$$= 2kA\left(\sum_{i=1}^{n-2}\frac{\partial}{\partial y}\left(\int_{t_i}^{t_{i+1}}(A_i + B_i t')K(t-t')dt'\right)\Big|_{y=0} + \frac{\partial}{\partial y}\left(\int_{t_{n-1}}^{t_n}(A_{n-1} + BB_{n-1}t')K(t-t')dt'\right)\Big|_{y=0}\right)$$

$$= 2kA\left(\sum_{i=1}^{n-2} I_i + I_{n-1}\right),$$

where A is the total cross-sectional area of the membrane. The integrals in Eq. (A11) can be evaluated analytically leading to the following expressions for I_i ad $I_{n\text{-}1}$

$$I_i = (A_i + B_i t_n)\frac{1}{\sqrt{\alpha\pi}}\left\{\frac{e^{\beta(t_{i+1}-t_n)}}{\sqrt{t_n - t_{i+1}}} - \frac{e^{\beta(t_i-t_n)}}{\sqrt{t_n - t_i}} + \sqrt{\beta\pi}\left(erf\left(\sqrt{\beta(t_n - t_{i+1})}\right) - erf\left(\sqrt{\beta(t_n - t_i)}\right)\right)\right\} + \frac{B_i}{2\sqrt{\alpha\beta}}\left(erf\left(\sqrt{\beta(t_n - t_{i+1})}\right) - erf\left(\sqrt{\beta(t_n - t_i)}\right)\right), \quad \text{(A12)}$$

and

$$I_{n-1} = -(A_{n-1} + B_{n-1}t_n)\frac{1}{\sqrt{\alpha\pi}}\left\{\frac{e^{\beta(t_{n-1}-t_n)}}{\sqrt{t_n - t_{n-1}}} + \sqrt{\beta\pi}erf\left(\sqrt{\beta(t_n - t_{n-1})}\right)\right\} - \frac{B_{n-1}}{2\sqrt{\alpha\beta}}erf\left(\sqrt{\beta(t_n - t_{n-1})}\right). \quad \text{(A13)}$$

Substituting Equations (A12) an (A13) into Equation (A11) results in an expression that can be used to estimate the conductive heat loss through the membrane at a time t_n from the prior temperature history of the heating element. Evaluation of this expression requires knowledge of the parameters a and b, which are readily determined experimentally [1]. The main approximation in the analysis is the linear expansion of the thermal radiation loss in Equation (A5). This approximation is acceptable as long as the neglected radiation loss terms are small compared to the other terms in the equation, i.e.,

$t \ll T_o/bt$, where t is the time scale of the experiment. Given the approximate character of the analysis, the preferred method of eliminating the conduction loss from experimental nanocalorimetry data is to take the difference between two subsequent scans with similar thermal histories. The above analysis can then be applied as a small correction to account for the difference in conduction loss as a result of the slight difference in thermal history between the two scans. That is the approach taken in this study.

Finally, the conduction loss through the heating element can be estimated using a similar approach. Because the element generates heat, it is necessary to include a volumetric power term in the left hand side of Equation (A1)

$$\rho c_P \frac{\partial T}{\partial t} = k \frac{\partial^2 T}{\partial x^2} - 2\frac{\varepsilon\sigma}{h}\left(T^4 - {T_0}^4\right) + P_v, \tag{A14}$$

where the physical constants now refer to the composite properties of the heating element and the membrane. The volumetric power changes with temperature through the temperature-dependence of the resistivity of the heating element

$$P_v = P_o(1 + \lambda\tau), \tag{A15}$$

so that Eq. (A14) can be reduced to

$$\frac{\partial \tau}{\partial t} = \alpha \frac{\partial^2 \tau}{\partial x^2} - \left(\beta - \frac{P_o \lambda}{\rho c_p}\right)\tau + \frac{P_o}{\rho c_p}. \tag{A16}$$

Writing this equation for the temperature difference between two subsequent scans eliminates the last term on the right hand side of the equation and an equation of the type (A5) is recovered. As long as P_o is constant and $P_o < brc_p/l$, the same approach can be used to calculate the conduction loss through the heating element as for the membrane.

APPENDIX B

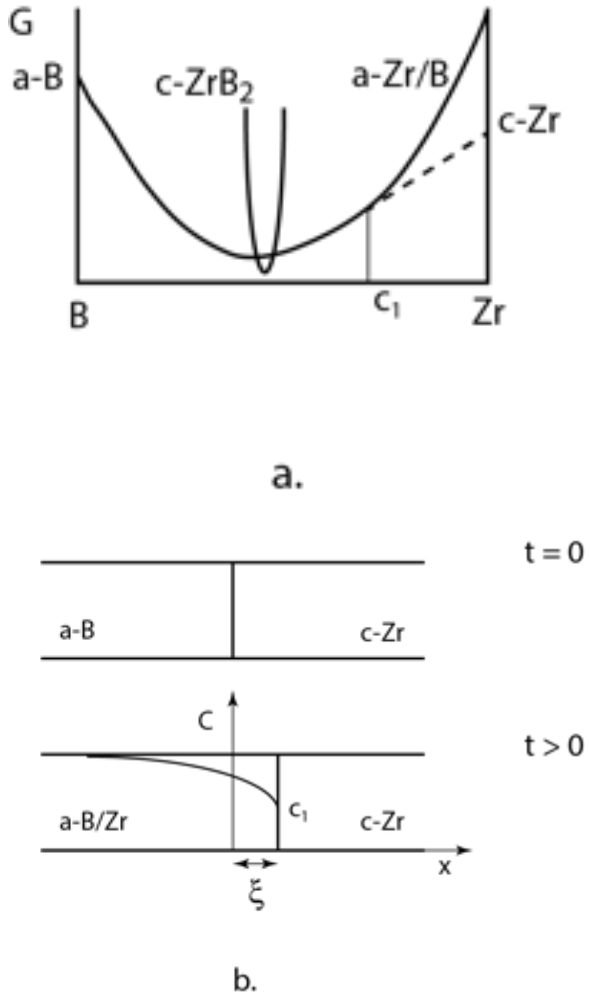


Figure B1. (a) Schematic free energy diagram for the B/Zr system. Crystalline Zr is in meta-stable equilibrium with an amorphous phase with B concentration C_1. (b) Concentration profiles after interdiffusion.

Figure B1 shows a simple model for the interdiffusion of amorphous B and crystalline Zr: c-Zr is in meta-stable equilibrium with an amorphous B/Zr phase with B concentration C_1; the solid solubility of B in c-Zr is taken negligibly small (a). After interdiffusion, the phase boundary has shifted a distance *x* and the B concentration in the amorphous phase has become non-uniform (b). We only consider the initial stage of the process where the diffusion distance is much smaller than the bilayer period of the sample. This problem can be formulated as a moving-boundary problem of the Stefan type. The concentration profile is the solution of the Fick's diffusion equation with the following boundary conditions,

$$\begin{aligned} C(-\infty,t) &= 1, \\ C(\xi,t) &= C_1. \end{aligned} \tag{B1}$$

The mass balance at the interface between the amorphous and crystalline phases further requires that

$$\frac{d\xi}{dt} = -\frac{D}{C_1}\frac{dC}{dx}\bigg|_{\xi}. \tag{B2}$$

Under isothermal conditions, the solution of this problem is a variant of Neumann's similarity solution and is given by

$$C(x,t) = 1 - \frac{1-C1}{1+\operatorname{erf}\alpha}\left(1+\operatorname{erf}\left(\frac{x}{2\sqrt{Dt}}\right)\right), \tag{B3}$$

$$\xi = 2\alpha\sqrt{Dt}, \tag{B4}$$

where *D* is the interdiffusion coefficient and *a* is a function of C_1, defined implicitly by

$$\alpha\left(1+\operatorname{erf}\alpha\right)\exp\alpha^2 = \frac{1-C1}{\sqrt{\pi}C1}. \tag{B5}$$

Taking the enthalpy released during interdiffusion to be proportional to the Zr concentration in the amorphous phase, it follows that

$$H = \frac{\Delta H}{t_{Zr}} \int_{-\infty}^{\xi} (1 - C)\, dx = 2 \frac{\alpha \Delta H}{t_{Zr}} \sqrt{Dt}\,, \tag{B6}$$

so that

$$H \frac{dH}{dt} = 2 \left(\frac{\alpha \Delta H}{t_{Zr}} \right)^2 D\,. \tag{B7}$$

In this expression ΔH is the total enthalpy released during interdiffusion of a single bilayer and t_{Zr} is the thickness of the Zr layers. Equation (B7) can be used to determine the diffusion coefficient from the heat flow obtained in an experiment performed under isothermal conditions. If experiments are not conducted under isothermal conditions, the solution to the diffusion problem is still valid, provided the product Dt is replaced by a quantity that depends on the entire temperature history $T(t)$ of the sample,

$$\tau = \int_{0}^{t} D(T(t))\, dt\,. \tag{B8}$$

For an experiment performed at constant heating rate b, Equation (B6) then becomes

$$H = 2 \frac{\alpha \Delta H}{t_{Zr} \sqrt{\beta}} \sqrt{\int_{T_o}^{T} D(T)\, dT}\,, \tag{B9}$$

but the product $H \frac{dH}{dt}$ is still given by Equation (B7) despite the non-isothermal conditions. If the diffusion coefficient D can be described by an Arrhenius equation, it follows that

$$\ln\left(H \frac{dH}{dt} \right) = 2 \ln\left(\frac{\alpha \Delta H \sqrt{2 D_o}}{t_{Zr}} \right) - \frac{E_d}{k_B T}\,, \tag{B10}$$

where k_B is the Boltzmann constant, E_d is the diffusion activation energy, and D_o is the pre-exponential factor of the diffusion coefficient. If some intermixing has taken place during deposition of the reactive multilayer, Equation (B10) may need to be replaced by

$$\ln\left(\left(H+H_o\right)\frac{dH}{dt}\right)=2\ln\left(\frac{\alpha\Delta H\sqrt{2D_o}}{t_{Zr}}\right)-\frac{E_d}{k_BT}, \tag{B11}$$

where H_o is the enthalpy associated with the intermixing. A graph of $\ln((H+H_o)dH/dt)$ versus $1/k_BT$ produces a straight line with as slope the activation energy E_d.

APPENDIX C

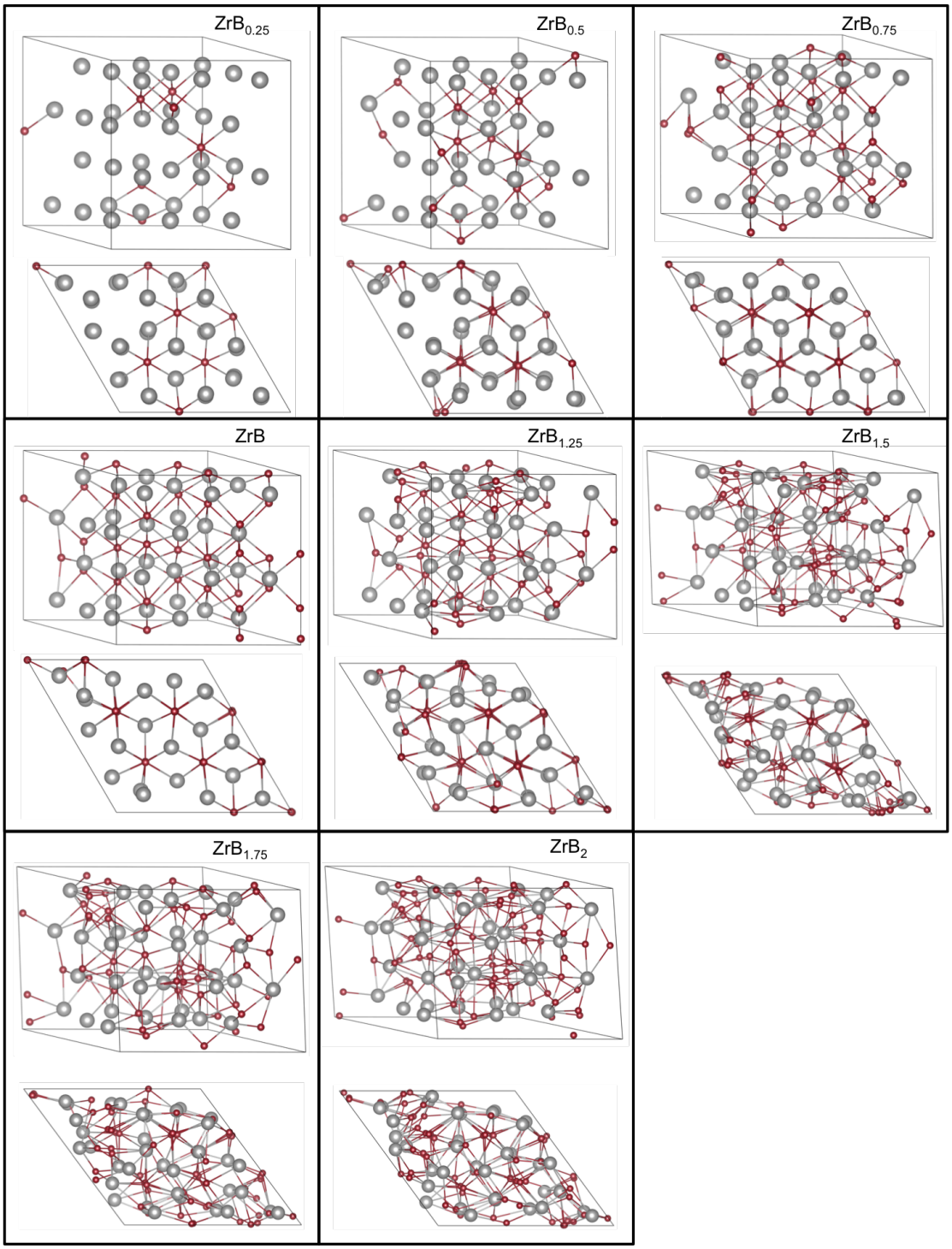


Figure C1. Structural evolution upon insertion of B in Zr lattice: prospect view (top) and plan view (bottom) at each concentration.

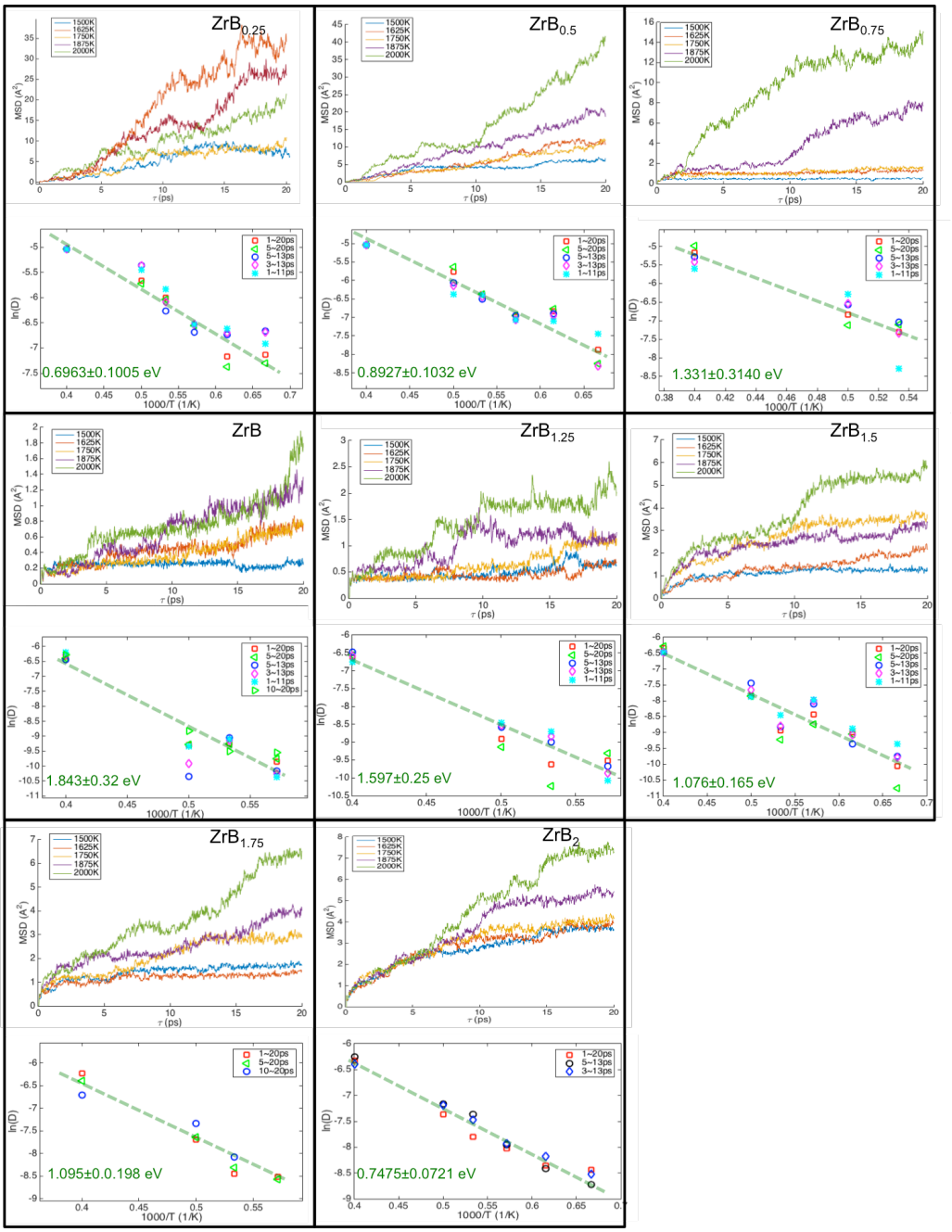


Figure C2. Mean square displacement (MSD) vs. simulation time (top) and diffusivity (D) vs. reciprocal temperature (bottom) for various concentrations. The activation energy of B diffusion for each concentration has been obtained by considering the Arrhenius relation and indicated in the diffusivity plots. MSD plots are not perfectly linear so we use different sample times to obtain diffusivity at each temperature. This calculation method and the non-linearity in the MSD plots create the error in the activation energy.

Bibliography

[1] P.J. McCluskey and J.J. Vlassak, *Nano-thermal transport array: An instrument for combinatorial measurements of heat transfer in nanoscale films.* Thin Solid Films, 2010. **518**(23): p. 7093-7106.

[2] P.J. McCluskey and J.J. Vlassak, *Combinatorial nanocalorimetry.* Journal of Materials Research, 2010. **25**(11): p. 2086-2100.

[3] K.C. Xiao, J.M. Gregoire, P.J. McCluskey, and J.J. Vlassak, *A scanning AC calorimetry technique for the analysis of nano-scale quantities of materials.* Review of Scientific Instruments, 2012. **83**(11): p. 114901.

[4] D. Lee, G.D. Sim, K.C. Xiao, and J.J. Vlassak, *Low-Temperature Synthesis of Ultra-High-Temperature Coatings of ZrB_2 Using Reactive Multilayers.* Journal of Physical Chemistry C, 2014. **118**(36): p. 21192-21198.

[5] D. Lee, J.J. Vlassak, and K. Zhao, *First-Principles Theoretical Studies and Nanocalorimetry Experiments on Solid-State Alloying of Zr–B.* Nano Letters, 2015. **15**(10): p. 6553-6558.

[6] D. Lee, G.-D. Sim, K. Zhao, and J.J. Vlassak, *Kinetic Role of Carbon in Solid-State Synthesis of Zirconium Diboride Using Nano-Laminates: Nanocalorimetry Experiments and First-Principles Calculations.* Nano Letters, 2015. **15**(12): p. 8266-8270.

[7] S. Carenco, D. Portehault, C. Boissiere, N. Mezailles, and C. Sanchez, *Nanoscaled metal borides and phosphides: recent developments and perspectives.* Chemical reviews, 2013. **113**(10): p. 7981-8065.

[8] W.G. Fahrenholtz, G.E. Hilmas, I.G. Talmy, and J.A. Zaykoski, *Refractory diborides of zirconium and hafnium.* Journal of the American Ceramic Society, 2007. **90**(5): p. 1347-1364.

[9] R. Liu, A. Bell, F.A. Ponce, S. Kamiyama, H. Amano, and I. Akasaki, *Atomic arrangement at the AlN/ZrB_2 interface.* Applied Physics Letters, 2002. **81**(17): p. 3182-3184.

[10] J. Suda and H. Matsunami, *Heteroepitaxial growth of group-III nitrides on lattice-matched metal boride ZrB_2 (0001) by molecular beam epitaxy.* Journal of Crystal Growth, 2002. **237**: p. 1114-1117.

[11] J. Tolle, R. Roucka, I.S.T. Tsong, C. Ritter, P.A. Crozier, A.V.G. Chizmeshya, and J. Kouvetakis, *Epitaxial growth of group III nitrides on silicon substrates via a reflective lattice-matched zirconium diboride buffer layer.* Applied Physics Letters, 2003. **82**(15): p. 2398-2400.

[12] Y. Yamada-Takamura, Z.T. Wang, Y. Fujikawa, T. Sakurai, Q.K. Xue, J. Tolle, P.L. Liu, A.V.G. Chizmeshya, J. Kouvetakis, and I.S.T. Tsong, *Surface and interface studies of GaN epitaxy on Si(111) via ZrB_2 buffer layers.* Physical Review Letters, 2005. **95**(26): p. 266105.

[13] K. Upadhya, J.M. Yang, and W.P. Hoffman, *Materials for ultrahigh temperature structural applications.* American Ceramic Society Bulletin, 1997. **76**(12): p. 51-56.

[14] M.M. Opeka, I.G. Talmy, and J.A. Zaykoski, *Oxidation-based materials selection for 2000 degrees C plus hypersonic aerosurfaces: Theoretical considerations and historical experience.* Journal of Materials Science, 2004. **39**(19): p. 5887-5904.

[15] C.W. Hu, A.V.G. Chizmeshya, J. Tolle, J. Kouvetakis, and I.S.T. Tsong, *Nucleation and growth of epitaxial ZrB_2(0001) on Si(111).* Journal of Crystal Growth, 2004. **267**(3-4): p. 554-563.

[16] R. Roucka, V.R. D'Costa, Y.J. An, M. Canonico, J. Kouvetakis, J. Menendez, and A.V.G. Chizmeshya, *Thermoelastic and optical properties of thick boride templates on silicon for nitride integration applications.* Chemistry of Materials, 2008. **20**(4): p. 1431-1442.

[17] D. Lee, G.D. Sim, K.C. Xiao, Y.S. Choi, and J.J. Vlassak, *Scanning AC nanocalorimetry study of Zr/B reactive multilayers.* Journal of Applied Physics, 2013. **114**(21): p. 214902.

[18] G. Samsonov and G. Zhunkovskii, *Mechanism of the reaction of refractory metals with boron in vacuum boriding.* Soviet Powder Metallurgy and Metal Ceramics, 1970. **9**(6): p. 472-478.

[19] C. Michaelsen, K. Barmak, and T.P. Weihs, *Investigating the thermodynamics and kinetics of thin film reactions by differential scanning calorimetry.* Journal of Physics D-Applied Physics, 1997. **30**(23): p. 3167-3186.

[20] D.P. Adams, *Reactive multilayers fabricated by vapor deposition: A critical review.* Thin Solid Films, 2015. **576**: p. 98-128.

[21] F. Spaepen and C.V. Thompson, *Calorimetric Studies of Reactions in Thin-Films and Multilayers.* Applied Surface Science, 1989. **38**(1-4): p. 1-12.

[22] D. Lee, G.D. Sim, K.C. Xiao, Y.S. Choi, and J.J. Vlassak, *Scanning AC nanocalorimetry study of Zr/B reactive multilayers.* Journal of Applied Physics, 2013. **114**(21): p. 214902.

[23] R.B. Schwarz and W.L. Johnson, *Formation of an Amorphous Alloy by Solid-State Reaction of the Pure Polycrystalline Metals.* Physical Review Letters, 1983. **51**(5): p. 415-418.

[24] R.J. Highmore, J.E. Evetts, A.L. Greer, and R.E. Somekh, *Differential Scanning Calorimetry Study of Solid-State Amorphization in Multilayer Thin-Film Ni/Zr.* Applied Physics Letters, 1987. **50**(10): p. 566-568.

[25] P.J. Desre and A.R. Yavari, *Suppression of Crystal Nucleation in Amorphous Layers with Sharp Concentration Gradients.* Physical Review Letters, 1990. **64**(13): p. 1533-1536.

[26] P.J. Desre, *Effect of Sharp Concentration Gradients on the Stability of a 2-Component Amorphous Layer Obtained by Solid-State Reaction.* Acta Metallurgica Et Materialia, 1991. **39**(10): p. 2309-2315.

[27] F. Hodaj and P.J. Desre, *Effect of a sharp gradient of concentration on nucleation of intermetallics at interfaces between polycrystalline layers.* Acta Materialia, 1996. **44**(11): p. 4485-4490.

[28] P. Vajeeston, P. Ravindran, C. Ravi, and R. Asokamani, *Electronic structure, bonding, and ground-state properties of AlB_2-type transition-metal diborides.* Physical Review B, 2001. **63**(4): p. 045115.

[29] S.Q. Guo, *Densification of ZrB_2-based composites and their mechanical and physical properties: A review.* Journal of the European Ceramic Society, 2009. **29**(6): p. 995-1011.

[30] S.K.M. Pathak, S. Das, S.K. Das, and P. Ramachandrarao, *Sintering studies on ultrafine ZrB_2 powder produced by a self-propagating high-temperature synthesis process.* Journal of Materials Research, 2000. **15**(11): p. 2499-2504.

[31] S.Q. Guo, T. Nishimura, and Y. Kagawa, *Preparation of zirconium diboride ceramics by reactive spark plasma sintering of zirconium hydride-boron powders.* Scripta Materialia, 2011. **65**(11): p. 1018-1021.

[32] M. Brochu, B. Gauntt, T. Zimmerly, A. Ayala, and R. Loehman, *Fabrication of UHTCs by conversion of dynamically consolidated Zr+B and Hf+B powder mixtures.* Journal of the American Ceramic Society, 2008. **91**(9): p. 2815-2822.

[33] S.Q. Guo, C.F. Hu, and Y. Kagawa, *Mechanochemical Processing of Nanocrystalline Zirconium Diboride Powder.* Journal of the American Ceramic Society, 2011. **94**(11): p. 3643-3647.

[34] A.L. Chamberlain, W.G. Fahrenholtz, and G.E. Hilmas, *Reactive hot pressing of zirconium diboride.* Journal of the European Ceramic Society, 2009. **29**(16): p. 3401-3408.

[35] M. Vohra, M. Grapes, P. Swaminathan, T.P. Weihs, and O.M. Knio, *Modeling and quantitative nanocalorimetric analysis to assess interdiffusion in a Ni/Al bilayer.* Journal of Applied Physics, 2011. **110**(12): p. 123521.

[36] K.J. Blobaum, D. Van Heerden, A.J. Gavens, and T.P. Weihs, *Al/Ni formation reactions: characterization of the metastable Al_9Ni_2 phase and analysis of its formation.* Acta Materialia, 2003. **51**(13): p. 3871-3884.

[37] K. Barmak, C. Michaelsen, and G. Lucadamo, *Reactive phase formation in sputter-deposited Ni/Al multilayer thin films.* Journal of Materials Research, 1997. **12**(1): p. 133-146.

[38] E.A. Olson, M. Yu, Y. Efremov, M. Zhang, Z.S. Zhang, and L.H. Allen, *The design and operation of a MEMS differential scanning nanocalorimeter for high-speed heat capacity measurements of ultrathin films.* Journal of Microelectromechanical Systems, 2003. **12**(3): p. 355-364.

[39] Y. Motemani, P.J. McCluskey, C.W. Zhao, M.J. Tan, and J.J. Vlassak, *Analysis of Ti-Ni-Hf shape memory alloys by combinatorial nanocalorimetry.* Acta Materialia, 2011. **59**(20): p. 7602-7614.

[40] K.C. Xiao, J.M. Gregoire, P.J. McCluskey, D. Dale, and J.J. Vlassak, *Scanning AC nanocalorimetry combined with in-situ x-ray diffraction.* Journal of Applied Physics, 2013. **113**(24): p. 243501.

[41] J.M. Gregoire, K.C. Xiao, P.J. McCluskey, D. Dale, G. Cuddalorepatta, and J.J. Vlassak, *In-situ X-ray diffraction combined with scanning AC nanocalorimetry applied to a $Fe_{0.84}Ni_{0.16}$ thin-film sample.* Applied Physics Letters, 2013. **102**(20): p. 201902.

[42] H. Huth, A.A. Minakov, and C. Schick, *Differential AC-chip calorimeter for glass transition measurements in ultrathin films.* Journal of Polymer Science Part B-Polymer Physics, 2006. **44**(20): p. 2996-3005.

[43] J. Wang, E. Besnoin, O.M. Knio, and T.P. Weihs, *Investigating the effect of applied pressure on reactive multilayer foil joining.* Acta Materialia, 2004. **52**(18): p. 5265-5274.

[44] J. Wang, E. Besnoin, A. Duckham, S.J. Spey, M.E. Reiss, O.M. Knio, M. Powers, M. Whitener, and T.P. Weihs, *Room-temperature soldering with nanostructured foils.* Applied Physics Letters, 2003. **83**(19): p. 3987-3989.

[45] A.J. Swiston, T.C. Hufnagel, and T.P. Weihs, *Joining bulk metallic glass using reactive multilayer foils.* Scripta Materialia, 2003. **48**(12): p. 1575-1580.

[46] X. Qiu and J. Wang, *Bonding silicon wafers with reactive multilayer foils.* Sensors and Actuators a-Physical, 2008. **141**(2): p. 476-481.

[47] A. Duckham, S.J. Spey, J. Wang, M.E. Reiss, T.P. Weihs, E. Besnoin, and O.M. Knio, *Reactive nanostructured foil used as a heat source for joining titanium.* Journal of Applied Physics, 2004. **96**(4): p. 2336-2342.

[48] P.J. McCluskey and J.J. Vlassak, *Glass transition and crystallization of amorphous Ni-Ti-Zr thin films by combinatorial nano-calorimetry.* Scripta Materialia, 2011. **64**(3): p. 264-267.

[49] C.A. Ross, D.T. Wu, L.M. Goldman, and F. Spaepen, *Measurements of Interdiffusion in Electrodeposited Nickel-Phosphorus Multilayers.* Journal of Applied Physics, 1992. **72**(7): p. 2773-2780.

[50] J.W. Zimmermann, G.E. Hilmas, W.G. Fahrenholtz, R.B. Dinwiddie, W.D. Porter, and H. Wang, *Thermophysical properties of ZrB_2 and ZrB_2-SiC ceramics.* Journal of the American Ceramic Society, 2008. **91**(5): p. 1405-1411.

[51] A.L. Chamberlain, W.G. Fahrenholtz, and G.E. Hilmas, *Low-temperature densification of zirconium diboride ceramics by reactive hot pressing.* Journal of the American Ceramic Society, 2006. **89**(12): p. 3638-3645.

[52] K.R. Coffey, L.A. Clevenger, K. Barmak, D.A. Rudman, and C.V. Thompson, *Experimental-Evidence for Nucleation during Thin-Film Reactions.* Applied Physics Letters, 1989. **55**(9): p. 852-854.

[53] E.J. Huber, E.L. Head, and C.E. Holley, *Heats of Formation of Zirconium Diboride and Dioxide.* Journal of Physical Chemistry, 1964. **68**(10): p. 3040-3042.

[54] V. Zamora, A.L. Ortiz, F. Guiberteau, and M. Nygren, *Spark-plasma sintering of ZrB_2 ultra-high-temperature ceramics at lower temperature via nanoscale crystal refinement.* Journal of the European Ceramic Society, 2012. **32**(10): p. 2529-2536.

[55] W.G. Fahrenholtz, G.E. Hilmas, S.C. Zhang, and S. Zhu, *Pressureless sintering of zirconium diboride: Particle size and additive effects.* Journal of the American Ceramic Society, 2008. **91**(5): p. 1398-1404.

[56] W.G. Fahrenholtz, G.E. Hilmas, A.L. Chamberlain, and J.W. Zimmermann, *Processing and characterization of ZrB_2-based ultra-high temperature monolithic and fibrous monolithic ceramics.* Journal of Materials Science, 2004. **39**(19): p. 5951-5957.

[57] D. Sciti, S. Guicciardi, A. Bellosi, and G. Pezzotti, *Properties of a pressureless-sintered ZrB_2-$MoSi_2$ ceramic composite.* Journal of the American Ceramic Society, 2006. **89**(7): p. 2320-2322.

[58] L. Silvestroni and D. Sciti, *Effects of $MoSi_2$ additions on the properties of Hf- and Zr-B_2 composites produced by pressureless sintering.* Scripta Materialia, 2007. **57**(2): p. 165-168.

[59] S.C. Zhang, G.E. Hilmas, and W.G. Fahrenholtz, *Pressureless densification of zirconium diboride with boron carbide additions.* Journal of the American Ceramic Society, 2006. **89**(5): p. 1544-1550.

[60] M. Thompson, W.G. Fahrenholtz, and G. Hilmas, *Effect of Starting Particle Size and Oxygen Content on Densification of ZrB_2.* Journal of the American Ceramic Society, 2011. **94**(2): p. 429-435.

[61] V. Zamora, A.L. Ortiz, F. Guiberteau, and M. Nygren, *Crystal-size dependence of the spark-plasma-sintering kinetics of ZrB_2 ultra-high-temperature ceramics.* Journal of the European Ceramic Society, 2012. **32**(2): p. 271-276.

[62] R.J. Highmore, R.E. Somekh, J.E. Evetts, and A.L. Greer, *Differential Scanning Calorimetry Studies of Solid-State Amorphization in Multilayer Ni/Zr.* Journal of the Less-Common Metals, 1988. **140**: p. 353-360.

[63] E.J. Cotts, W.J. Meng, and W.L. Johnson, *Calorimetric Study of Amorphization in Planar, Binary, Multilayer, Thin-Film Diffusion Couples of Ni and Zr.* Physical Review Letters, 1986. **57**(18): p. 2295-2298.

[64] L.A. Clevenger and C.V. Thompson, *Nucleation-Limited Phase Selection during Reactions in Nickel Amorphous-Silicon Multilayer Thin-Films.* Journal of Applied Physics, 1990. **67**(3): p. 1325-1333.

[65] E. Ma, C.V. Thompson, and L.A. Clevenger, *Nucleation and Growth during Reactions in Multilayer Al/Ni Films - the Early Stage of Al_3Ni Formation.* Journal of Applied Physics, 1991. **69**(4): p. 2211-2218.

[66] T.P. Weihs, T.W. Barbee, and M.A. Wall, *A low-temperature technique for measuring enthalpies of formation.* Journal of Materials Research, 1996. **11**(6): p. 1403-1409.

[67] P. Swaminathan, M.D. Grapes, K. Woll, S.C. Barron, D.A. LaVan, and T.P. Weihs, *Studying exothermic reactions in the Ni-Al system at rapid heating rates using a nanocalorimeter.* Journal of Applied Physics, 2013. **113**(14): p. 143509.

[68] R.K. Kummamuru, L. De La Rama, L. Hu, M.D. Vaudin, M.Y. Efremov, M.L. Green, D.A. LaVan, and L.H. Allen, *Measurement of heat capacity and enthalpy of formation of nickel silicide using nanocalorimetry.* Applied Physics Letters, 2009. **95**(18): p. 181911.

[69] L.P. Cook, R.E. Cavicchi, N. Bassim, S. Eustis, W. Wong-Ng, I. Levin, U.R. Kattner, C.E. Campbell, C.B. Montgomery, W.F. Egelhoff, and M.D. Vaudin, *Enhanced mass transport in ultrarapidly heated Ni/Si thin-film multilayers.* Journal of Applied Physics, 2009. **106**(10): p. 104909.

[70] J.M. Gregoire, P.J. McCluskey, D. Dale, S.Y. Ding, J. Schroers, and J.J. Vlassak, *Combining combinatorial nanocalorimetry and X-ray diffraction techniques to study the effects of composition and quench rate on Au-Cu-Si metallic glasses.* Scripta Materialia, 2012. **66**(3-4): p. 178-181.

[71] J. Orava, A.L. Greer, B. Gholipour, D.W. Hewak, and C.E. Smith, *Characterization of supercooled liquid $Ge_2Sb_2Te_5$ and its crystallization by ultrafast-heating calorimetry.* Nature Materials, 2012. **11**(4): p. 279-283.

[72] K.C. Xiao, J.M. Gregoire, P.J. McCluskey, and J.J. Vlassak, *A scanning AC calorimetry technique for the analysis of nano-scale quantities of materials.* Review of Scientific Instruments, 2012. **83**(11): p. 114901.

[73] M. Molina-Ruiz, A.F. Lopeandia, M. Gonzalez-Silveira, Y. Anahory, M. Guihard, G. Garcia, M.T. Clavaguera-Mora, F. Schiettekatte, and J. Rodriguez-Viejo, *Formation of Pd_2Si on single-crystalline Si (100) at ultrafast heating rates: An in-situ analysis by nanocalorimetry.* Applied Physics Letters, 2013. **102**(14): p. 143111.

[74] P. Cebe, X. Hu, D.L. Kaplan, E. Zhuravlev, A. Wurm, D. Arbeiter, and C. Schick, *Beating the Heat - Fast Scanning Melts Silk Beta Sheet Crystals.* Scientific Reports, 2013. **3**.

[75] M. Ahrenberg, M. Brinckmann, J.W.P. Schmelzer, M. Beck, C. Schmidt, O. Kessler, U. Kragl, S.P. Verevkin, and C. Schick, *Determination of volatility of ionic liquids at the nanoscale by means of ultra-fast scanning calorimetry.* Physical Chemistry Chemical Physics, 2014. **16**(7): p. 2971-2980.

[76] S.A. Golovanenko, A.B. Natapova, B.A. Klypin, and T.M. Kesaev, *Recrystallization of Tungsten Alloys.* Metal Science and Heat Treatment, 1976. **18**(9-10): p. 810-812.

[77] E.J. Huber, E.L. Head, and C.E. Holley, *The Heats of Formation of Zirconium Diboride and Dioxide1.* The Journal of Physical Chemistry, 1964. **68**: p. 3040-3042.

[78] H.E. Kissinger, *Reaction Kinetics in Differential Thermal Analysis.* Analytical Chemistry, 1957. **29**(11): p. 1702-1706.

[79] G.V. Samsonov and G.L. Zhunkovskii, *Mechanism of the reaction of refractory metals with boron in vacuum boriding.* Soviet Powder Metallurgy and Metal Ceramics, 1970. **9**: p. 472-478.

[80] B.M. Clemens, *Solid-State Reaction and Structure in Compositionally Modulated Zirconium-Nickel and Titanium-Nickel Films.* Physical Review B, 1986. **33**(11): p. 7615-7624.

[81] S.K. Mishra, S. Das, and L.C. Pathak, *Defect structures in zirconium diboride powder prepared by self-propagating high-temperature synthesis.* Materials Science and Engineering a-Structural Materials Properties Microstructure and Processing, 2004. **364**(1-2): p. 249-255.

[82] F. Willaime, *Ab initio study of self-interstitials in hcp-Zr.* Journal of Nuclear Materials, 2003. **323**(2-3): p. 205-212.

[83] M.I. Mendelev and B.S. Bokstein, *Molecular dynamics study of self-diffusion in Zr.* Philosophical Magazine, 2010. **90**(5): p. 637-654.

[84] G.D. Samolyuk, A.V. Barashev, S.I. Golubov, Y.N. Osetsky, and R.E. Stoller, *Analysis of the anisotropy of point defect diffusion in hcp Zr.* Acta Materialia, 2014. **78**: p. 173-180.

[85] R. Kumar, M.C. Mishra, B.K. Sharma, V. Sharma, J.E. Lowther, V. Vyas, and G. Sharma, *Electronic structure and elastic properties of TiB_2 and ZrB_2.* Computational Materials Science, 2012. **61**: p. 150-157.

[86] S.C. Middleburgh, D.C. Parfitt, P.R. Blair, and R.W. Grimes, *Atomic Scale Modeling of Point Defects in Zirconium Diboride.* Journal of the American Ceramic Society, 2011. **94**(7): p. 2225-2229.

[87] J.W. Lawson, C.W. Bauschlicher, and M.S. Daw, *Ab Initio Computations of Electronic, Mechanical, and Thermal Properties of ZrB_2 and HfB_2.* Journal of the American Ceramic Society, 2011. **94**(10): p. 3494-3499.

[88] H. Li, L.T. Zhang, Q.F. Zeng, J.J. Wang, L.F. Cheng, H.T. Ren, and K. Guan, *Crystal structure and elastic properties of ZrB compared with ZrB_2: A first-principles study.* Computational Materials Science, 2010. **49**(4): p. 814-819.

[89] J. Li and C. Fan, *Novel metastable compounds in the Zr–B system: an ab initio evolutionary study.* Physical Chemistry Chemical Physics, 2015. **17**(2): p. 1180-1188.

[90] R.G. Hennig, D.R. Trinkle, J. Bouchet, S.G. Srinivasan, R.C. Albers, and J.W. Wilkins, *Impurities block the alpha to omega martensitic transformation in titanium.* Nature Materials, 2005. **4**(2): p. 129-133.

[91] H.H. Wu and D.R. Trinkle, *Direct Diffusion through Interpenetrating Networks: Oxygen in Titanium.* Physical Review Letters, 2011. **107**(4): p. 045504.

[92] Y.F. Zhang, Y.J. Li, Z.Y. Wang, and K.J. Zhao, *Lithiation of SiO_2 in Li-Ion Batteries: In Situ Transmission Electron Microscopy Experiments and Theoretical Studies.* Nano Letters, 2014. **14**(12): p. 7161-7170.

[93] P. Rogl and P.E. Potter, *A Critical-Review and Thermodynamic Calculation of the Binary-System - Zirconium-Boron.* Calphad-Computer Coupling of Phase Diagrams and Thermochemistry, 1988. **12**(2): p. 191-204.

[94] G. Kresse and J. Furthmuller, *Efficient iterative schemes for ab initio total-energy calculations using a plane-wave basis set.* Physical Review B, 1996. **54**(16): p. 11169-11186.

[95] G. Kresse and D. Joubert, *From ultrasoft pseudopotentials to the projector augmented-wave method.* Physical Review B, 1999. **59**(3): p. 1758-1775.

[96] J.P. Perdew, K. Burke, and M. Ernzerhof, *Generalized gradient approximation made simple.* Physical Review Letters, 1996. **77**(18): p. 3865-3868.

[97] G. Henkelman and H. Jonsson, *Improved tangent estimate in the nudged elastic band method for finding minimum energy paths and saddle points.* Journal of Chemical Physics, 2000. **113**(22): p. 9978-9985.

[98] G. Henkelman, B.P. Uberuaga, and H. Jonsson, *A climbing image nudged elastic band method for finding saddle points and minimum energy paths.* Journal of Chemical Physics, 2000. **113**(22): p. 9901-9904.

[99] P. Wu, H.F. Lv, T. Peng, D.P. He, and S.C. Mu, *Nano Conductive Ceramic Wedged Graphene Composites as Highly Efficient Metal Supports for Oxygen Reduction.* Scientific Reports, 2014. **4**.

[100] H.F. Lv and S.C. Mu, *Nano-ceramic support materials for low temperature fuel cell catalysts.* Nanoscale, 2014. **6**(10): p. 5063-5074.

[101] S. Meng, E. Kaxiras, and Z.Y. Zhang, *Metal-diboride nanotubes as high-capacity hydrogen storage media.* Nano Letters, 2007. **7**(3): p. 663-667.

[102] S.-Q. Guo, *Densification of ZrB_2-based composites and their mechanical and physical properties: A review.* Journal of the European Ceramic Society, 2009. **29**(6): p. 995-1011.

[103] S.K. Mishra and S.K. Das, *Sintering and microstructural behaviour of SHS produced zirconium diboride powder with the addition of C and TiC.* Materials Letters, 2005. **59**(27): p. 3467-3470.

[104] S. Zhu, W.G. Fahrenholtz, G.E. Hilmas, and S.C. Zhang, *Pressureless sintering of zirconium diboride using boron carbide and carbon additions.* Journal of the American Ceramic Society, 2007. **90**(11): p. 3660-3663.

[105] S. Zhu, W.G. Fahrenholtz, G.E. Hilmas, and S.C. Zhang, *Pressureless sintering of carbon-coated zirconium diboride powders.* Materials Science and Engineering: A, 2007. **459**(1): p. 167-171.

[106] F. Goutier, G. Trolliard, S. Valette, A. Maître, and C. Estournès, *Role of impurities on the spark plasma sintering of ZrC_x–ZrB_2 composites.* Journal of the European Ceramic Society, 2008. **28**(3): p. 671-678.

[107] G.J. Zhang, M. Ando, J.F. Yang, T. Ohji, and S. Kanzaki, *Boron carbide and nitride as reactants for in situ synthesis of boride-containing ceramic composites.* Journal of the European Ceramic Society, 2004. **24**(2): p. 171-178.

[108] A. Takeuchi and A. Inoue, *Classification of bulk metallic glasses by atomic size difference, heat of mixing and period of constituent elements and its application to characterization of the main alloying element.* Materials Transactions, 2005. **46**(12): p. 2817-2829.

[109] W.L. Johnson, *Thermodynamic and Kinetic Aspects of the Crystal to Glass Transformation in Metallic Materials.* Progress in Materials Science, 1986. **30**(2): p. 81-134.

[110] A.L. Greer, *Metallic Glasses.* Science, 1995. **267**(5206): p. 1947-1953.

[111] J. Schroers, *Bulk Metallic Glasses.* Physics Today, 2013. **66**(2): p. 32-37.

[112] A.L. Greer, *Confusion by Design.* Nature, 1993. **366**(6453): p. 303-304.

[113] R.W. Balluffi, S. Allen, and W.C. Carter, *Chap. 19., Kinetics of materials*. 2005: John Wiley & Sons.

[114] J. Mayer, L.A. Giannuzzi, T. Kamino, and J. Michael, *TEM sample preparation and FIB-induced damage.* Mrs Bulletin, 2007. **32**(05): p. 400-407.

[115] Q. Gu, G. Krauss, and W. Steurer, *Transition Metal Borides: Superhard versus Ultra-incompressihle.* Advanced Materials, 2008. **20**(19): p. 3620-3626.

[116] H.Y. Chung, M.B. Weinberger, J.B. Levine, A. Kavner, J.M. Yang, S.H. Tolbert, and R.B. Kaner, *Synthesis of ultra-incompressible superhard rhenium diboride at ambient pressure.* Science, 2007. **316**(5823): p. 436-439.

[117] Y.Y. Wu, B. Messer, and P.D. Yang, *Superconducting MgB_2 nanowires.* Advanced Materials, 2001. **13**(19): p. 1487-1489.

[118] R.V. Reeves, M.A. Rodriguez, E.D. Jones, and D.P. Adams, *Condensed-Phase and Oxidation Reaction Behavior of Ti/2B Foils in Varied Gaseous Environments.* Journal of Physical Chemistry C, 2012. **116**(33): p. 17904-17912.

[119] M.B. Weinberger, J.B. Levine, H.Y. Chung, R.W. Cumberland, H.I. Rasool, J.M. Yang, R.B. Kaner, and S.H. Tolbert, *Incompressibility and Hardness of Solid Solution Transition Metal Diborides: $Os_{1-x}Ru_xB_2$.* Chemistry of Materials, 2009. **21**(9): p. 1915-1921.